ISAE - Supaero & Politecnico di Torino

Master's thesis in Aerospace Engineering

A.a. 2024-2025

Damage and Failure Identification of Carbon Fiber Reinforced Thermoplastic Laminates under Static and Dynamic Loading

Professors:
ISAE-Supaero: Prof. Frédéric Lachaud
`frederic.lachaud@isae-supaero.fr`
Politecnico di Torino: Prof. Marco Gherlone
`marco.gherlone@polito.it`

Student:
Federica Lovero

Abstract

Recent advancements in composite technology using fiber-reinforced polymeric materials have greatly benefited the aerospace industry, which requires lighter and more efficient materials. Since the 1970s, thermoset composites have been favored due to their high failure strength, low creep, and high elastic modulus at a relatively low cost. However, thermosets have limitations, including storage, aging, toughness, and complex processing steps. As a result, research is increasingly focused on replacing thermoset matrices with thermoplastic ones. Fiber-reinforced thermoplastic composites offer advantages like better damage tolerance, impact resistance, recyclability, repairability, and faster production cycles, making them an attractive alternative. This work presents the development of a constitutive model for fiber-reinforced thermoplastics, implemented in finite element method software and being experimentally verified.

Contents

Chapter 1

Introduction

1.1 Project introduction

One of the key developments of recent times is, without any doubts, composite technology using fiber reinforced polymeric materials. The excellent specific properties of these materials perfectly meet the requirements of the aerospace industry which is in need of more light and, overall, more efficient materials.

Since the 1970s, thermoset composites have been the preferred type of composite material because of their high failure strength, low creep, high elastic modulus with a relatively low cost compared to thermoplastic composites. Thermosetting composites have, however, limitations in terms of storage, aging and toughness other than processing constraints due to the long and strict multi-step processing. Because of these limitations extensive research with the goal of replacing thermoset matrices with thermoplastic ones, is on the rise [1].

Fiber reinforced thermoplastic composites are a promising alternative to thermoset composites because of their better damage tolerance and impact resistance. This kind of composites also have an high potential for recyclability and repairability which attracts the interests of researchers and developers as part of a broader focus towards sustainability. Last but not least thermoplastic composites also offer faster production cycles.

As a key partner in the aeronautical industry, Airbus Atlantic is working towards the development of thermoplastic composites to be used in the cockpit design. As a part of development and posterior certification process, a constitutive model, tailored towards fiber reinforced thermoplastics has to be proposed. The model here proposed is implemented in a finite element method solver software and it's being verified experimentally.

1.2 Objectives and scope of this project

The ultimate aim of this project is the development of a constitutive model designed, in particular, for carbon fiber reinforced thermoplastics for the use in the finite element method solver Abaqus CAE. In Abaqus is, indeed, possible to define the matherial behaviour through user subroutines: in this case these are the user material (UMAT) subroutine to be used with implicit analysis and the vectorized user material (VUMAT) to be used with explicit analysis.

This author contribution to the project starts in September 2024 and the main goals from then to March 2025 are the following ones:

- Test of the present day subroutine in order to identify and correct any flaws present in the code;
- Experimental tests to validate the present day subroutine;
- Initiation of studies regarding strain rate sensitivity whose results will be added to the subroutine;
- Perform experimental tests and process the obtained data to include in the subroutines experimentally identified material parameters.

Chapter 2

Theoretical background

During the development of the material model on which this work focuses on, many sources have been consulted in order to obtain an accurate picture of the most important behaviors of fiber reinforced composite materials. In the following sections insights about these materials are given.

2.1 Composite materials

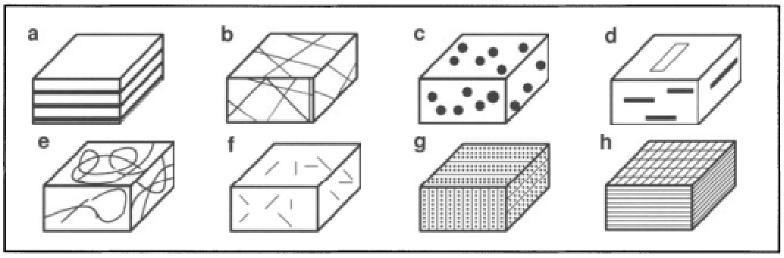

Figure 2.1: Examples of composite materials with different forms of constituents and distribution of the reinforcements. [2]

Composite materials morphology			
Type	*Description*	*Type*	*Description*
A	Laminate with uni- or bidirectional layers	E	Random arrangement of continuous fibres
B	Irregular reinforcement with long fibres	F	Irregular reinforcement with short fibres
C	Reinforcement with particles	G	Spatial reinforcement
D	Reinforcement with plate strapped particles	H	Reinforcement with surface tissues as mats, woven fabrics, etc.

Table 2.1: Description of the different distributions of reinforcement of Figure 2.1 [2]

Composite materials are defined as a combination of two or more materials called constituents that can be distinguished by physical or chemical properties, with the intention to produce a new material with augmented properties.

Different classes of composite materials can be delineated depending on the nature of their constituents. According to the nature of the matrix material it is possible to classify [2]:

- Organic matrix composites that are polymer resins with fillers. In this case the reinforcement can be mineral (like glass fibers), organic (like Kevlar fibers) or metallic;
- Mineral matrix composites that are ceramic with fibers or with metallic or mineral particles;
- Metallic matrix composites are metals with mineral or metallic fibers.

Composite materials can also be classified by the form and distribution of their constituents (Figure 2.1). The following distributions can be found:

- Fibrous reinforcement constituent
  - with continuous fibers: long fibers
  - with discontinuous fibers: short fibers
- Particulate reinforcement constituent with different possible shapes and arrangements:
  - random distribution
  - regular distribution with preferred orientations

Particular attention must be paid to fiber reinforced composites which are exceptionally important in the aeronautical field. These composite materials are made up of continuous matrix with fibers inside that act as the reinforcement. The fibers carry the majority of the load while the matrix provides support maintaining the fibers in the correct position. The matrix also transfers load between fibers and protects them from the external environment. Because of this distinction in the functions of the two constituents some material properties depends highly on the characteristics of the matrix like the shear strength, the strength along the direction transverse to the direction of the fibers and the strength longitudinal to the direction of the fibers when under compression.
Extremely interesting in high performance engineering applications are the fiber reinforced composites where the reinforcement is represented by carbon fibers.

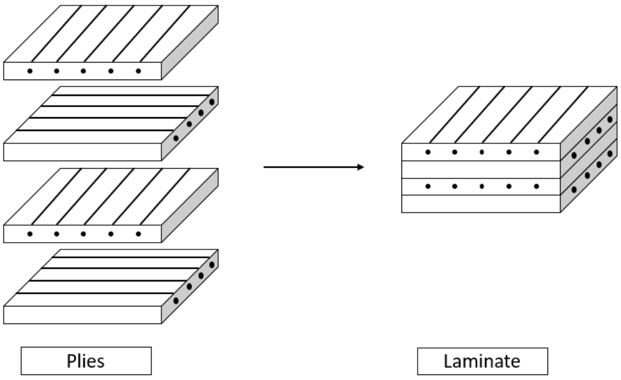

Figure 2.2: Fiber reinforced laminate structure

Commonly fiber reinforced composites are produced as plies, each ply contains the fibers, with specific orientations, soaked in the matrix (Figure 2.2).
Specifically, polymeric matrices are the most used for aeronautical applications because of their very low weight. There are two major groups of plastic matrix materials that can be described as follows:

- Thermoset matrices: extensively used for engineering applications. Composite materials with thermoset matrix and fibrous reinforcement compose a large portion of modern aircraft structures. One of the main issues of these materials is their low failure strain. As a consequence of this, composites will have low resistance to stresses in the thickness direction. These materials also absorb moisture that, as a result, reduces mechanical properties. Moreover, the manufacturing process of thermoset matrix composites is very long and complex.

- Thermoplastic matrices: they present high failure strain and consequently high impact resistance. Also the moisture absorbance is lower than their counterpart and solvent resistance is higher. The most interesting feature is that they can be remelted and reformed multiple times which creates the possibility to recycle it. In contrast the manufacturing cost increases with these matrices.

The material used in this work is a carbon fiber reinforced thermoplastic matrix, specifically PEAK matrix is considered (Polyaryletherketone).

2.2 Damage mechanisms

The foundation for modeling material behaviors lies in the understanding of their damage mechanisms. Before further details on the topic, it is necessary to differentiate the following concepts: fracture and damage .
Conventionally the term fracture implies the breakage of the material, or at a more fundamental level, breakage of its atomic bonds. This rupture results in the creation of internal surfaces. Whereas the term damage refers to all the irreversible changes brought in the material as a consequence of dissipating physical or chemical processes [3].

Some of the most common damage mechanisms observed in composite materials are shown in this section.

2.2.1 Fiber breakage

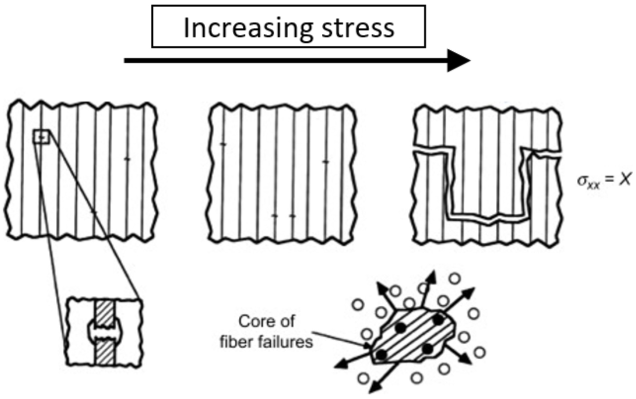

Figure 2.3: Sequence of failure events leading to failure under axial tensile loading [3]

Fiber breakage is one of the most negative factors that affect the mechanical behavior of fiber reinforced composites. This phenomena can occur if the composite is loaded in tension along the fiber direction and can take place at load levels lower than the failure load. Fiber breakages occur at weak points along fibers, that is where fiber defects are sufficient to make that area reach the fiber failure stress (Figure 2.3). As load increases more fibers fail in the vicinity of already broken fibers [4].
The progression of fiber breakage is stochastic and depends strongly on the conditions of the failure region. Because of this the fiber failure process can be described just in statistical therms.
It is, therefore, quite arduous to predict the longitudinal tensile strength of a composite.

2.2.2 Matrix micro-cracking

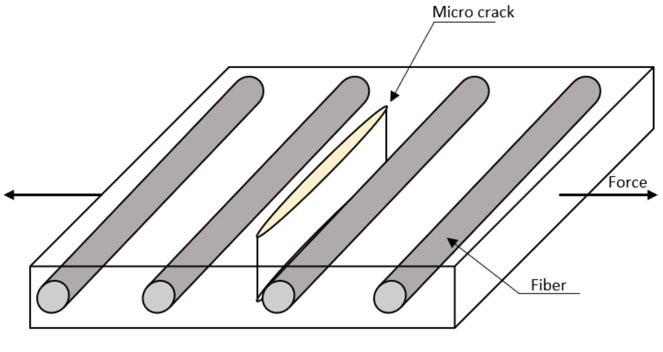

Figure 2.4: Schematic representation of matrix micro-cracking

Matrix micro-cracks are intralaminar or ply cracks that traverse the thickness of the ply running parallel to the fiber of that ply. Since these cracks are typically perpendicular to the loading direction they are also called transverse cracks and they form predominantly in plies off-axis with loading direction. This phenomenon can be observed during tensile loading, fatigue loading or thermocycling and it is a consequence of the fact that the mechanical properties of the composite in the direction transverse to fibers orientation depends mostly on matrix properties. Matrix material generally has poor mechanical properties.

The effect of micro-cracking is degradation of mechanical properties including effective moduli, change in the Poisson ratio and thermal expansion coefficient.

As a secondary effect micro-cracking is the basis for other damage forms like delamination and fiber breaks [5].

2.2.3 Fiber-matrix debonding

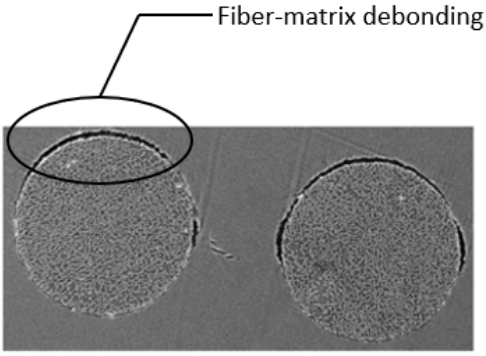

Figure 2.5: X-ray microtomography observation of interfacial debonding [6]

Fiber-matrix debonding concerns the separation of the fibers from the surrounding matrix. The bond between matrix and fibers has a major impact on the performance of the fiber reinforced composite because it determines how effectively stresses are shifted between the two constituents.

Because of the dissimilar mechanical properties of fibers and matrix, they tend to have distinct deformations as loading increases. When this difference is high enough the resulting stresses result in the separation of fiber and matrix along their interface (Figure 2.5).

2.2.4 Delamination

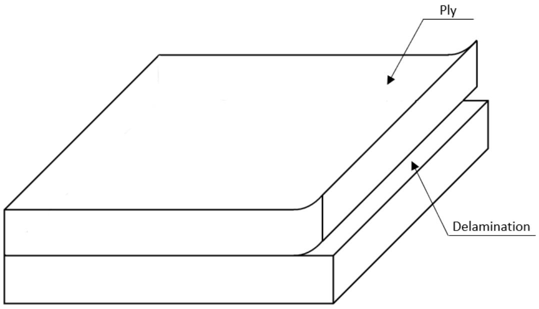

Figure 2.6: Schematic representation of delamination process

The leading weakness of fiber reinforced laminate materials is their little interlaminar strength. Because of this, delamination between layers interfaces is a very common and critical problem for these materials. The term delamination refers to the separation of adjacent layers due to weakening of the interface layer between them (Figure 2.6). The process of delamination can be triggered by manufacturing process of the laminate or during the operation service of the composite.
Delamination can occur because when the material is loaded in in-plane direction, defects can generate normal and shear stresses through the thickness. Delamination can also happen as a result of previous interlaminar cracking [7].

2.2.5 Fiber micro-buckling and kinking

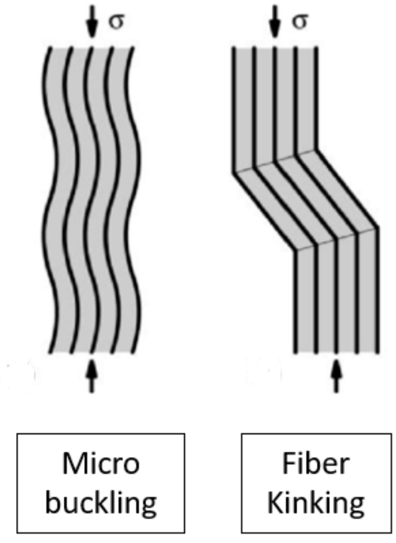

Figure 2.7: Schematic representation of fiber micro-buckling and kinking [8]

The term fiber micro-buckling refers to the phenomenon because of which fibers under compressive load in fiber direction undergo transverse displacement caused by the buckling effect (2.7). There are two general ways in which this instability can occur:

- elastic buckling of the fiber that involves also deformation of the matrix. This phenomenon is generally referred to as fiber micro buckling;
- Plastic deformation of the fiber known as fiber kinking.

Micro-buckling may occur as a periodic mode with periodic deformation of the fibers and shear of the matrix but also as non-periodic mode in which shear is negligible and the process is dominated by transverse deformations. The matrix shear properties and material imperfections play an important role in the micro-buckling mechanical modes. The kinking process, instead, is governed by shear stresses and can be a consequence of misalignment of the fibers during their manufacturing process [9].

2.3 Strain rate effect

Composite materials are widely used for applications concerning dynamic loads. Works on dynamic characterization of composite materials is relatively limited compared to quasi static-tests because of the difficulty of high strain-rate testing and data interpretation. Because of this, it is very difficult to find unanimous conclusions in literature regarding high strain rate composite material behavior. H.M. Hsiao and I.M. Daniel tested both Carbon/Epoxy and Carbon/PEEK materials [10] and because of the similarities of these materials with the one under study their result seem the most meaningful in the context of this research.

Transverse compressive behavior

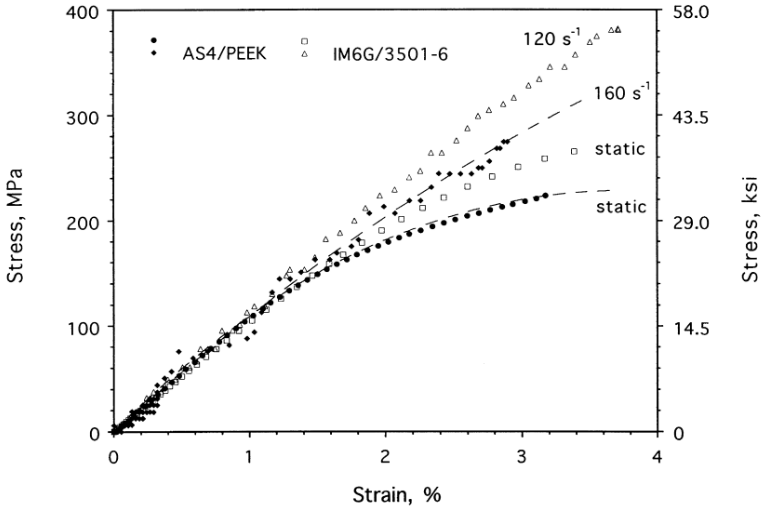

Figure 2.8: Comparison of transverse compressive stress–strain curves between AS4/APC2 carbon/PEEK and IM6G/3501-6 carbon/epoxy under quasi-static and high strain rate loading [10]

Figure 2.8 shows transverse compressive stress-strain curves to failure under quasi-static and high strain rate loading. It is clear that the behavior is strongly influenced by strain-rate. The transverse strength, which is dominated by matrix's properties, increases with the strain rate. A similar phenomenon happens with the initial modulus but no effect seems to appear looking at the ultimate strain. The material stiffens as the strain rate increases and this phenomena is more significant in the non linear region. Hsiao proposes two explanations:

- Viscoelastic nature of the polymeric matrix
- Time dependent nature of accumulating damage: at higher rates damage does not have time to develop so the damage accumulation process has a lower effect on the stress-strain curve

Both Carbon/PEEK and Carbon/Epoxy show this behavior

In-plane shear behavior

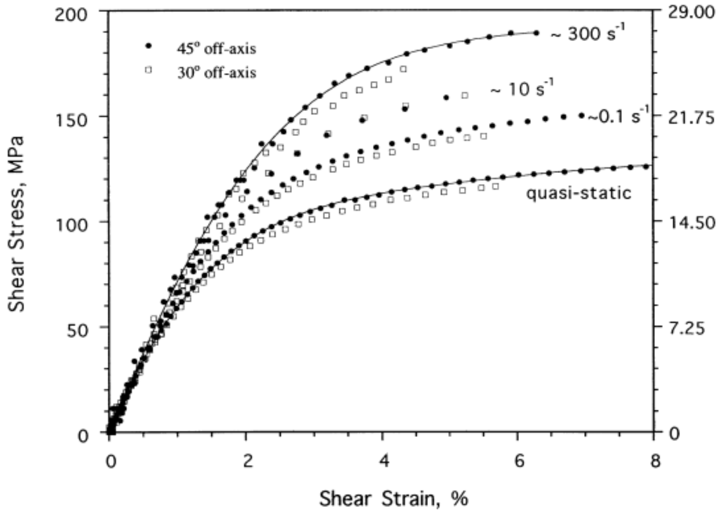

Figure 2.9: Comparison of shear stress–strain curves obtained from 30° and 45° off-axis tests under quasi-static and high strain rate compressive loading [10]

Figure 2.9 shows the compressive shear stress-strain curves obtained from 30° and 45° off-axis specimens under quasi-static and high strain-rates loading. It appears that the shear stress-strain curves obtained from different angles agree for similar strain rate and for both cases a strong behavior dependence from strain-rate can be observed. The yield point increases with increasing strain rate just as strength and initial modulus.

Longitudinal compressive behavior

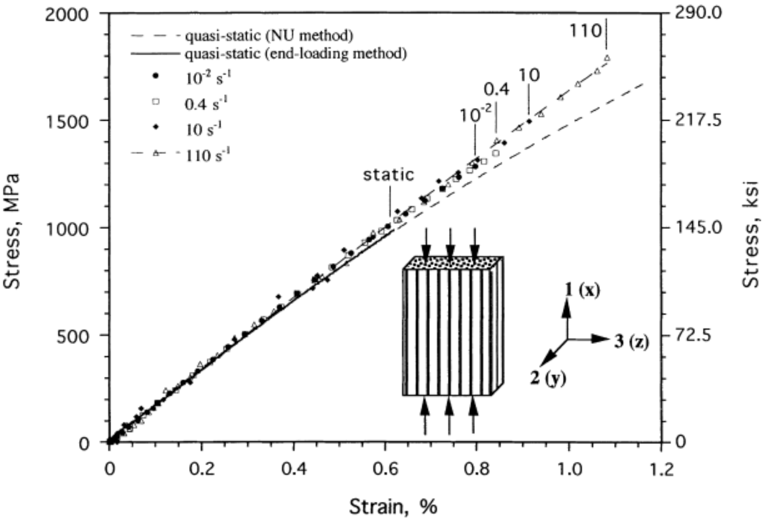

Figure 2.10: Longitudinal compressive stress–strain curves for unidirectional IM6G/3501-6 carbon/epoxy under quasi-static and high strain rate loading [10]

Longitudinal compressive stress-strain curves under quasi-static and high strain-rate loading are shown in Figure 2.10. The stiffening behavior in the non-linear range can be observed also in this loading condition. The magnitude of the stiffening is way lower compared to the transverse behavior. In this case both the strength and ultimate strain are higher in the high strain rate loading condition than their static values. This last phenomena can be due to shear behavior of the composite and the change in failure modes. Indeed, longitudinal compressive failure is related to in-plane shear response of the composite in the presence of even the slightest initial fiber misalignment [11]. The longitudinal compressive strength can be expressed as follows:

$$F_{1c} = \frac{\tau^*}{\phi + \gamma^*} \tag{2.1}$$

where ϕ is the initial fiber misalignment, τ^* and γ^* are the values of shear stress and strain defined as in Figure 2.11.

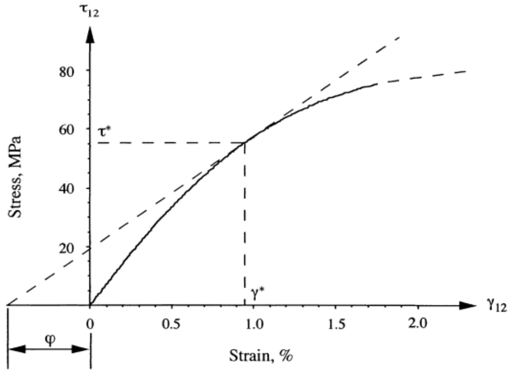

Figure 2.11: Graphical determination of longitudinal compressive strength [10]

It is clear that, if the in-plane shear behavior stiffens substantially with increasing strain rate than this would lead to the increase in longitudinal compressive strength.

Finally it is widely accepted that the longitudinal tensile properties of unidirectional carbon-epoxy composites are not strain rate sensitive as demonstrated in a study by J. Harding and L.M. Welsh [12] [13].

2.4 Numerical theories

In this section the theory behind the numerical model used for this work is presented.

2.4.1 Orthotropic materials macro-mechanics

Constitutive equations define material behavior of a structure under applied loads. The most general form of the linear constitutive equation for infinitesimal deformations is known as the generalized Hooke law [14]:

$$\sigma_{ij} = C_{ijkl}\epsilon_{kl} \tag{2.2}$$

Where C_{ijkl} is called stiffness tensor and generally has 81 scalar components. This number can be reduced to 36 considering the symmetry of σ_{ij} and ϵ_{kl}. The constitutive equation can therefore be expressed in an alternate form using single subscript notation for stresses and strains and double subscript notation for the material stiffness coefficients:

$$\sigma_i = C_{ij}\epsilon_j \tag{2.3}$$

This notation is called engineering notation or Voigt-Kelvin notation.

In matrix notation the previous equation can be rewritten as follows:

$$\begin{Bmatrix}\sigma_1\\ \sigma_2\\ \sigma_3\\ \sigma_4\\ \sigma_5\\ \sigma_6\end{Bmatrix} = \begin{pmatrix} C_{11} & C_{12} & C_{13} & C_{14} & C_{15} & C_{16}\\ C_{21} & C_{22} & C_{23} & C_{24} & C_{25} & C_{26}\\ C_{31} & C_{32} & C_{33} & C_{34} & C_{35} & C_{36}\\ C_{41} & C_{42} & C_{43} & C_{44} & C_{45} & C_{46}\\ C_{51} & C_{52} & C_{53} & C_{54} & C_{55} & C_{56}\\ C_{61} & C_{62} & C_{63} & C_{64} & C_{65} & C_{66}\end{pmatrix} \begin{Bmatrix}\epsilon_1\\ \epsilon_2\\ \epsilon_3\\ \epsilon_4\\ \epsilon_5\\ \epsilon_6\end{Bmatrix} \tag{2.4}$$

Orthotropic materials, like one layer of unidirectional fiber reinforced composite material, show three mutually orthogonal planes of symmetry. Because of this the number of independent elastic coefficient is reduced to 9 and the constitutive equation changes in:

$$\begin{Bmatrix}\sigma_1\\ \sigma_2\\ \sigma_3\\ \sigma_4\\ \sigma_5\\ \sigma_6\end{Bmatrix} = \begin{pmatrix} C_{11} & C_{12} & C_{13} & 0 & 0 & 0\\ C_{12} & C_{22} & C_{23} & 0 & 0 & 0\\ C_{13} & C_{23} & C_{33} & 0 & 0 & 0\\ 0 & 0 & 0 & C_{44} & 0 & 0\\ 0 & 0 & 0 & 0 & C_{55} & 0\\ 0 & 0 & 0 & 0 & 0 & C_{66}\end{pmatrix} \begin{Bmatrix}\epsilon_1\\ \epsilon_2\\ \epsilon_3\\ \epsilon_4\\ \epsilon_5\\ \epsilon_6\end{Bmatrix} \tag{2.5}$$

Classically material's characteristics are determined through laboratory tests in terms of engineering constants such as Young modulus (E), shear modulus (G)

and Poisson ratio (ν). The 9 independent coefficients of the Hooke's equation can be expressed using the material engineering constants as follows:

$$C_{11} = \frac{1-\nu_{23}\nu_{32}}{E_2E_3\Delta} \quad C_{12} = \frac{\nu_{21}+\nu_{31}\nu_{23}}{E_2E_3\Delta} \quad C_{13} = \frac{\nu_{31}+\nu_{21}\nu_{32}}{E_2E_3\Delta} \tag{2.6}$$

$$C_{22} = \frac{1-\nu_{13}\nu_{31}}{E_1E_3\Delta} \quad C_{23} = \frac{\nu_{32}+\nu_{12}\nu_{31}}{E_1E_3\Delta} \quad C_{33} = \frac{1-\nu_{12}\nu_{21}}{E_1E_2\Delta} \tag{2.7}$$

$$C_{44} = G_{23} \quad C_{55} = G_{31} \quad C_{66} = G_{12} \tag{2.8}$$

in which:

$$\Delta = \frac{1-\nu_{12}\nu_{21}-\nu_{23}\nu_{32}-\nu_{13}\nu_{31}-2\nu_{21}\nu_{32}\nu_{13}}{E_1E_2E_3} \tag{2.9}$$

For the Poisson ratio the following relation is valid:

$$\frac{\nu_{ij}}{E_i} = \frac{\nu_{ji}}{E_j} \tag{2.10}$$

The constitutive equations are defined in terms of stresses and strains components that are referred to a coordinate system which coincides with the principal material coordinate system (Figure 2.12).

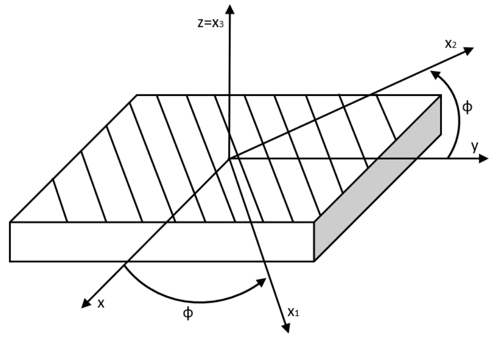

Figure 2.12: Composite plate coordinates systems

Unfortunately in the problem formulation this coordinate system does not coincide with the general laminate coordinate system called problem coordinate system. It is also necessary to consider that every lamina of the laminate has its own material coordinate system with its specific orientation. The relation between the material coordinate system ($x_1\ x_2\ x_3$) and the problem coordinates ($x\ y\ z$) is expressed below:

$$\begin{Bmatrix} x_1 \\ x_2 \\ x_3 \end{Bmatrix} = \begin{pmatrix} cos\phi & sin\phi & 0 \\ -sin\phi & cos\phi & 0 \\ 0 & 0 & 1 \end{pmatrix} \begin{Bmatrix} x \\ y \\ z \end{Bmatrix} = [L] \begin{Bmatrix} x \\ y \\ z \end{Bmatrix} \tag{2.11}$$

The inverse of the previous equation is:

$$\begin{Bmatrix} x \\ y \\ z \end{Bmatrix} = \begin{pmatrix} cos\phi & -sin\phi & 0 \\ sin\phi & cos\phi & 0 \\ 0 & 0 & 1 \end{pmatrix} \begin{Bmatrix} x_1 \\ x_2 \\ x_3 \end{Bmatrix} = [L]^T \begin{Bmatrix} x_1 \\ x_2 \\ x_3 \end{Bmatrix} \tag{2.12}$$

Considering that each quantity related to the material reference system is indicated by the subscript m and those related to the problem reference systems by the subscript p, it results:

$$\{\sigma\}_p = [L]^T\{\sigma\}_m[L] \quad \epsilon_p = [L]^T\{\epsilon\}_m[L] \tag{2.13}$$

The material stiffness are transformed from the material coordinate system to the problem coordinates as follows:

$$\{\sigma\}_p = [L]^T\{\sigma\}_m[L] = [L]^T[C]_m\{\epsilon\}_m[L] = [L]^T[L][C]_m[L][L]^T\{\epsilon\}_p = [C]_p\{\epsilon\}_p \tag{2.14}$$

Defining $[Q] = [C]_p$, $[C] = [C]_m$ and $[T] = [L]^T[L]$:

$$[Q] = [T][C][T]^T \tag{2.15}$$

This last equation can be written for each layer of the considered laminate.

2.4.2 Classical lamination theory

The classical lamination theory (CLT) represents one of the fundamental simplified models used to analyze the mechanical behavior of multi-layered materials. Thanks to this theory it is possible to consistently proceed directly from the composite basic building block, the lamina, to the end result, the structural laminate. The process is based on assumptions that enable to transform a complicated three dimensional elasticity problem, into a solvable two dimensional mechanics of deformable bodies problem.

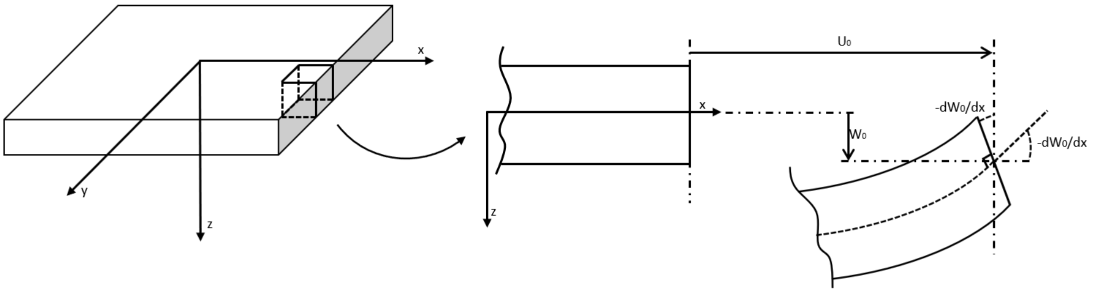

Figure 2.13: Classical lamination theory hypothesis scheme

The laminate is presumed to consist of perfectly bonded laminae and the bonds are presumed to be infinitesimally thin as well as non shear-deformable. That means that the displacements are continuous across lamina boundaries so that no lamina can slip relative to another. The laminate, therefore, acts as a single layer with very special properties [14].

The previous assumptions lead to the application of Kirchhoff theory to define mechanical behavior of the lamina. This classical lamination theory is thus based on the Kirchhoff hypothesis (Figure 2.13):

1. Straight lines perpendicular to the mid-surface (i.e transverse normals) before deformation, remain straight after deformation
2. Transverse normals do not experience elongation
3. Transverse normals rotate such that they remain perpendicular to the mid-surface after deformation.

As a result of the first two assumptions it is possible to conclude that the transverse normal displacement is independent of the thickness coordinate and the transverse normal strain is zero ($\epsilon_{zz} = 0$). The consequence of the last assumption is that the shear strains are zero ($\gamma_{xz} = \gamma_{xz} = 0$).
The plate displacement field, because of these assumptions, is:

$$\begin{gathered} u(x,y,z) = u_0(x,y) - z\frac{\delta w_0}{\delta x} \\ v(x,y,z) = v_0(x,y) - z\frac{\delta w_0}{\delta y} \\ w(x,y,z) = w_0(x,y) \end{gathered} \tag{2.16}$$

The strains are linked with the displacement and they have a constant component and a component linear in the variable z:

$$\begin{Bmatrix} \epsilon_{xx} \\ \epsilon_{yy} \\ \epsilon_{xy} \end{Bmatrix} = \begin{Bmatrix} \epsilon_{xx}^{(0)} \\ \epsilon_{yy}^{(0)} \\ \epsilon_{xy}^{(0)} \end{Bmatrix} + z \begin{Bmatrix} \epsilon_{xx}^{(1)} \\ \epsilon_{yy}^{(1)} \\ \epsilon_{xy}^{(1)} \end{Bmatrix} \tag{2.17}$$

$$\{\epsilon^0\} = \begin{Bmatrix} \epsilon_{xx}^{(0)} \\ \epsilon_{yy}^{(0)} \\ \epsilon_{xy}^{(0)} \end{Bmatrix} = \begin{Bmatrix} \frac{\delta u_0}{\delta x} \\ \frac{\delta v_0}{\delta y} \\ \frac{\delta u_0}{\delta y} + \frac{\delta v_0}{\delta x} \end{Bmatrix} \quad \{\epsilon_1\} = \begin{Bmatrix} \epsilon_{xx}^{(1)} \\ \epsilon_{yy}^{(1)} \\ \epsilon_{xy}^{(1)} \end{Bmatrix} = \begin{Bmatrix} -\frac{\delta^2 w_0}{\delta x^2} \\ -\frac{\delta^2 w_0}{\delta y^2} \\ -2\frac{\delta^2 w_0}{\delta x \delta y} \end{Bmatrix} \tag{2.18}$$

where the constant components ($\epsilon_{xx}^{(0)}, \epsilon_{yy}^{(0)}, \epsilon_{xy}^{(0)}$) are the membrane strains while coefficients of the linear component ($\epsilon_{xx}^{(1)}, \epsilon_{yy}^{(1)}, \epsilon_{xy}^{(1)}$) are the bending strains, also known as curvatures.

The simplified kinematic assumptions used in this theory to move from a three dimensional structure to a two dimensional one generate a phenomena called Poisson locking. Specifically, this phenomena is due to the use of plane strain hypothesis in a shell theory. The analysis of shell problems is, in fact, often associated to plane stress assumption while plane strain hypothesis is usually used for beam theories. Because of the Poisson locking equivalent single layer analysis with transverse normal displacement constant or linear through the thickness do not lead to the 3D solution in case of thin plate.

In order to avoid this problem it is necessary to force the following condition:

$$\sigma_{zz} = 0 \tag{2.19}$$

By imposing this condition in the Hooke's law it is possible to calculate the reduced stiffness coefficients by imposing the new condition in σ_{zz} and calculating the new ϵ_{zz}. Considering an orthotropic material:

$$\sigma_{zz} = C_{13}\epsilon_{xx} + C_{23}\epsilon_{yy} + C_{33}\epsilon_{zz} = 0 \tag{2.20}$$

$$\epsilon_{zz} = -\frac{C_{13}}{C_{33}}\epsilon_{xx} - \frac{C_{23}}{C_{33}}\epsilon_{yy} \tag{2.21}$$

The so calculated ϵ_{zz} is then substituted in Hooke's law equations for σ_{xx} and σ_{yy} finally obtaining the reduced coefficients.

The final constitutive equation for the classical lamination theory considering all the assumptions is the following one:

$$\begin{Bmatrix} \sigma_{xx} \\ \sigma_{yy} \\ \sigma_{xy} \end{Bmatrix} = \begin{pmatrix} \bar{C}_{11} & \bar{C}_{12} & 0 \\ \bar{C}_{12} & \bar{C}_{22} & 0 \\ 0 & 0 & \bar{C}_{66} \end{pmatrix} \begin{Bmatrix} \epsilon_{xx} \\ \epsilon_{yy} \\ \epsilon_{xy} \end{Bmatrix} \tag{2.22}$$

with

$$\bar{C}_{11} = C_{11} - \frac{C_{13}^2}{C_{33}} \quad \bar{C}_{12} = C_{12} - \frac{C_{13}C_{23}}{C_{33}} \quad \bar{C}_{22} = C_{22} - \frac{C_{23}^2}{C_{33}} \quad \bar{C}_{66} = C_{66} \tag{2.23}$$

A laminate shell is loaded by stress resultants which are integrals of the stress components through the thickness. The following integrals can be defined along the thickness in case of multi-layered plate:

$$\begin{Bmatrix} N_{xx} \\ N_{yy} \\ N_{xy} \end{Bmatrix} = \int_{\frac{h}{2}}^{\frac{h}{2}} \begin{Bmatrix} \sigma_{xx} \\ \sigma_{yy} \\ \sigma_{xy} \end{Bmatrix} dz \qquad \begin{Bmatrix} M_{xx} \\ M_{yy} \\ M_{xy} \end{Bmatrix} = \int_{\frac{h}{2}}^{\frac{h}{2}} \begin{Bmatrix} \sigma_{xx} \\ \sigma_{yy} \\ \sigma_{xy} \end{Bmatrix} zdz \tag{2.24}$$

Through the substitution of the 2.23 equation the following relations are obtained:

$$\begin{Bmatrix} N_x \\ N_y \\ N_{xy} \\ M_x \\ M_y \\ M_{xy} \end{Bmatrix} = \begin{pmatrix} A_{11} & A_{12} & A_{14} & B_{11} & B_{12} & B_{14} \\ A_{21} & A_{22} & A_{24} & B_{12} & B_{22} & B_{24} \\ A_{14} & C_{24} & C_{44} & B_{14} & B_{24} & B_{44} \\ B_{11} & B_{12} & B_{14} & D_{11} & D_{12} & D_{14} \\ B_{12} & B_{22} & B_{24} & D_{12} & D_{22} & D_{24} \\ B_{14} & B_{24} & B_{44} & D_{14} & D_{24} & D_{44} \end{pmatrix} \begin{Bmatrix} \epsilon_x^0 \\ \epsilon_y^0 \\ \epsilon_{xy}^0 \\ \kappa_x \\ \kappa_y \\ \kappa_{xy} \end{Bmatrix} \tag{2.25}$$

In wich:

$$(A_{ij}, B_{ij}, D_{ij}) = \int_{-\frac{h}{2}}^{\frac{h}{2}} \bar{C}_{ij}(1, z, z^2)dz = \sum_{k=1}^{N} \int_{z_k}^{z_k+1} \bar{C}_{ij}^{(k)}(1, z, z^2)dz \tag{2.26}$$

with k representing the number of the considered layer of the N layers composite material. These new coefficients have a physical significance:

- A_{ij} is the extensional stiffness
- D_{ij} is the bending stiffness
- B_{ij} is the bending-extensional coupling stiffness

The classical lamination theory, while being very useful and at the base of every commercial structural analysis software, does not take into account many phenomena that occur inside a composite plate during loading.

Chapter 3

Material model and properties

3.1 UMAT and VUMAT subroutines

This work presents, as one of the main objectives, the validation of the material model previously developed at ISAE Supaero. In this chapter the main features of this material model are discussed but for a complete understanding of it reference should be made to the previous work of L.L. Pérez [15] and G.L.M. da Rocha Coelho [16].

The material models are implemented in the ABAQUS finite element solver through a User Material (UMAT) subroutine and a Vectorized User Material (VUMAT) subroutine. Both options were developed because the UMAT provides higher fidelity results for static simulations, where convergence of the implicit formulation is achievable while the VUMAT, is especially useful for dynamic cases. In this last case, given the high non-linearity, the convergence of the implicit formulation is difficult. A scheme of the ABAQUS solver stages is presented in Figure 3.1.

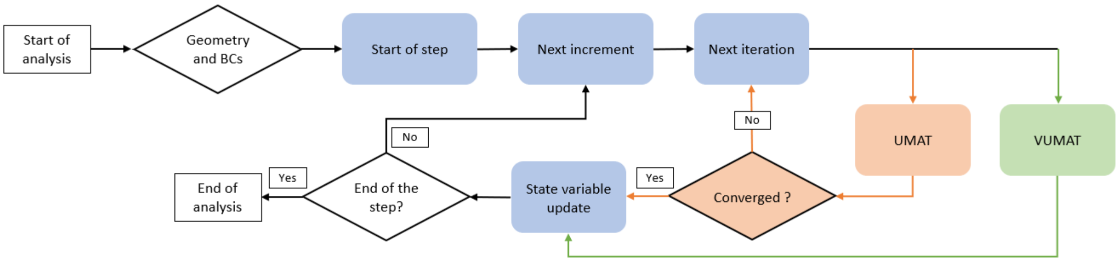

Figure 3.1: Simplified flowchart of the ABAQUS solver

3.1.1 Logical scheme

The scheme in Figure 3.2 shows the logical flow of the UMAT and VUMAT subroutine. Everything is furtherly specified in the following sections.

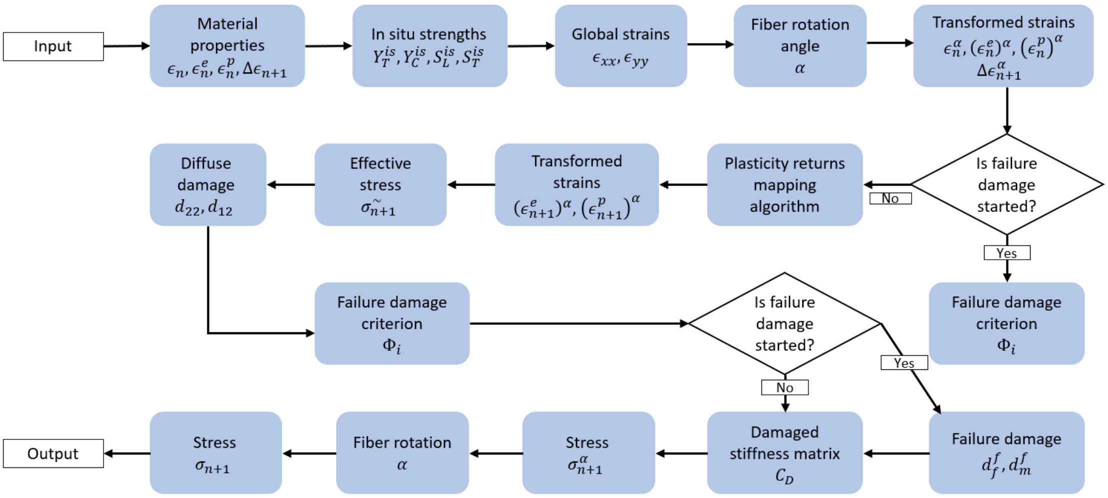

Figure 3.2: UMAT and VUMAT subroutines flowchart

3.1.2 Required inputs

The properties given in Table 3.1 are the necessary inputs to run the UMAT and VUMAT subroutines:

Props(1) E_1
Props(2) E_2
Props(3) E_3
Props(4) G_{12}
Props(5) G_{13}
Props(6) G_{23}
Props(7) ν_{12}
Props(8) ν_{13}
Props(9) ν_{23}
Props(10) ϵ_{11}^{ft}
Props(11) ϵ_{22}^{ft}
Props(12) ϵ_{33}^{ft}
Props(13) ϵ_{11}^{fc}
Props(14) ϵ_{22}^{fc}
Props(15) ϵ_{33}^{fc}
Props(16) ϵ_{12}^{f}
Props(17) ϵ_{13}^{f}
Props(18) ϵ_{23}^{f}
Props(19) χ_T
Props(20) χ_C
Props(21) Y_T
Props(22) Y_C
Props(23) S_L
Props(24) S_T
Props(25) α_0
Props(26) β
Props(27) G_{fc}^T
Props(28) G_{fc}^C
Props(29) G_{mc}^T
Props(30) G_{mc}^C
Props(31) G_{mc}^S
Props(32) η
Props(33) In situ configuration
Props(34) t
Props(35) η_T
Props(36) η_L
Props(37) Θ_0
Props(38) $\frac{E_1^c}{E_1}$
Props(39) Diffuse damage model

Table 3.1: Property vector inputted at the beginning of each iteration of the subroutines

In the VUMAT subroutine one further input needs to be given: **Props(40)** which is the strain at which the user wants the deletion of the element to happen. This variable is not necessary in the UMAT subroutine because it doesn't have the element deletion option in it.

3.1.3 In situ effect

Considering a multi-layered composite there is an effect that appear when the plies are oriented with different directions: the in situ effect. Because of this response when a ply is constrained between plies with different orientation, it shows higher transverse tensile and shear strengths compared to its equivalent in a unidirectional laminate. The in situ strength depends also on the number of plies and on their orientation [17]. The UMAT model calculates the new strengths produced by this effect known as in situ strengths. Their calculus depends on the configuration of the considered ply.

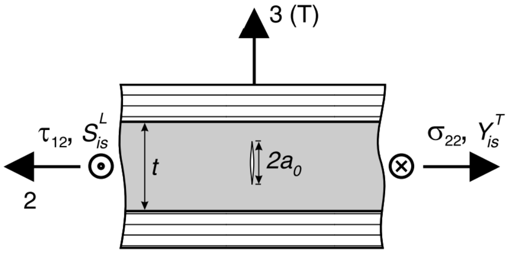

Figure 3.3: Thick embedded ply [17]

The thick ply configuration (Figure 3.3) is considered when transverse cracks in the matrix are shorter than the ply thickness. In this case the in-situ transverse tensile strength is calculated as follows:

$$Y_T^{is} = \sqrt{\frac{2G_{Ic}(T)}{\pi a_0 \Lambda_{22}^0}} \tag{3.1}$$

where $G_{Ic}(T)$ is the intralaminar critical energy release rate for mode 1 crack growth in direction 3 and Λ_{22}^0 is a coefficient that takes into account the engineering constants of the ply. The in-situ in-plane shear strength can be calculated as follows:

$$S_L^{is} = \sqrt{\frac{(1+\beta\phi G_{12})^{\frac{1}{2}} - 1}{3\beta G_{12}}} \tag{3.2}$$

where β is a parameter that defines the non-linearity of the relationship between shear stress and shear strain and ϕ is:

$$\phi = \frac{12S_L^2}{G_{12}} + 18\beta S_L^4 \tag{3.3}$$

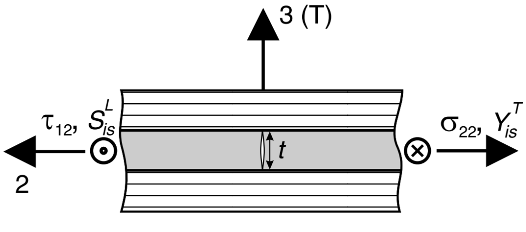

Figure 3.4: Thin embedded ply [17]

The thin ply configuration (Figure 3.4) is considered when the length of the transverse cracks in the matrix is equal to the thickness of the ply. In this case the in situ strengths are calculated as follows:

$$Y_T^{is} = \sqrt{\frac{8G_{Ic}(L)}{\pi t \Lambda_{22}^0}} \quad S_L^{is} = \sqrt{\frac{8G_{IIc}(L)}{\pi t \Lambda_{44}^0}} \tag{3.4}$$

where t is the ply thickness, G_{Ic} and G_{IIc} are the intralaminar critical energy release rate, respectively, for mode 1 and 2 of crack growth in direction 1.

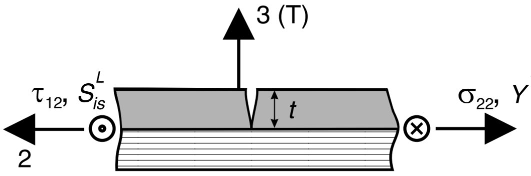

Figure 3.5: Thin outer ply [17]

The last case considered is the thin outer ply (Figure 3.5) that corresponds to the first or last ply of the laminate. Considering the intralaminar energy release rate for mode 1 crack growth in the direction 1, the in-situ tensile transverse strength is calculated as follows:

$$Y_T^{is} = \sqrt{\frac{4G_{Ic}(L)}{\pi t \Lambda_{22}^0}} \tag{3.5}$$

while the in-situ in-plane shear strength can be calculated with equation 3.2 using the following ϕ:

$$\phi = \frac{24G_{IIc}(L)}{\pi t} \tag{3.6}$$

The in-situ compressive transverse strength (Y_C^{is}) and the in-situ through the thickness shear strength (S_T^{is}) are calculated using the expression proposed in Catalanotti et al. [18]:

$$Y_C^{is} = -\frac{S_L^{is}(2cos^2(\alpha_0) - 1)}{\eta_L cos^2(\alpha_0)} \quad S_T^{is} = \frac{S_L^{is}(2sin^2(\alpha_0) - 1)}{2\eta_L\sqrt{1 - sin^2(\alpha_0)}sin(\alpha_0)} \tag{3.7}$$

where $\alpha_0 = 53 \pm 2°$ [19] is the fracture angle under pure transverse compression and η_L is the longitudinal friction coefficient.

3.1.4 Fiber rotation

When a composite material is loaded, fibers reorient themselves towards the loading direction. This phenomena leads to an increase in the apparent axial modulus and intra-ply stresses of the material. The rotation can be up to 10°.

Different methodologies exists to evaluate the effect of fiber rotation and the one selected for the UMAT and VUMAT sub-routines is the one used by J.Fuller and M.Wisnom [20]. The fibers are considered inextensible and they act in a scissor motion, realigning towards the direction of applied stress. The new fiber angle (θ') depends on the strains (ϵ_x and ϵ_y):

$$\theta' = arctan\left(\frac{tan(\theta) + \epsilon_y}{1 + \epsilon_x}\right) \tag{3.8}$$

where θ is the original fiber orientation, i.e the ply orientation.

The two dimensional formulation previously presented, needs some modifications in order to take into account all the strains components of a three dimensional case.

3.1.5 Plasticity effect

In order to create a plasticity model it is necessary to define a plastic potential function, a hardening law and an algorithm that calculates plastic deformation for each strain increment that in this case corresponds to each time step of the ABAQUS analysis.

For the UMAT subroutine the Hill-type plastic potential function [16] independent of longitudinal effective stresses is chosen:

$$f_p(\tilde{\sigma}) = \sqrt{\tilde{\sigma}_{12}^2 + \tilde{\sigma}_{13}^2 + \tilde{\sigma}_{23}^2 + c^2(\tilde{\sigma}_{22}^2 + \tilde{\sigma}_{33}^2)} \tag{3.9}$$

where c is a coupling parameter that describes the level of plastic deformation developed under normal loads compared to shear loads [21].

The hardening law is obtained from experimental tensile tests performed on $[\pm 45]_{2s}$ AS4/PEEK coupons:

$$\sigma_y(p) = K(p + \beta_p)^{\alpha_p} \tag{3.10}$$

where K,α_p and β_p are obtained form the experimental data

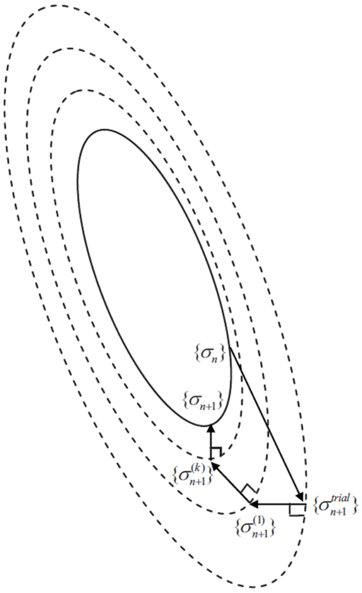

Figure 3.6: Stress returns corresponding to CPA algorithm [22]

The computing algorithm chosen is a modified version of the cutting plane algorithm (CPA) as presented in J.Huang and D.V.Grifiths [22]. The way plastic strains is calculated at each step is unfolded in the following bullet list:

1. Trial stress:
   The stress that would be obtained if the strain increment during this time step were purely elastic (i.e the trial effective stress) is calculated:

   $$\tilde{\sigma}_{trial} = C : (\epsilon_{n+1} - \epsilon_n^p) \tag{3.11}$$

   where ϵ_{n+1} is the total strain tensor at the end of the current time step, its value is known because ABAQUS calculates the total strain increment in each step, and ϵ_n^p is the plastic strain tensor at the end of the previous time step. C is the stiffness tensor written in the $6 * 6$ matrix form as seen in equation 2.5.

2. Initial check of the yield condition:
   The yield function is evaluated using the trial effective stress and the value of the accumulated plastic strain at the beginning of every time step (p_n):

   $$F_p(\tilde{\sigma}_{trial}, p_n) = f_p(\tilde{\sigma}_{trial}) - \sigma_y(p_n) \tag{3.12}$$

   If $F_p(\tilde{\sigma}_{trial}, p_n) \leq 0$ only elastic deformation is taking place and elastic strain, plastic strain and accumulated plastic strain are respectively calculated as follows:

   $$\epsilon_{n+1}^e = \epsilon_{n+1} - \epsilon_n^p \tag{3.13}$$

   $$\epsilon_{n+1}^p = \epsilon_n^p \tag{3.14}$$

   $$p_{n+1} = p_n \tag{3.15}$$

   In this case all the following step can be skipped. Alternatively, if $F_p(\tilde{\sigma}_{trial}, p_n) > 0$ plastic deformation is occurring and to calculate the value of the plastic strain, the value of the plastic strain rate $\dot{\lambda}$ for which $F_p = 0$ must be found. That is because of the Kuhn-Tucker condition:

   $$F_p(\tilde{\sigma}_{n+1}, p_{n+1}) = 0 \tag{3.16}$$

   It is important to note that numerically finding the exact value of $\dot{\lambda}$ would add too much computational time so a tolerance value is used. The condition to be met is therefore $|F_p| \leq TOL$.

3. Initialization:
   Before the iterative CPA algorithm can be used, some initial values needs to be set:

   $$F_p^0 = F_p(\tilde{\sigma}_{trial}, p_n) \quad \epsilon_{n+1}^{p^0} = \epsilon_n^p \quad p_{n+1}^0 = p_n \tag{3.17}$$

   The initial value for the gradient of the yield function with respect to stresses of plastic flow is defined as follows:

   $$a^0 = \left.\frac{\delta F_p}{\delta \tilde{\sigma}}\right|_{\tilde{\sigma}_{trial,pn}} = \frac{1}{f_p(\tilde{\sigma}_{trial})} \begin{Bmatrix} 0 \\ c^2\tilde{\sigma}_{22trial} \\ c^2\tilde{\sigma}_{33trial} \\ \tilde{\sigma}_{12trial} \\ \tilde{\sigma}_{13trial} \\ \tilde{\sigma}_{23trial} \end{Bmatrix} \tag{3.18}$$

4. Plastic strain rate:
   This is the first step of the CPA algorithm. The plastic strain rate is calculated as follows:
$$\dot{\lambda}^{i+1} = \frac{F_p^i}{a^{i^T} : C : a^i + H} \tag{3.19}$$
   where H^i is calculated as:
$$H^i = \left.\frac{\delta \sigma_y}{\delta p}\right|_{p^i_{n+1}} = K\alpha_p(p^i_{n+1} + \beta_p)^{(\alpha_p - 1)} \tag{3.20}$$

5. Plastic strain:
   The plastic strain can now be calculated:
$$\epsilon^{p^i+1}_{n+1} = \epsilon^{p^i}_{n+1} + \delta\epsilon^{p^i+1}_{n+1} = \epsilon^{p^i}_{n+1} + \dot{\lambda}^{i+1}a^i \tag{3.21}$$

6. Effective stress:
   The effective stress is calculated as follows:
$$\tilde{\sigma}^{i+1} = \tilde{\sigma}^i + \delta\tilde{\sigma}^{i+1} = \tilde{\sigma}^i - \dot{\lambda}^{i+1} C : a^i \tag{3.22}$$

7. Accumulated plastic strain:
   The accumulated plastic strain is calculated:
$$p^{i+1}_{n+1} = p^i_{n+1} + \dot{\lambda}^{i+1} \tag{3.23}$$

8. Plastic flow:
   Using the effective stress calculated in Step 6, the plastic flow is:
$$a^{i+1} = \left.\frac{\delta F_p}{\delta \tilde{\sigma}}\right|_{\tilde{\sigma}^{i+1}, p^{i+1}_{n+1}} = \frac{1}{f_p(\tilde{\sigma}^{i+1})} \begin{Bmatrix} 0 \\ c^2\tilde{\sigma}^{i+1}_{22} \\ c^2\tilde{\sigma}^{i+1}_{33} \\ \tilde{\sigma}^{i+1}_{12} \\ \tilde{\sigma}^{i+1}_{13} \\ \tilde{\sigma}^{i+1}_{23} \end{Bmatrix} \tag{3.24}$$

9. Yield condition:
   The final step of the CPA algorithm is to check if values of the yield function is consistent with the tolerance requirements when using the values calculated in the last iteration:
$$F_p^{i+1} = F_p(\tilde{\sigma}^{i+1}, p^{i+1}_{n+1}) = f_p(\tilde{\sigma}^{i+1}) - \sigma_y(p^{i+1}_{n+1}) \tag{3.25}$$
   If $|F_p^{i+1}| \leq TOL$ then the solution is found and the values calculated in the last iteration can be saved as correct values, otherwise if $|F_p^{i+1}| > TOL$ the solution is not correct, so i is set to $i + 1$ and the process starts again from Step 4.

If the maximum number of iteration is reached without convergence to the correct solution ABAQUS will abandon the current time increment and reattempt with a smaller one.

3.1.6 Diffuse damage

There are three elements necessary to define a multidimensional damage model:

- One or more scalar variables known as damage variables that describe the internal state of the material. Each of these variables represents a particular type of damage.
- Thermodynamic forces associated to each of the damage variables. This can be done using the Helmholtz or Gibbs free energy density
- Damage evolution laws that describe how the damage develops. This can be done with kinetic equations developed from thermodynamic principles or functions developed from experimental results and material characteristics.

In the UMAT diffuse damage model [16] two damage variables are defined, d_{22} and d_{12}, that are respectively associated with transverse matrix micro-cracking (Section 2.2.2) and fiber-matrix debonding (Section 2.2.3).

In the UMAT subroutine three different diffuse damage models are set out: the Ladeveze model [23], a modified version of the Wang model [24] and a custom model. In particular, the Wang model is modified with the aim of making it work with only two diffuse damage variables and taking into account the crack closure. The custom model uses the same damage variables and damage evolution laws of the Ladeveze model but expands the definition of the Helmholtz free energy density to include terms related to a three dimensional case.

Ladeveze model

P. Ladeveze and E. Le Dantec model from 1992 uses the following definition of the Helmholtz free energy density [23]:

$$\Psi = \frac{1}{2\rho}\left[\frac{\sigma_{11}^2}{E_1} + \frac{\langle\sigma_{22}\rangle_+^2}{E_2(1-d')} + \frac{\langle\sigma_{22}\rangle_-^2}{E_2} - 2\frac{\nu_{12}\sigma_{11}\sigma_{22}}{E_1} + \frac{\sigma_{12}^2}{G_{12}(1-d)}\right] \tag{3.26}$$

where $\langle x\rangle$ are the Macaulay brackets:

$$\langle x\rangle_+ = \begin{cases} 0 & x < 0 \\ x & x \geq 0 \end{cases} \tag{3.27}$$

$$\langle x\rangle_+ = \begin{cases} x & x < 0 \\ 0 & x \geq 0 \end{cases} \tag{3.28}$$

This operator is used to take into consideration crack closure in compression. d and d' are the scalar damage variables.
The associated thermodynamic forces Y_d and $Y_{d'}$ control damage development the same way that energy release rate govern crack propagation:

$$Y_d = -\rho\frac{\delta\Psi}{\delta d} = \frac{\sigma_{12}^2}{2G_{12}(1-d)^2} \tag{3.29}$$

$$Y_d = -\rho\frac{\delta\Psi}{\delta d'} = \frac{\langle\sigma_{22}\rangle_+^2}{2E_{12}(1-d')^2} \tag{3.30}$$

Modified Wang model

The definition of the Helmholtz free energy density used in the modified Wang model is:

$$\Psi = \frac{1}{2\rho}\left[\frac{\sigma_{11}^2}{E_1} + \frac{\sigma_{22}^2}{E_2(1-d_{22})} + \frac{\sigma_{33}^2}{E_3} - 2\frac{\nu_{12}\sigma_{11}\sigma_{22}}{E_1}\right. \tag{3.31}$$

$$\left. -2\frac{\nu_{13}\sigma_{11}\sigma_{33}}{E_1} - 2\frac{\nu_{23}\sigma_{22}\sigma_{33}}{E_2} + \frac{\sigma_{12}^2}{G_{12}(1-d_{12})} + \frac{\sigma_{13}^2}{G_{13}} + \frac{\sigma_{23}^2}{G_{23}}\right] \tag{3.32}$$

Custom model

The definition of the Helmholtz free energy density used in the custom model is:

$$\Psi = \frac{1}{2\rho}\left[\frac{\sigma_{11}^2}{E_1} + \frac{\langle\sigma_{22}\rangle_+^2}{E_2(1-d_{22})} + \frac{\langle\sigma_{22}\rangle_-^2}{E_2} + \frac{\langle\sigma_{33}\rangle_+^2}{E_3(1-d_{22})}\right. \tag{3.33}$$

$$+\frac{\langle\sigma_{33}\rangle_-^2}{E_3} - 2\frac{\nu_{12}\sigma_{11}\sigma_{22}}{E_1} - 2\frac{\nu_{13}\sigma_{11}\sigma_{33}}{E_1} - 2\frac{\nu_{23}\sigma_{22}\sigma_{33}}{E_2} \tag{3.34}$$

$$\left.+\frac{\sigma_{12}^2}{G_{12}(1-d_{12})} + \frac{\sigma_{13}^2}{G_{13}(1-d_{12})} + \frac{\sigma_{23}^2}{G_{23}(1-d_{12})}\right] \tag{3.35}$$

Damage evolution laws

The following damage evolution laws are used to control changes in the diffuse damage variables:

$$d_{22} = \begin{cases} a_d Y_{d_{22}} & Y_{d_{22}} \leq Y_{d_{22}} < Y_{d_{22}} \\ 0 & \text{otherwhise} \end{cases} \tag{3.36}$$

$$d_{12} = \begin{cases} b_d Y_{d_{22}} + c_d & Y_{d_{12}}^0 \leq Y_{d_{22}} < Y_{d_{22}}^c \\ d_d Y_{d_{12}}^{e_d} + f_d & Y_{d_{12}}^{trans} \leq Y_{d_{12}} < Y_{d_{12}}^c \\ 0 & \text{otherwhise} \end{cases} \tag{3.37}$$

where a_d, b_d, c_d, d_d, e_d, f_d, $Y_{d_{22}}^0$, $Y_{d_{12}}^0$ and $Y_{d_{12}}^{trans}$ come directly from experimental data and $Y_{d_{22}}^c$ and $Y_{d_{12}}^c$ can be calculated as the values of the thermodynamics forces when failure strain is reached. Finally, $Y_{d_{22}}$ and $Y_{d_{12}}$ are calculated following the Ladeveze model:

$$Y_{d_{22}}(t) = sup_{\tau\leq t}\left(\sqrt{Y_{d_{22}}(\tau)}\right) \tag{3.38}$$

$$Y_{d_{12}}(t) = sup_{\tau\leq t}\left(\sqrt{Y_{d_{12}}(\tau) + bY_{d_{22}}(\tau)}\right) \tag{3.39}$$

where b is a material characteristic [23].

3.1.7 Failure criterion

The failure criterion implemented in the UMAT material model is the interactive Catalanotti failure criterion [18] with the addition of a further failure index. This criterion identifies diverse failure modes associated to either fiber or matrix failure under tension or compression, it also includes in-situ effects in its formulation:

- Matrix tensile failure: the following index is proposed

$$\phi_{mT} = \begin{cases} 0 & \sigma_n < 0 \\ \left(\frac{\sigma_n}{S_T^{is}}\right)^2 + \left(\frac{\tau_L}{S_L^{is}}\right)^2 + \left(\frac{\tau_T}{S_T^{is}}\right)^2 + \lambda\left(\frac{\sigma_n}{S_T^{is}}\right)\left(\frac{\tau_L}{S_L^{is}}\right)^2 + \kappa\left(\frac{\sigma_n}{S_T^{is}}\right) & \sigma_n \geq 0 \end{cases} \tag{3.40}$$

  where:

$$\kappa = \frac{(S_T^{is})^2 - (Y_T^{is})^2}{S_T^{is} Y_T^{is}} \qquad \lambda = 2\eta_L \frac{S_T^{is}}{S_L^{is}} - \kappa \tag{3.41}$$

  It is important to note that in some cases the parameter κ can be negative leading to loading cases with a negative failure index. This inaccurate result can be due to the effect of in-situ strengths, the problem is not addressed in the original publication.

  The stress components on the fracture plane are calculated as follows:

$$\sigma_n = \frac{\tilde{\sigma}_{22} + \tilde{\sigma}_{33}}{2} + \frac{\tilde{\sigma}_{22} - \tilde{\sigma}_{33}}{2} cos(2\alpha) + \tilde{\sigma}_{23} sin(2\alpha) \tag{3.42}$$

$$\tau_L = -\frac{\tilde{\sigma}_{22} - \tilde{\sigma}_{33}}{2} sin(2\alpha) + \tilde{\sigma}_{23} cos(2\alpha) \tag{3.43}$$

$$\tau_T = \tilde{\sigma}_{12} cos(\alpha) + \tilde{\sigma}_{13} sin(\alpha) \tag{3.44}$$

  where α is the fracture plane angle. This angle is found calculating the failure index for all possible angles between 0° and 90°, the angle for which the maximum failure index is obtained is considered the correct one.

- Compressive matrix failure: a modified version of the A. Puck and H. Shurmann [19] defined as follows:

$$\Phi_{mC} = \begin{cases} \left(\frac{\tau_T}{S_T^{is} - \eta_T \sigma_n}\right)^2 + \left(\frac{\tau_L}{S_L^{is} - \eta_L \sigma_n}\right) & \sigma_n < 0 \\ 0 & \sigma_n \geq 0 \end{cases} \tag{3.45}$$

  The stresses on the fracture plane are calculated as shown for the tensile matrix failure

- Tensile fiber failure: a non interacting maximum strain criterion is used [18]:

$$\Phi_{fT} = \begin{cases} 0 & \epsilon_{11} < 0 \\ \frac{\epsilon_{11}}{\epsilon_{11}^{fT}} & \epsilon_{11} \geq 0 \end{cases} \tag{3.46}$$

  where ϵ_{11}^{fT} is the tensile failure strain in the fiber direction.

- Compressive fiber failure: A non-interacting maximum strain criterion is used:

$$\Phi_{fC} = \begin{cases} \frac{\epsilon_{11}}{\epsilon_{11}^{fC}} & \epsilon_{11} < 0 \\ 0 & \epsilon_{11} \geq 0 \end{cases} \tag{3.47}$$

  where ϵ_{11}^{fC} is the compressive failure strain in fiber direction.

Fiber kinking is also considered because it is usually recognized as the most common to occur when the component is under longitudinal compression. The creation of kink bands is due to the rotation of initially misaligned fibers. This phenomena induces shearing in the matrix. Catalanotti et al. [18] proposes two failure indexes associated with fiber kinking:

$$\Phi_{fkT} = \begin{cases} 0 & \sigma_n^{(m)} < 0 \\ \left(\frac{\sigma_n^{(m)}}{S_T^{is}}\right)^2 + \left(\frac{\tau_L^{(m)}}{S_L^{is}}\right)^2 + \left(\frac{\tau_T^{(m)}}{S_T^{is}}\right)^2 + \lambda\left(\frac{\sigma_n^{(m)}}{S_T^{is}}\right)\left(\frac{\tau_L^{(m)}}{S_L^{is}}\right)^2 + \kappa\left(\frac{\sigma_n^{(m)}}{S_T^{is}}\right)^2 & \sigma_n^{(m)} \geq 0 \end{cases} \tag{3.48}$$

$$\Phi_{fkC} = \begin{cases} \left(\frac{\tau_T^{(m)}}{S_T^{is} - \eta_T \sigma_n^{(m)}}\right)^2 + \left(\frac{\tau_L^{(m)}}{S_L^{is} - \eta_L \sigma_n^{(m)}}\right) & \sigma_n^{(m)} < 0 \\ 0 & \sigma_n^{(m)} \geq 0 \end{cases} \tag{3.49}$$

Whether the resulting fracture plane is under tension or compression is what determines which failure index needs to be used. The normal and shear stresses on the fracture plane can be calculated as follows.

$$\sigma_n^{(m)} = \sigma_{22}^{\tilde{\alpha}} = \frac{\tilde{\sigma}_{22}^{\varphi} + \tilde{\sigma}_{33}^{\theta}}{2} sin(2\alpha) + \frac{\tilde{\sigma}_{22}^{\varphi} - \tilde{\sigma}_{33}^{\theta}}{2} cos(2\alpha) + \tilde{\sigma}_{23}^{\varphi} sin(2\alpha) \tag{3.50}$$

$$\tau_T^m = \tilde{\sigma}_{23}^{\alpha} = -\frac{\tilde{\sigma}_{22}^{\varphi} - \tilde{\sigma}_{33}^{\theta}}{2} sin(2\alpha) + \tilde{\sigma}_{23}^{\varphi} cos(2\alpha) \tag{3.51}$$

$$\tau_L^m = \tilde{\sigma}_{12}^{\varphi} cos(\alpha) + \tilde{\sigma}_{13}^{\varphi} sin(\alpha) \tag{3.52}$$

where:

- $\tilde{\sigma}_{22}^{\alpha}$,$\tilde{\sigma}_{23}^{\alpha}$ and $\tilde{\sigma}_{12}^{\alpha}$ are the effective stress components on the third of the three coordinates systems associated with fiber kinking,
- $\tilde{\sigma}_{22}^{\varphi}$,$\tilde{\sigma}_{12}^{\varphi}$,$\tilde{\sigma}_{13}^{\varphi}$ are the effective stress components on the second of the three coordinates systems associated with fiber kinking
- $\tilde{\sigma}_{33}^{\theta}$ an effective stress component in the first of the three coordinates systems associated with fiber kinking.

In order to obtain the effective stress tensors in these coordinates systems it is necessary to perform the following coordinate transformations:

$$\tilde{\sigma}^{(\theta)} = R_{()\rightarrow(\theta)} \rightarrow \tilde{\sigma} R_{()\rightarrow(\theta)}^T \tag{3.53}$$

$$\tilde{\sigma}^{(\varphi)} = R_{(\theta)\rightarrow(\varphi)} \rightarrow \tilde{\sigma} R_{(\theta)\rightarrow(\varphi)}^T \tag{3.54}$$

$$\tilde{\sigma}^{(\alpha)} = R_{(\varphi)\rightarrow(\alpha)} \rightarrow \tilde{\sigma} R_{(\varphi)\rightarrow(\alpha)}^T \tag{3.55}$$

where:

$$R_{()\rightarrow(\theta)} = \begin{bmatrix} 1 & 0 & 0 \\ 0 & cos(\theta) & sin(\theta) \\ 0 & -sin(\theta) & cos(\theta) \end{bmatrix} \tag{3.56}$$

$$R_{(\theta)\rightarrow(\varphi)} = \begin{bmatrix} cos(\varphi) & sin(\varphi) & 0 \\ -sin(\varphi) & cos(\varphi) & 0 \\ 0 & 0 & 1 \end{bmatrix} \tag{3.57}$$

$$R_{(\theta)\rightarrow(\varphi)} = \begin{bmatrix} 1 & 0 & 0 \\ 0 & cos(\alpha) & sin(\alpha) \\ 0 & -sin(\alpha) & cos(\alpha) \end{bmatrix} \tag{3.58}$$

The angles θ and φ can be calculated as follows:

$$\theta = \frac{1}{2} arctan\left(\frac{2\tilde{\sigma}_{23}}{\tilde{\sigma}_{22} - \tilde{\sigma}_{33}}\right) \tag{3.59}$$

$$\varphi = \begin{cases} -\gamma_m & \tilde{\sigma}_{12} < 0 \\ \gamma_m & \tilde{\sigma}_{12} \geq 0 \end{cases} \tag{3.60}$$

where γ_m is calculated numerically using the Newton-Raphson method. The converge condition consists in a simple comparison between the relative error of the value γ_m in successive iterations and a maximum tolerance value.
Lastly the angle α can be obtained as it is done for the fracture angle in the tensile and compressive failure cases: both Φ_{fkt} and Φ_{fkc} are calculated for all possible values of α between 0° and 90°. The angle with which the maximum index is obtained is considered the correct α value.

3.1.8 Failure damage

The failure damage model used in the UMAT subroutine is the Linde model [25]. Since this model uses two damage variables, one for the fiber failure and one for the matrix failure, it is necessary to introduce some adaptations in order to use it with the Catalanotti failure criterion [18] described in section 3.1.7. The following failure model is the result of the previously announced modifications:

- Matrix failure damage: The value of the matrix failure damage variable is calculated for each failure index:

$$d_m^T = 1 - \frac{1}{\Phi_{mt}} exp\left(\frac{(1-\Phi_{mt})C_{22}L_c(\epsilon_{eq}^{fT(\alpha)})^2}{G_{mc}^T}\right) \tag{3.61}$$

$$d_m^C = 1 - \frac{1}{\Phi_{mC}} exp\left(\frac{(1-\Phi_{mc})C_{22}L_c(\epsilon_{eq}^{fC(\alpha)})^2}{G_{mc}^C}\right) \tag{3.62}$$

where G_{mc}^T and G_{mc}^C are the interlaminar fracture toughness of the matrix respectively under tension and compression. In the case of longitudinal $(\tilde{\sigma}_{11})$compression it is necessary to take into account fiber kinking:

$$d_{fkT}^f = 1 - \frac{1}{\Phi_{fkt}} exp\left(\frac{(1-\Phi_{fkt})C_{22}L_C(\epsilon_{eq}^{fKT(\alpha)})^2}{G_{mc}^T}\right) \tag{3.63}$$

$$d_{fkC}^f = 1 - \frac{1}{\Phi_{fkc}} exp\left(\frac{(1-\Phi_{fkc})C_{22}L_C(\epsilon_{eq}^{fKC(\alpha)})^2}{G_{mc}^C}\right) \tag{3.64}$$

The UMAT subroutine calculates an equivalent failure strain on the fracture plane in order to perform these calculations. The equivalent failure strain is saved for each failure mode when the corresponding failure index reaches the unit value. The equivalent failure strain is calculated as follows:

$$\epsilon_{eq}^{f(\alpha)} = \sqrt{(\epsilon_n^f)^2 + (\gamma_T^f)^2 + (\gamma_L^f)^2} = \sqrt{(\epsilon_{22}^{f(\alpha)})^2 + (2\epsilon_{23}^{f(\alpha)})^2 + (2\epsilon_{12}^{f(\alpha)})^2} \tag{3.65}$$

The value of the matrix failure damage is obtained as:

$$d_m^{f'} = \begin{cases} \max(d_{mt}^f, d_{fkt}^f) + d_{mc}^f & \epsilon_{22}^e \geq 0 \quad \tilde{\sigma}_{11} < 0 \quad \max(d_{mt}^f, d_{fkt}^f) + d_{mc}^f < 1 \\ \max(d_{mc}^f, d_{fkc}^f) & \epsilon_{22}^e < 0 \quad \tilde{\sigma}_{11} < 0 \quad \max(d_{mc}^f, d_{fkc}^f) < 1 \\ d_{mt}^f + d_{mc}^f & \epsilon_{22}^e \geq 0 \quad \tilde{\sigma}_{11} \geq 0 \quad d_{mt}^f + d_{mc}^f < 1 \\ d_{mc}^f & \epsilon_{22}^e < 0 \quad \tilde{\sigma}_{11} \geq 0 \quad d_{mc}^f < 1 \\ 1 & \text{otherwise} \end{cases} \tag{3.66}$$

$$d_m^f = sup_{\tau \leq t}(d_m^{f'}) \tag{3.67}$$

- Fiber failure damage: As mentioned in section 3.1.7 the failure criterion uses two different indices for fiber failure. The value of the failure damage is calculated for both indices and then the maximum is considered the correct value:

$$d_{ft} = 1 - \frac{1}{\Phi_{ft}} exp\left(\frac{(1-\Phi_{ft})C_{11}L_c(\epsilon_{11}^{fT})^2}{G_{fc}^T}\right) \tag{3.68}$$

$$d_{fc} = 1 - \frac{1}{\Phi_{fc}} exp\left(\frac{(1-\Phi_{fc})C_{11}L_c(\epsilon_{11}^{fC})^2}{G_{fc}^C}\right) \tag{3.69}$$

$$d_f^f = \begin{cases} \sup_{\tau \leq t}\left(\max(d_{ft}^f, d_{fc}^f)\right) & \max(d_{ft}^f, d_{fc}^f) < 1 \\ 1 & \max(d_{ft}^f, d_{fc}^f) \geq 1 \end{cases} \tag{3.70}$$

where G_{fc}^T and G_{fc}^C are the fracture toughness of the fiber respectively under tension and compression.

3.1.9 Jacobian matrix

The major difference between the UMAT and VUMAT subroutine is that the UMAT, used for implicit computation, calculates the Jacobian matrix in each iteration while the VUMAT, used in explicit, does not.

The Jacobian matrix is defined as:

$$J = \frac{\delta \Delta \sigma}{\delta \Delta \epsilon} = \begin{bmatrix} \frac{\delta\sigma_{11}}{\delta\epsilon_{11}} & \frac{\delta\sigma_{11}}{\delta\epsilon_{22}} & \frac{\delta\sigma_{11}}{\delta\epsilon_{33}} & 0 & 0 & 0 \\ \frac{\delta\sigma_{22}}{\delta\epsilon_{11}} & \frac{\delta\sigma_{22}}{\delta\epsilon_{22}} & \frac{\delta\sigma_{22}}{\delta\epsilon_{33}} & 0 & 0 & 0 \\ \frac{\delta\sigma_{33}}{\delta\epsilon_{11}} & \frac{\delta\sigma_{33}}{\delta\epsilon_{22}} & \frac{\delta\sigma_{33}}{\delta\epsilon_{33}} & 0 & 0 & 0 \\ \frac{\delta\sigma_{12}}{\delta\epsilon_{11}} & \frac{\delta\sigma_{12}}{\delta\epsilon_{22}} & 0 & \frac{\delta\sigma_{12}}{\delta\epsilon_{12}} & 0 & 0 \\ \frac{\delta\sigma_{13}}{\delta\epsilon_{11}} & 0 & \frac{\delta\sigma_{13}}{\delta\epsilon_{33}} & 0 & \frac{\delta\sigma_{13}}{\delta\epsilon_{13}} & 0 \\ 0 & \frac{\delta\sigma_{23}}{\delta\epsilon_{22}} & \frac{\delta\sigma_{23}}{\delta\epsilon_{33}} & 0 & 0 & \frac{\delta\sigma_{23}}{\delta\epsilon_{23}} \end{bmatrix} \tag{3.71}$$

The calculation of the Jacobian matrix is necessary because of the use of a backward Euler procedure by the Standard ABAQUS solver which requires the Newton

Raphson method to be implemented.
Each of the terms is analytically specified, an example of one is here given:

$$\begin{aligned} J_{11} = \frac{\delta\sigma_{11}}{\delta\epsilon_{11}} =& (1-d_{f1})(1-d_{d1})C_{11} - \frac{\delta d_{d1}}{\delta\epsilon_{11}}(1-d_{f1})C_{11}\epsilon_{11} \\ & - \frac{\delta d_{f1}}{\delta\epsilon_{11}}(1-d_{d1})C_{11}\epsilon_{11} - \frac{\delta d_{f1}}{\delta\epsilon_{11}}(1-d_{d2})(1-d_{f2})C_{12}\epsilon_{22} \\ & - \frac{\delta d_{f1}}{\delta\epsilon_{11}}(1-d_{d3})(1-d_{f3})C_{13}\epsilon_{33} \end{aligned} \tag{3.72}$$

3.1.10 Modus operandi

As mentioned in the previous sections, different material behaviors are modeled through the UMAT and VUMAT subroutines. To provide the user with the option to choose which one to activate, these subroutines have been separated into distinct modules within the main subroutine, which can be enabled using a flag in the Fortran code.
The following sections can be activated or deactivated in the subroutines:

- *DIF-DAM*: computes the diffuse damage of the component as explained in Section 3.1.6. The wanted diffuse damage model can be selected using a flag in the subroutine.
- *THREE-DD* It is a sub-option of *DIF-DAM* and activates the three-dimensional model instead of the classical bi-dimensional one.
- *PLASTICITY*: computes the pseudo-plasticity behavior as explained in Section 3.1.5.
- *FAIL-DAM*: calculates the failure of fibers or matrix due to the loading condition at the considered step of the analysis. The failure criterion is extensively explained in Section 3.1.7.
- *FIBRE-ROT*: Takes into account fiber reorientation towards loading direction as shown in Section 3.1.4.
- *COMPRESSION*: Computes the compression effect on material modulus. Because of fiber misalignment, indeed, stiffness in fiber's direction with compressive load can be up to 25% lower than in tensile loading.

A simple finite element model is created in ABAQUS in order to better understand the contribution of the multiple sections of the UMAT and VUMAT subroutines. The cube showed in Figure 3.7 is modelled and one single eight node linear brick element (C3D8) is used to discretize it.

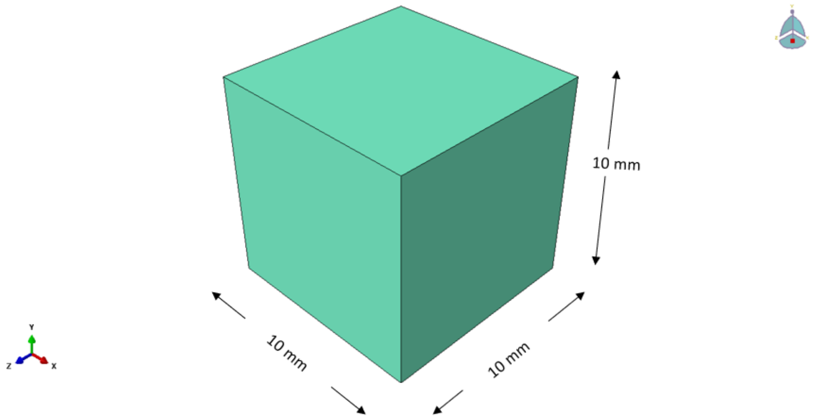

Figure 3.7: UMAT and VUMAT subroutine testing geometry

The following boundary conditions are applied to the cube surfaces as shown in Figure 3.8:

- $U_z = 0$ for both the XY surfaces
- $U_y = 0$ for both the XZ surfaces
- $U_y = 0$ for negative YZ surface
- $U_x > 0$ for traction testing and $U_x < 0$ for compression testing on the positive YZ surface

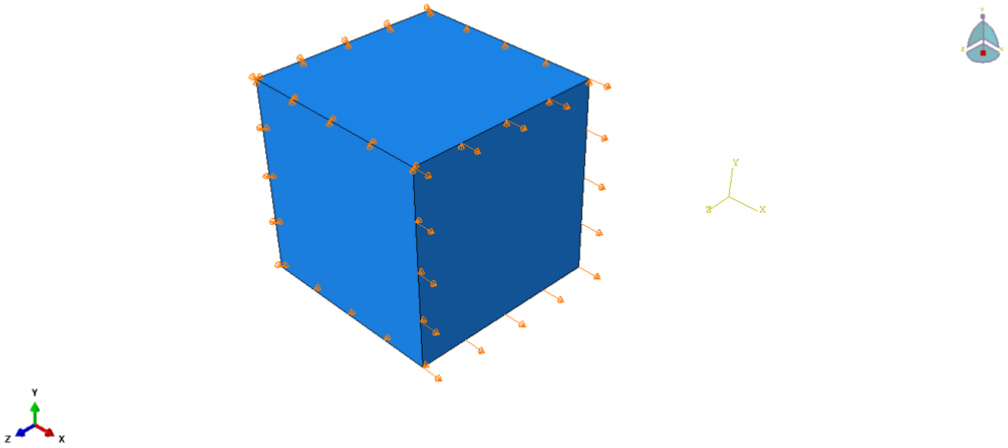

Figure 3.8: Boundary conditions applied to the testing geometry

The material used to test the subroutines is one layer of a unidirectional fiber reinforced composite material. Tests are performed with fibers at 0° and 90° from the loading direction.

To better visualize the effect of each section of the UMAT and VUMAT subroutine they are activated one by one. The results in pure tensile and pure compressive loading condition are shown below.

Pure tensile loading: [0] case

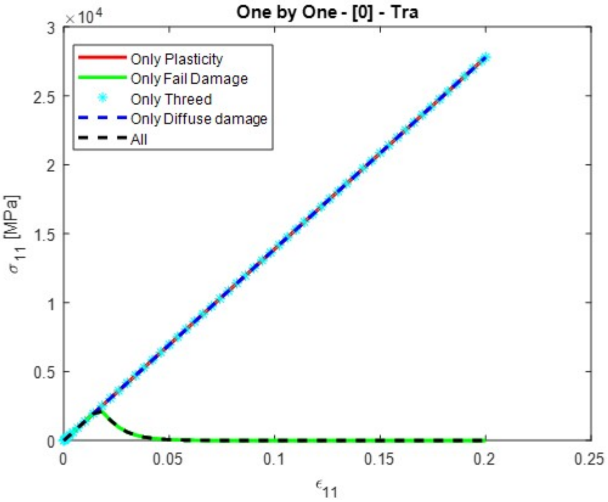

Figure 3.9: Stress-strain curve of [0] cube with tensile load

By observing Figure 3.9 one notices that the only section of the subroutine that gives a contribution with a zero degree layer of material is the *FAIL-DAM* one. Diffuse damage and pseudo-plasticity behavior are mostly due to the matrix so in this case their effect is not visible.

Pure compressive loading: [0] case

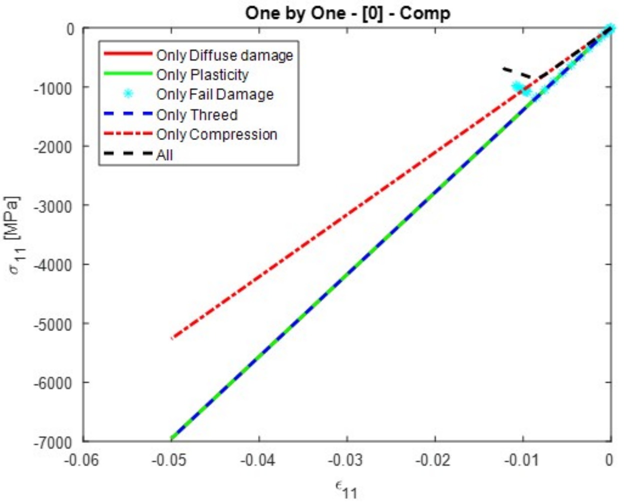

Figure 3.10: Stress-strain curve of [0] cube with compressive load

The compressive behavior of the cube is shown in Figure 3.10. In this case only *FAIL-DAM* and *COMPRESSION* give visible contribution. Specifically it is clear that compressive loading reduces conspicuously the material modulus.

Pure tensile loading: [90] **case**

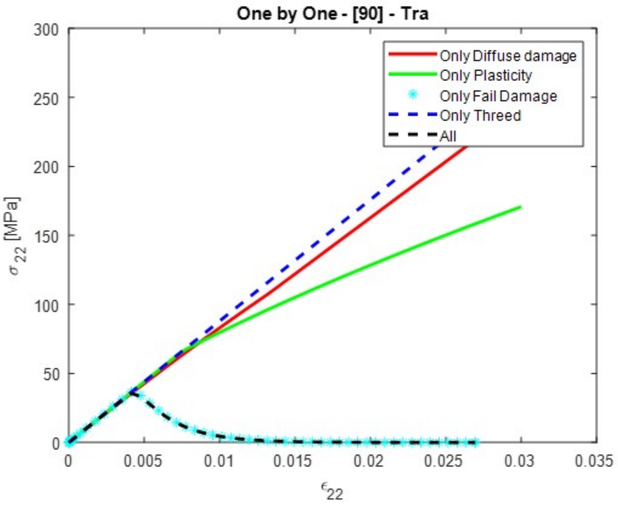

Figure 3.11: Stress-strain curve of [90] cube with tensile load

The tensile behavior of the cube with [90] layup is displayed in Figure 3.11. When the layer has a ply angle different from 0 all the sections of the subroutine have an impact on the cube behavior. It is interesting to point out that the contribution of plasticity and diffuse damage in, respectively, giving some non linearity and lowering the slope of the curve, is imperceptible even after zooming in on the first segment of the graph (Figure 3.12).

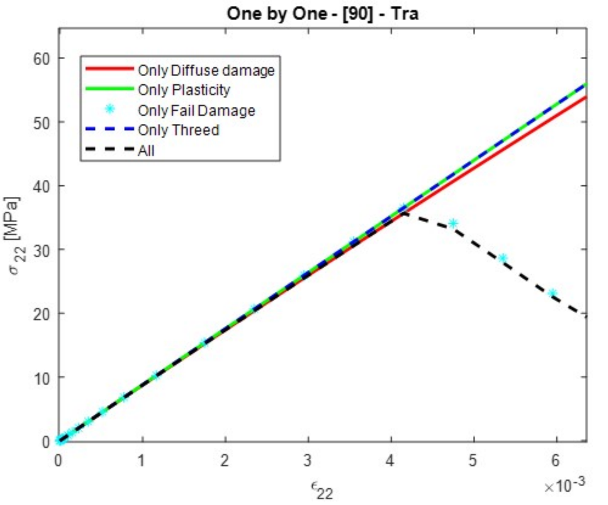

Figure 3.12: Detail of the tress-strain curve of [90] cube with tensile load

Since with the current layup it is possible to see di effect of the diffuse damage, the analysis is performed by activating all the sections and by choosing a different diffuse damage model each time. The results are shown in Figure 3.13.

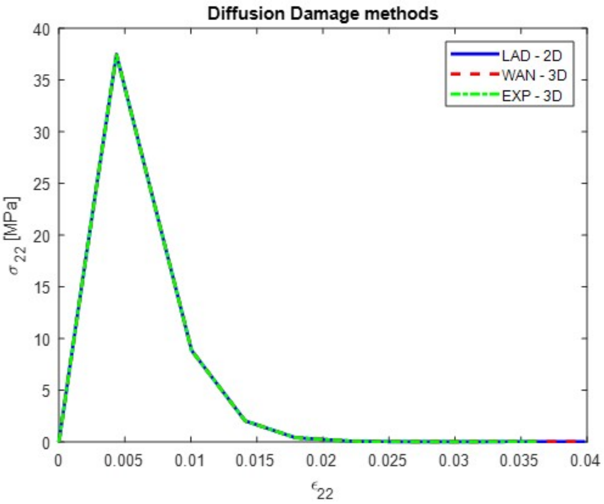

Figure 3.13: Diffuse damage models effect on the material behavior

Apparently no noticeable difference exists between the diffuse damage models. Zooming in the after failure area (Figure) it is possible to notice some minor variations 3.14.

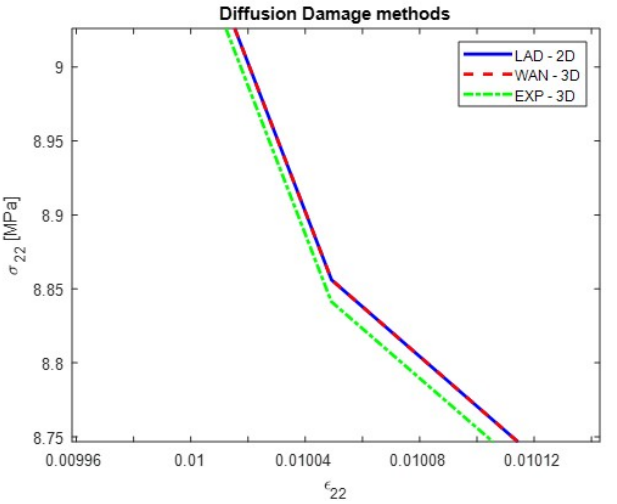

Figure 3.14: Detail of diffuse damage models effect on the material behavior

Pure compressive loading: $[90]$ **case**

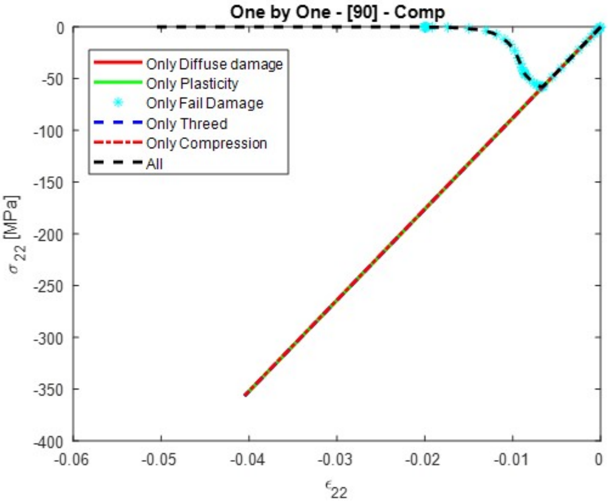

Figure 3.15: Stress-strain curve of $[90]$ cube with compressive load

Finally, compressive behavior on the $[90]$ cube is shown in Figure 3.15. Diffuse damage and plasticity have no contribution in compressive loading. Moreover, matrix properties have no changes in the slope due to compressive loading, therefore with this layup there is no contribution given by the *COMPRESSION* section. Only the *FAIL-DAM* section of the subroutine has an impact in the final behavior of the material.

3.2 Hashin model

The Hashin failure criteria is a failure theory developed by Zvi Hashin to predict failure mostly in composite materials distinguishing between fiber and matrix failure [26]. This theory is useful in finite elements analysis because:

- It has a better accuracy in failure prediction than maximum stress or strain theories because it considers differential failure in matrix and fiber which is a more accurate representation of composite behavior
- It can be used both for tensile and compressive failure
- It accounts for combined loading making it suitable also for complex loading conditions

The Hashin criteria can be applied both in two and three dimensional stress states, the idea is the same in both cases what changes is the number of considered stresses. The two dimensional theory focuses on the in-plane stresses and it's composed of the following criteria.

1. Fiber tension:

$$\left(\frac{\sigma_{11}}{X_T}\right)^2 + \left(\frac{\tau_{12}}{S_L}\right)^2 \geq 1 \tag{3.73}$$

   where:

   - σ_{11} is the longitudinal stress in fiber direction
   - X_T is the longitudinal tensile strength of the fibers
   - τ_{12} is the shear stress
   - S_L is the longitudinal shear strength

2. Fiber compression:

$$\left(\frac{\sigma_{11}}{X_c}\right)^2 \geq 1 \tag{3.74}$$

   where: X_C is the longitudinal compressive strength of the fibers.

3. Matrix tension

$$\left(\frac{\sigma_{22}}{Y_T}\right)^2 + \left(\frac{\tau_{12}}{S_L}\right)^2 \geq 1 \tag{3.75}$$

   where:

   - σ_{22} is the transverse normal stress
   - Y_T is the transverse tensile strength of the matrix

4. Matrix compression:

$$\left(\frac{\sigma_{22}}{2S_T}\right)^2 + \left[\left(\frac{Y_C}{2S_T}^2 - 1\right)\right]\left(\frac{\sigma_{22}}{Y_C}\right) + \left(\frac{\tau_{12}}{S_L}\right)^2 \geq 1 \tag{3.76}$$

   where:

   - Y_C is the transverse compressive strength of the matrix
   - S_T is the transverse shear strength

In the three dimensional case also out-of-plane stresses are considered in the criteria.

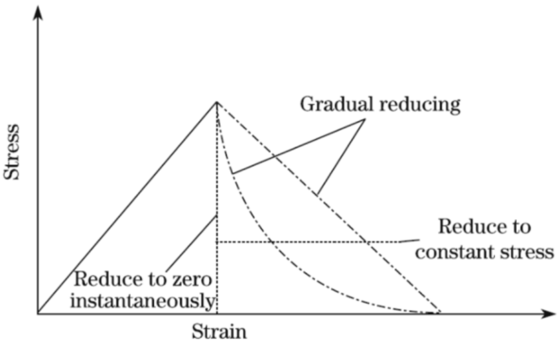

Figure 3.16: Properties reduction in composites after failure initiation [26]

In ABAQUS this criteria is used for damage initiation and when failure is identified at a specific material point properties in that point need to be modified based on a specified degradation law. There are three possibilities of property degradation laws that can be applied in combination with the Hashin failure criteria:

1. Instantaneous reduction: all the material strength is removed at the failure point.

2. Constant reduction: the stress is limited to a fixed value after failure. In this case some residual strength is preserved.

3. Gradual reduction: progressive loss. It simulates how damage propagates over time and under continued loading. Only linear progressive reduction is available as gradual reduction in ABAQUS.

This criterion is selected for running preliminary simulations of the static tests due to its lower computational time compared to the UMAT and VUMAT subroutines. It is useful for testing material properties with a model that has already been validated, before utilizing the Fortran subroutines.

3.3 Material properties

The composite used is TORAY CETEX TC1225. This composite uses T700GC carbon fibers and a PEAK matrix. The roving used has 12000 filaments, resulting in a fiber areal weight FAW of $124g/m^2$ per ply. The resin content by weight is 34%. The ply thickness is $0.184mm$. The initial properties used to model this materials are listed in table 3.2.

Property	**Value**	**Unit**	**Origin**
E_1	140000	Mpa	Experimental data
E_2	8860	MPa	Experimental data
E_3	8860	MPa	Experimental data
G_{12}	4300	MPa	Experimental data
G_{13}	7340	MPa	Experimental data
G_{23}	3700	MPa	Experimental data
ν_{12}	0.396		Experimental data
ν_{13}	0.396		Assumed from experimental data
ν_{23}	0.45		Assumed from experimental data
ϵ_{11}^{fT}	0.01684		Experimental data
ϵ_{22}^{fT}	0.00673		Experimental data
ϵ_{33}^{fT}	0.00673		Assumed from experimental data
$\|\epsilon_{11}^{fC}\|$	0.00836		[16]
$\|\epsilon_{22}^{fC}\|$	0.00637		[16]
$\|\epsilon_{33}^{fC}\|$	0.00637		[16]
γ_{12}^{f}	0.345		Experimental data
γ_{13}^{f}	0.195		[16]
γ_{23}^{f}	0.195		[16]
X_T	2400	MPa	Experimental data
X_C	950	MPa	[16]
Y_T	57	MPa	Experimental data
Y_C	205	MPa	[16]
S_L	130	MPa	Experimental data
S_T	72	MPa	[16]
α_0	53	deg	[27]
β	$4.72 * 10^{-8}$		[16]
G_{fC}^{T}	218	N/mm	[16]
G_{fC}^{C}	104	N/mm	[16]
$G_{mC}^{T} = G_{Ic}$	1.156	N/mm	[16]
$G_{mC}^{C} = G_{IIc}$	1.98	N/mm	[16]
η	0.0025		Assumed
In situ configuration	Thin ply		Assumed
t	0.184	mm	Airbus Atlantic
η_T	0.287		[18]
η_L	0.515		[18]
Θ_0		deg	Test dependent
$\chi = \frac{E_1^C}{E_1}$	0.75		Assumed
Diffuse damage model			Test dependent

Table 3.2: Material properties

Chapter 4

Static validation: compact tensile test (CT)

Fiber breaking can take place during longitudinal tension or compression. Experimental determination of the fracture toughness associated with both these fiber failure modes is fundamental for both material characterization and numerical modeling.

Currently there are no standards to determine these properties on composite materials. Compact tensile (CT) and compact compressive (CC) tests are selected for this purpose following the example of many precedents in literature [28].

This type of test is inspired by the same tests for polymers described by the ASTM-D5045 standard [29] but the coupons are designed for the specific requirements of the composite material utilized during the present study. The material properties are listed in Section 3.3.

4.1 Initial sample geometry

The coupons used for the compact tensile tests are reminiscent of those proposed by the ASTM-D5045 standard. However, the ones used for the tests here described are lightly different and have their own dimensions presented in Figure 4.1.

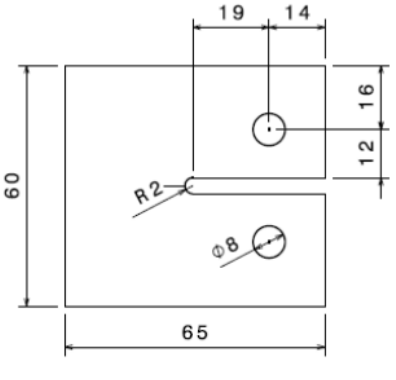

Figure 4.1: CT Test coupon geometry

The dimensions chosen for these coupons are the same used in precedent tests at ISAE-Supaero on Carbon-Epoxy coupons. For this reason there is no certainty about the correctness of this geometry in the case of the material here studied. Only after the first tests it is possible to determine if this geometry is suitable for the purpose.

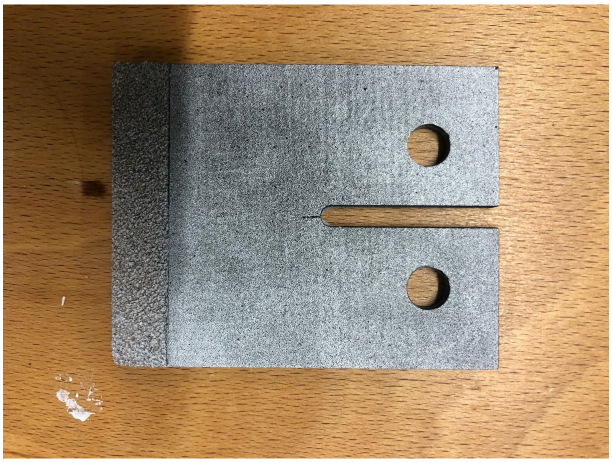

Figure 4.2: CT Test real coupon

As further explained in the ASTM-D5045 standard it is necessary to create a pre-crack in the coupon geometry, this can be observed clearly in Figure 4.2. The pre-crack is made using a diamond wire cutting machine and has a length of $5mm$.

The material used is the one presented in Section 3.3 with the following stacking sequence: $[0 \quad 90]_{5s}$

4.2 FEM model: UMAT and Hashin

The coupon is modeled using ABAQUS/CAE. Specifically, two different models are created:

- Hashin damage model: uses the ABAQUS routine with the same name for the material behavior
- UMAT model: uses the UMAT subroutine (Chapter 3) for the material behavior.

Differences between the two models are explained in the following sections.

4.2.1 Geometry

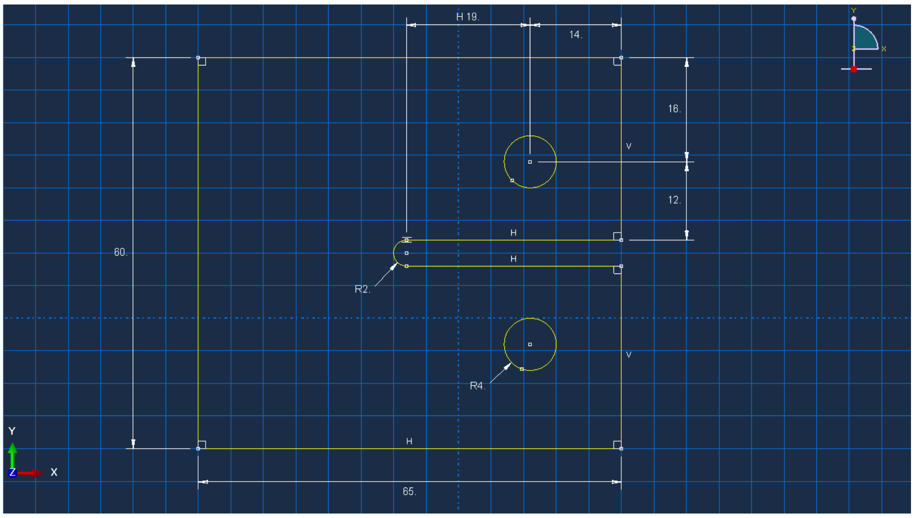

Figure 4.3: 2D Sketch of the CT coupon

The 3D volume representing the CT coupon is created starting from the sketch showed in Figure 4.3 and then extruded in order to obtain the wanted thickness of 3.7 mm. The pre-crack is created through an extruded cut of the volume.

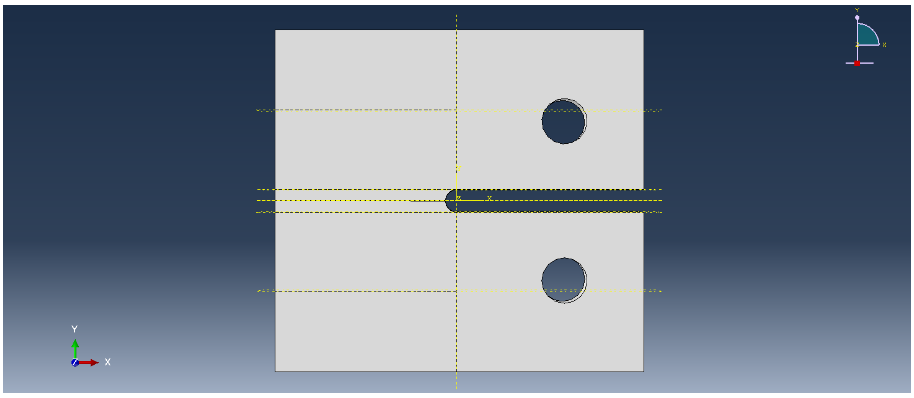

Figure 4.4: Cells partitions

In order to facilitate the meshing phase the partitions in the volume showed in Figure 4.4 are created. Because of the operating method of the UMAT subroutine, it is necessary to apply an additional partition to the dedicated model: in the thickness direction one cell corresponding per composite layer needs to be created (Figure 4.5).

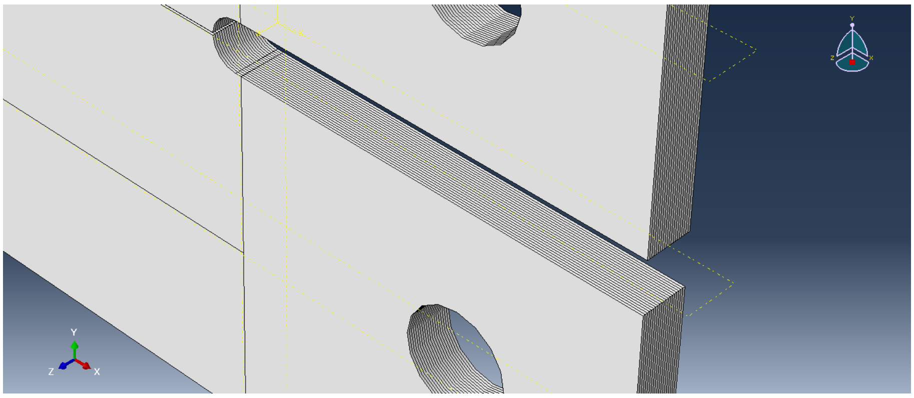

Figure 4.5: Thickness partition detail in the UMAT model

The cylinders representing the loading pins are modeled using a simple rigid shell with a radius slightly lower than the coupon holes one to avoid interpenetration. In the centers of these cylinders a reference point is created in order to measure reaction forces and displacements. The final assembly is showed in Figure 4.6.

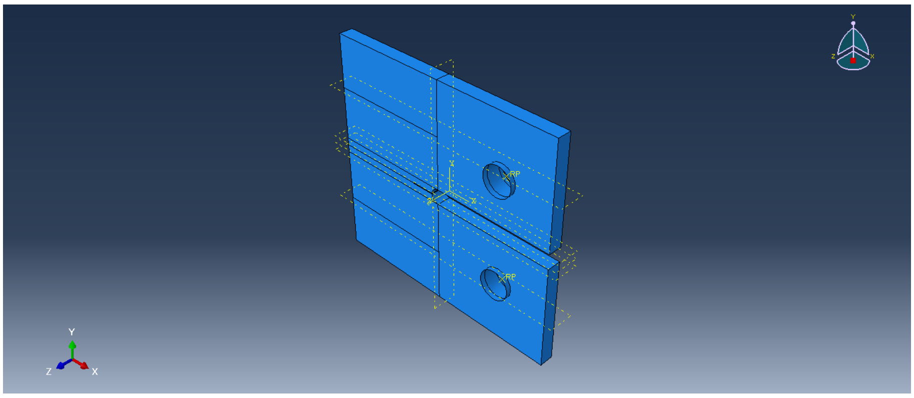

Figure 4.6: CT model's final assembly

4.2.2 Mesh

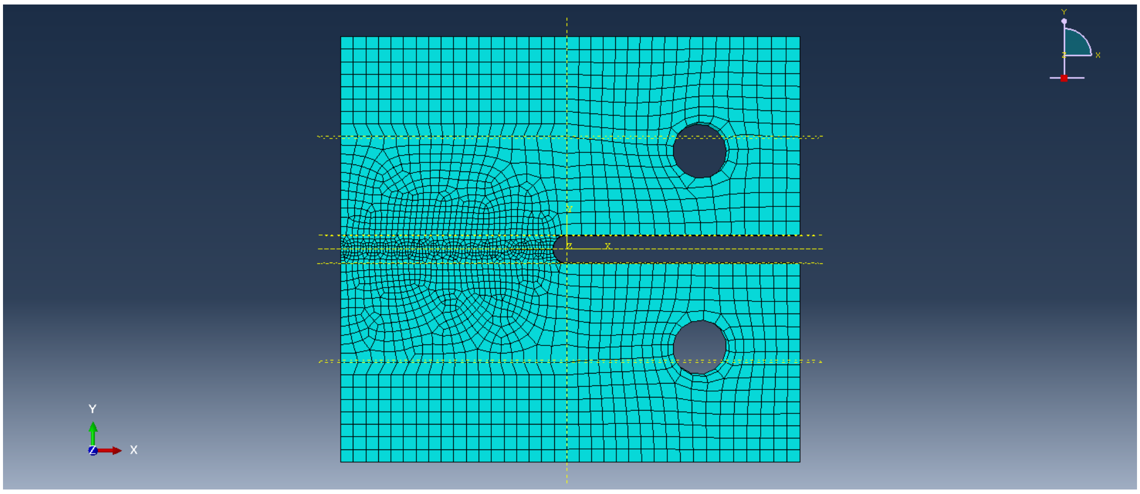

Figure 4.7: Mesh morphology of the CT coupon

As can be seen in Figure 4.7 different mesh dimensions are used in order to discretize the crack growth correctly without increasing excessively the computational cost. To achieve this result the characteristic mesh size is set to 1.7 mm away from the pre-crack while in the area of expected failure propagation it is refined to 0.4 mm. Different element types are used in the two models here described:

- C3D8 for the UMAT model
- SC8R for the Hashin damage model

In both cases the element deletion feature is activated.

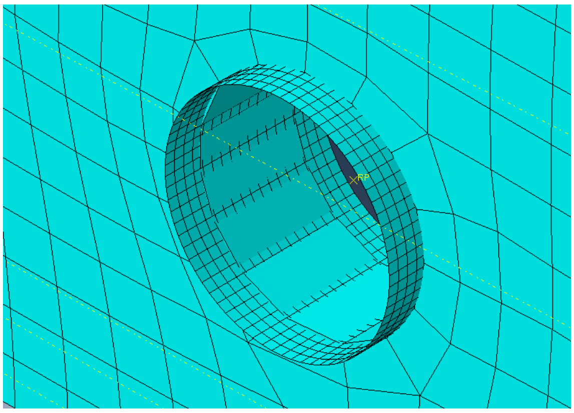

Figure 4.8: Mesh morphology of the loading cylinders

Regarding the loading cylinder mesh (Figure 4.8) discrete rigid elements with a characteristic length of 0.2 mm are used. It is crucial that the cylinder mesh is highly refined to obtain an accurate contact detection between the cylinders and the CT coupon during analysis.

4.2.3 Boundary conditions

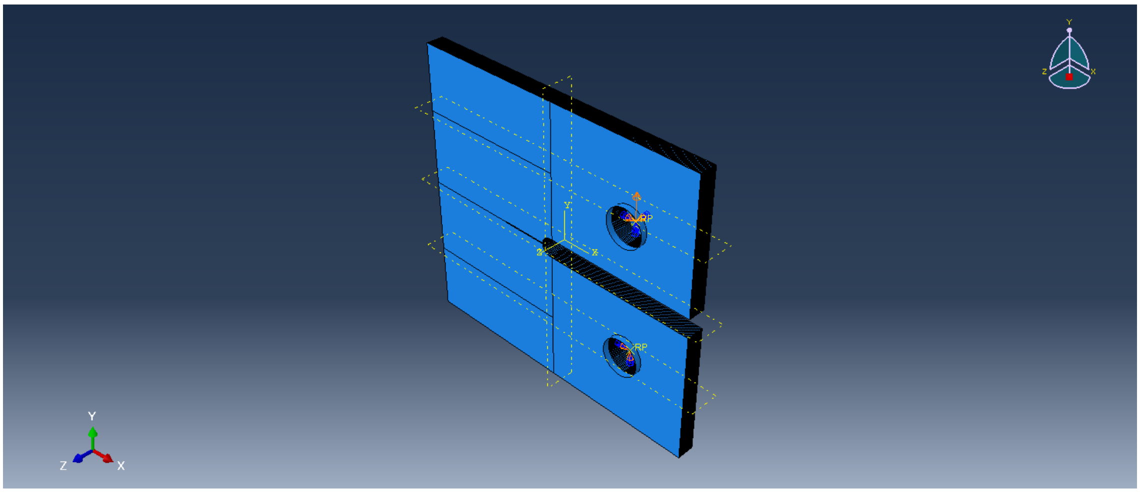

Figure 4.9: Boundary conditions

With the aim of simulating the real test loading process, the following boundary conditions are applied to both models (Figure 4.9):

- clumping conditions at the reference point defined at the center of the lower cylinder ($U_x = U_y = Uz = 0 \;\; U_{Rx} = U_{Ry} = U_{Rz} = 0$)
- $U_x = U_z = U_{Rx} = U_{Ry} = 0$ at the reference point defined at the center of the upper cylinder
- $U_y = 4 \;\; mm$ at the reference point defined at the center of the upper cylinder

Since the Hashin damage model volume is discretized using just one element in the thickness direction it is necessary to apply an additional condition in that model to obtain a plane strain condition: for this reason $U_z = 0$ is applied to the whole CT coupon part.

Finally contacts between the pins and the specimen are defined as hard contact with a friction coefficient of 0.15.

4.2.4 Analysis

The analysis carried out with the two models is an implicit one using the Newton-Raphson convergence method. The following parameters are selected:

- Minimum step: 10^{-7}
- Maximum step: 0.1
- Automatic stabilization: *Specify dissipated energy fraction* set to 0.0002
- Adaptive stabilization is used with a *Max ratio of stabilization to strain energy* is set to 0.05

4.3 CT Test

4.3.1 Experimental setup and procedure

The tests are performed using an Instron machine following the procedure of the ASTM-D5045 standard [29]. A displacement rate of $1mm/min$ is imposed to avoid dynamic effects during the experiment and two CCD cameras are placed on one side of the machine recording the crack propagation on the specimen face. Specifically, the face that is recorded gets painted in order to allow the camera to better recognize different points of the specimen separately.

During the test the following parameters are measured:

- Displacement of the machine
- Load applied to the machine
- Crack length monitored by the crack gauge (Figure 4.10) and the FRACTOMAT system
- Crack length visually measured from the images taken by the CCD cameras

- Specimen deformation through the CCD cameras.

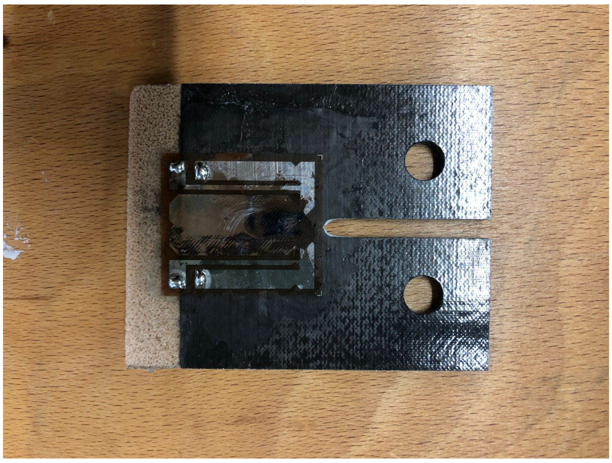

Figure 4.10: Crack gauge sensor

The procedure of the experimental campaign can be summarized in the following steps:

1. The coupon is placed in the machine. The metal pin is inserted through the hole in the upper support making it coincide with the upper hole of the specimen. The machine is then adjusted so that the hole in the lower support of the machine and the lower hole in the specimen coincide and the second pin can be inserted;
2. The machine is slightly loaded until the specimen is securely fixed. This ensures that the specimen does not rotate during the firsts loading phases of the test;
3. The cables of the crack gauge are connected to the FRACTOMAT system;
4. The test is started and the data is recorded until the load of the machine is near null and the crack has propagated almost along the whole width of the specimen.

4.3.2 Data post-processing methods

Different post processing methods can be found in literature to analyze CT tests data.

Area method

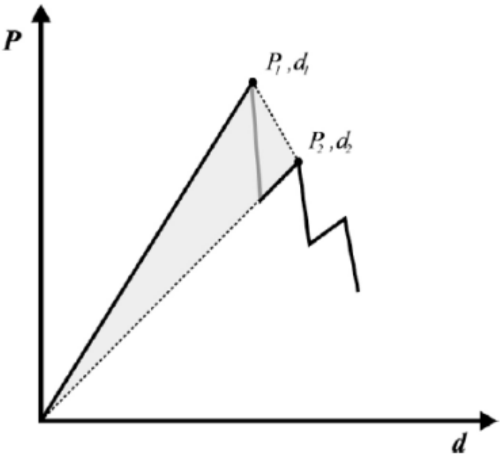

Figure 4.11: Graphic interpretation of the area method [30]

The area method is a simple approach to obtain the critical energy release rate of the material. The base concept is that the energy release rate is seen as the area below the force-displacement curve [30]. This method estimates G_c from the load and displacement of two consecutive peaks of the force displacement graphic. Moreover, the energy release rate depends on the crack length of the specimen, since the change in elastic energy is related with the surface created by crack propagation [31]:

$$G_{IC} = \frac{1}{e_p \Delta a} \frac{P_1 u_2 - P_2 u_1}{2} \tag{4.1}$$

where e_p represents the thickness of the specimen, Δa is the crack length increase between two consecutive measures, P_1 and u_1 are the load and displacement of the pins for the first measure and P_2 and u_2 of the second one.

The main drawback of this method is the high sensitivity to errors for low increments in the crack length [30].

ASTM E399

The ASTM standard E399 [32] proposes the following procedure valid for an isotropic material. The critical intensity factor for a fracture load P is given by:

$$K_{Ic} = \frac{P}{h\sqrt{w}} f\left(\frac{a}{w}\right) \tag{4.2}$$

with:

$$f\left(\frac{a}{w}\right) = \frac{2 + \frac{a}{w}}{(1 - \frac{a}{w})^{1.5}} \left[0.886 + 4.64\left(\frac{a}{w}\right) - 13.32\left(\frac{a}{w}\right)^2 + 14.72\left(\frac{a}{w}\right)^3 - 5.6\left(\frac{a}{w}\right)^4\right] \tag{4.3}$$

where h is the thickness of the specimen, w is the distance between the load line and the right hand edge of the specimen and a is the crack length whose initial value is

a_0. The critical energy release rate of the laminate can be calculated from K_{Ic} as follows:

$$G_{Ic_{lam}} = \frac{K_{Ic}^2}{\sqrt{2E_xE_y}}\sqrt{\sqrt{\frac{E_x}{E_y}} + \frac{E_x}{2G_{xy}} - \nu_{xy}} \tag{4.4}$$

where E_x, E_y, G_{xy} and ν_{xy} are respectively: the Young's modulus in fiber direction and transversal to fiber direction, shear modulus and Poisson's ratio of the laminate. These values are obtained from the laminae properties in table 3.2 using lamination theory (Section 2.4.2).

Compliance Calibration method

A different method that can be used is the compliance calibration (CC) method. This method estimates the release energy rate as a function of the compliance variation with the crack propagation according to the following equation [30]:

$$G_{Ic} = \frac{P^2}{2e_p}\frac{\delta C}{\delta a} \tag{4.5}$$

in which:

- P is the load measured at each time instant of the propagation
- e_p represents the thickness of the specimen
- a is the crack length
- C is the compliance of the specimen that can be calculated dividing the displacement (u) by the applied load (P).

The method here explained requires to obtain a function to approximate the compliance dependence on crack length. In order to do so, it is necessary to plot the experimental data of compliance against the crack variation along the test. The curve obtained is, then, fitted with a function in accordance with the results. In this case the shape of the function used is the following one, where α_3 and α_0 are constants estimated to best fit the experimental results:

$$C = f(a) = \alpha_3 a^3 + \alpha_0 \tag{4.6}$$

Introducing the expression 4.6 in equation 4.5:

$$G_{Ic} = \frac{P^2}{2ep}f'(a) = \frac{P^2}{2e_p}(3\alpha_3 a^2) \tag{4.7}$$

In order to avoid the dependence of the energy release rate on the crack length, the function $f(a)$ can be inverted obtaining the crack length as a function of the compliance:

$$G_{Ic} = \frac{P^2}{2e_p}f'(f^{-1}(C)) \tag{4.8}$$

This is called the 'Modified compliance calibration method' and its main advantage is that it eliminates the error induced by the use of the visually measured crack propagation length [31].

For the present study the crack length used in the computation of the compliance is obtained from the crack gauge. These measurements are considered to be more accurate than the ones visually determined, consequently the compliance calibration method is considered accurate enough and the modified compliance calibration method is not used.

4.4 Test 1: Results

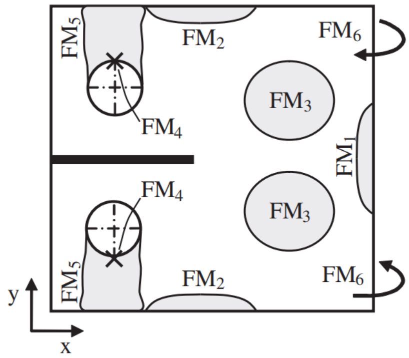

Figure 4.12: Scheme of the CT specimen with the location of the considered failure mechanisms [33]

The failure mechanisms that can appear during a CT test, besides crack propagation, are outlined in Figure 4.12[33]:

- FM_1: fiber fracture due to longitudinal compressive stress (σ_{yy}) at the right edge of the specimen
- FM_2: Fiber fracture due to longitudinal compressive stress (σ_{xx}) at the upper and lower edges of the specimen
- FM_3: matrix cracking due to in-plane shear stress (σ_{xy})
- FM_4: bearing in the holes of the specimen due to compressive stress
- FM_5: Shear-out in the holes of the specimen due to shear stress
- FM_6: buckling due to the high compressive stresses at the right edge

Figure 4.13: CT Coupon after test

In Figure 4.13 is shown the CT coupon after the first test. As easily noticeable the coupon has an unexpected torsion because of which the results obtained are unusable in order to validate the numerical models. The result can still be useful for some discussions and deliberations:

- The crack propagates in the expected area;
- The coupon unexpected torsion is probably due to buckling behavior in the compressive areas appointed as FM_1 in Figure 4.12. It is possible that the compressed area reaches the energy necessary for buckling behavior before the crack is able to propagate;
- The Hashin model is not able to simulate the real behavior because of the added condition on the out of plane displacements. Additionally, it is possible to see that both models simulate correctly the linear part of the curve representing the pre-damaged behavior but none of them is able to show the buckling problem.

The problem might be created by the sample and the pre-crack geometry. The geometry, as explained in Section 4.1, comes from previous similar tests carried out on ISAE-Supaero on carbon-Epoxy coupons. Since thermoset resins need less energy to make the crack propagate than thermoplastic ones, it is possible that some changes in the geometry need to be applied in order to obtain wanted results during tests.

A new geometry is proposed in order to make the crack propagate and obtain some useful test results.

4.5 Geometrical modifications

Detailed observations of the coupon stacking sequence are performed in order to understand why the coupon is showing out of plane displacements.

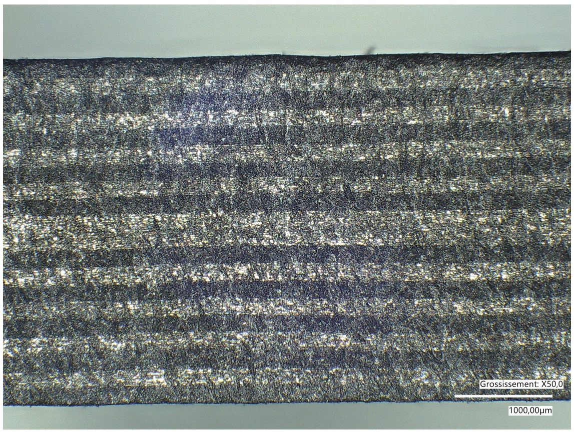

Figure 4.14: Magnification x50 of the stacking sequence of the CT sample

As observable in Figure 4.14 the stacking sequence is symmetrical, therefore out-of-plane displacements are not imputable to couplings in the material behavior. In order to read correctly the image it is necessary to point out that dark stripes are layers in which fiber direction is parallel to the image plane while the bright ones have fibers that come out of the image plane.

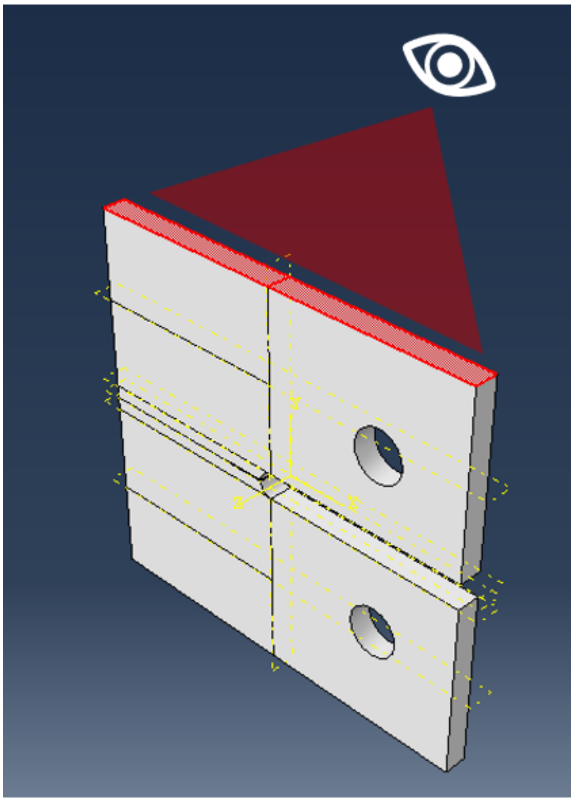

Figure 4.15: Observation direction of the microscope during the magnification

Taking into account the direction of observation during the magnification (Figure 4.15) it is clear that external layers do not have fibers in loading direction. This can result in lower buckling critical load. In order to increase the buckling critical load, the stacking sequence is rotated of 90°in the new samples.

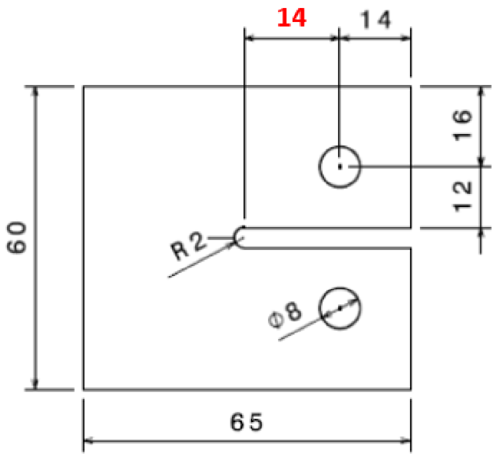

Figure 4.16: In red the modification in the CT geometry dimensions

In order to reduce the load needed to open the crack, the dimension showed in Figure 4.16 is changed from the original geometry.

4.6 Test 2: Results

First test is performed with 10 *mm* pre-crack. The coupon shows a better behavior than the original one but it broke in compression after one step of damage propagation.

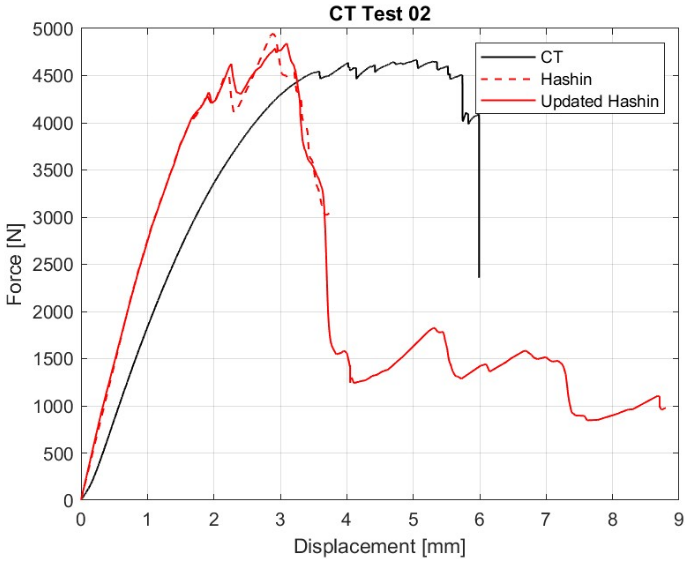

Figure 4.17: Test results with updated geometry

The observation of the after test coupon in Figures 4.18 and 4.19 leads to the conclusion that no buckling appeared during test, no out-of-plane displacement is indeed visible except for the area where fibers broke in compression. Near the pre-crack it is possible to visualize small propagation of the damage.

Figure 4.18: After test coupon top view

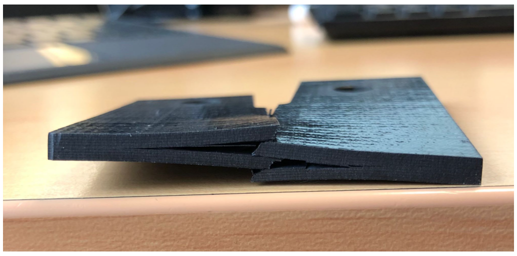

Figure 4.19: After test coupon side view

Using the procedure showed in Section 4.3.2, with a test measured crack propagation of 3 mm, it is possible to calculate the following critical energy release rate: $G_{Ic} = 185\ kJ/m^2$. Updating the FEM model with this information as showed in the graph in Figure 4.17 the model is able to detect correctly the failure force even though it remains stiffer than the real test coupon.

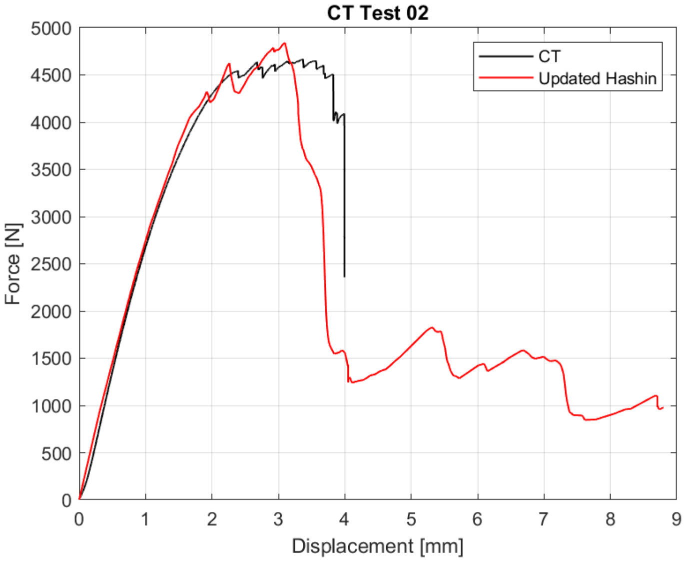

Figure 4.20: Numerical and experimental comparison with Hashin damage model

It is important to notice that the displacements measured during test are the ones of the machine and not directly the sample ones. This leads to higher displacements in the test results than the real ones. To take into account this phenomena the experimental displacements are multiplied by a constant factor of 0.25. The final comparison is showed in Figure 4.20.
After all the model's information are udated, they can be applied to the UMAT model that can be finally compared with the test results.

4.7 UMAT: Numerical and experimental results comparison

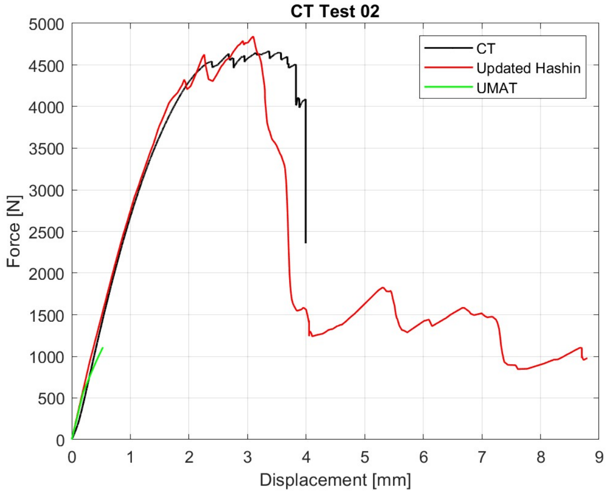

Figure 4.21: Numerical and experimental comparison with Hashin damage model and UMAT model

Figure 4.21 shows the comparison between experimental results, and numerical results calculated with both the UMAT subroutine and the Hashin model. The premature interruption of the UMAT curve stands out right away. This is due to a non convergence of the analysis. In order to localize the problem the model is run activating one by one the various subroutines (Section 3.1.10), the results are shown in Figure 4.22.

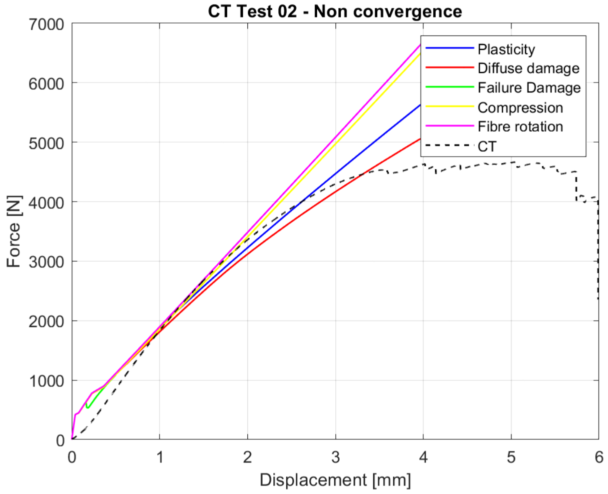

Figure 4.22: Non convergence problem identification

The problematic subroutine seems to be the *FAIL-DAM* one. The reasons behind this problem are still unclear and under study. It is still possible to observe that, as long as it converges, the UMAT graph follows correctly the test behavior.

4.8 VUMAT: Numerical and experimental results comparison

In order to overcome the convergence issue an explicit analysis is run on the FEM model using, therefore, the VUMAT subroutine instead of the UMAT. This gives the possibility to check the accuracy of the material model even if convergence issues will still need to be solved with the implicit subroutine.

The CT test is a quasi-static test that lasts for a few minutes and, consequently, cannot be simulated explicitly as it is because the number of time steps required would be too high for any calculator. The following changes are applied to the model to make the analysis less time consuming:

- Mass scaling factor of 10000

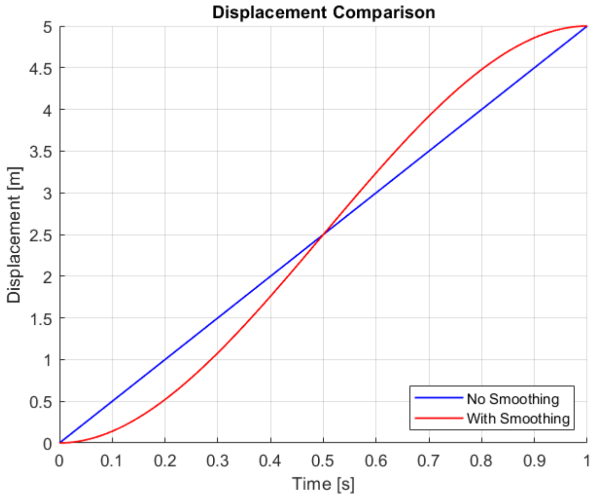

Figure 4.23: Displacement comparison with and without the application of the smoothing function

- Smoothing of the imposed displacement on the upper pin reference point. (Figure 4.23 shows the classical applied displacement compared to the smooth one)
- Time period reduced to 1 s

When changes, like the one previously listed, are applied to a model there is the risk that the results are not coherent with the real phenomena. To avoid this problem it is necessary to pay attention to the followings:

- No abrupt changes in the energy must happen. That is why there is a smoothing of the applied displacement (Figure 4.23).
- The mass scaling operation increases the time increment and the kinetic energy. At the end of the simulation it is necessary to check that the kinetic energy is a small fraction compared to the internal energy. If that does not happen the mass scaling factor must be reduced.

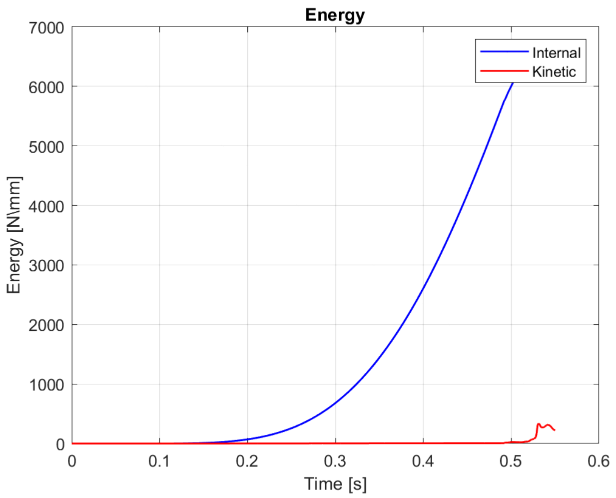

Figure 4.24: Internal and Kinetic energy comparison

The comparison between internal and kinetic energy of the analysis is shown in Figure 4.24: the kinetic energy is a very small fraction compared to the internal energy so the chosen mass scaling factor doesn't influence excessively the results.

- It is better to use a double precision floating point format.

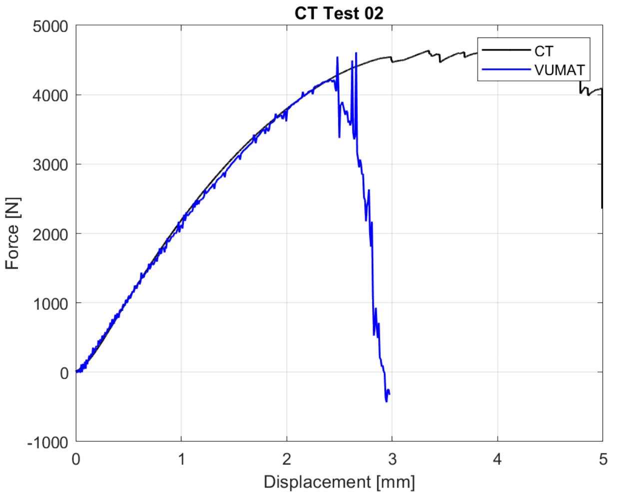

Figure 4.25: Numerical and experimental comparison with VUMAT model

Figure 4.25 shows the comparison between CT test data and the numerical VUMAT results:

- The elastic behavior is perfectly calculated by the model;
- The small pseudo-plastic behavior due to the thermoplastic matrix is correctly evaluated by the FE model;
- Because of the mass scaling and increased velocity of the model some vibrations appear in the curve that do not represent the real behavior of the sample;

- The failure of the model appears with the correct force value but at a lower displacement level. The test coupon, because of the breakage of fibers in compression, undergoes both delamination and interpenetration of the laminae after the first crack propagation step. This phenomena is not taken into account in the numerical model and this could be the reason of the different failure displacements.

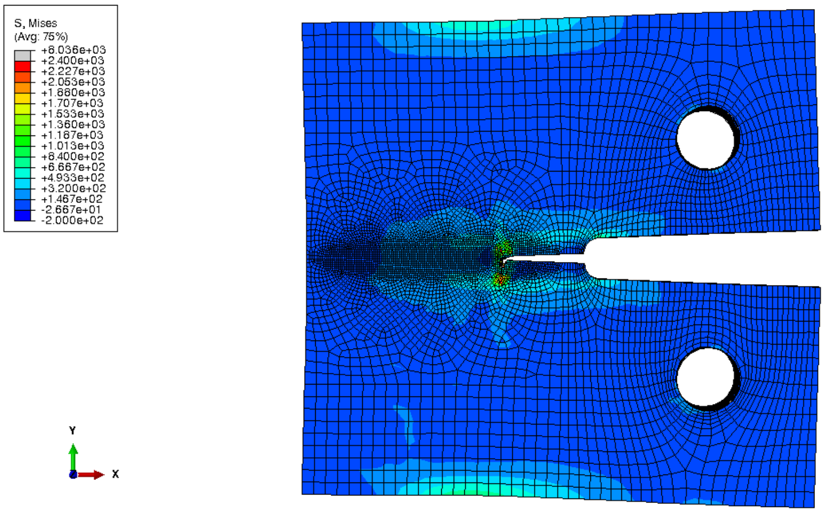

Figure 4.26: Mises stresses map on the CT coupon

The stress distribution of the numerical model is coherent with the expected distribution shown in Figure 4.12. Moreover the failure pattern (Figure 4.27) seems correct compared to the test one shown in Figure 4.18.

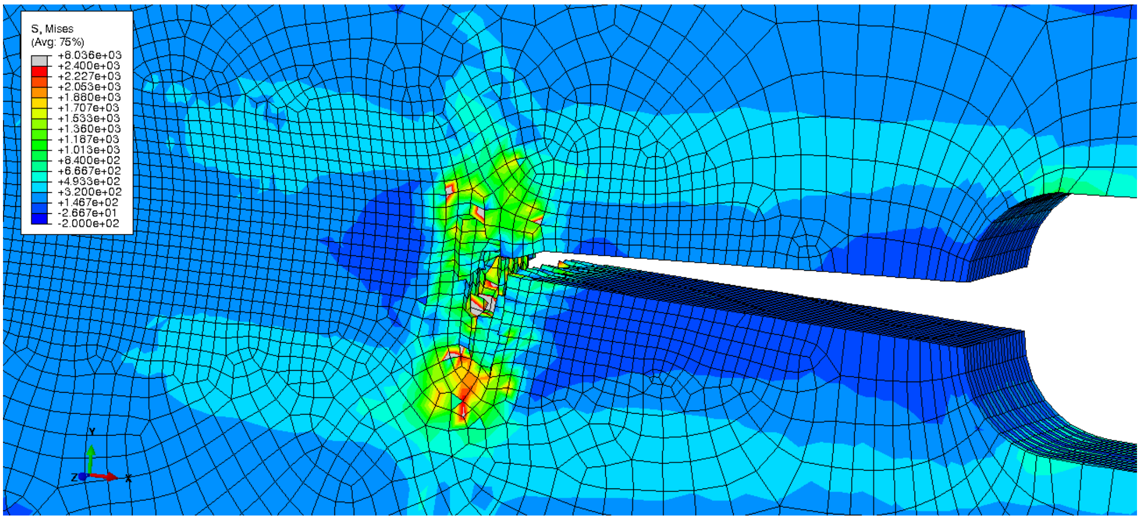

Figure 4.27: Numerical failure pattern

Chapter 5

Static validation: compact compressive test (CC)

5.1 Sample geometry

The specimens used for the compact compressive tests are reminiscent of those proposed by the ASTM-D5045 standard. The geometry and dimensions of the sample used for the tests here described are presented in Figure 5.1 .

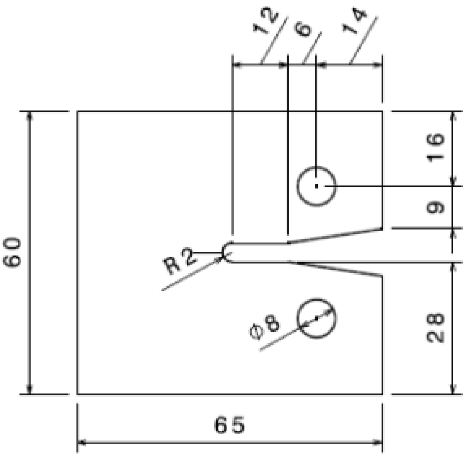

Figure 5.1: CC test coupon geometry

The material used is the one presented in Section 3.3 with the following stacking sequence: $[0 \quad 90]_{5s}$

5.2 FEM model: UMAT and Hashin

The coupon is modeled using ABAQUS/CAE. Using the same approach of the CT tests, two models are created: one model uses the Hashin model to define material's behavior and the other uses the UMAT subroutine. Differences between the two models are explained in the following sections.

5.2.1 Geometry

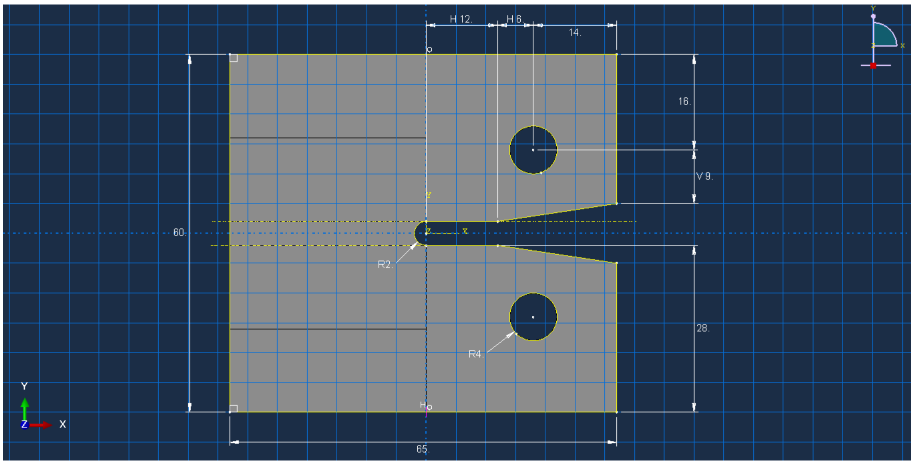

Figure 5.2: 2D Sketch of the CC coupon

The 3D volume representing the CC sample is created starting from the sketch showed in Figure 5.2 and then extruded in order to obtain the wanted thickness of 3.7 mm.

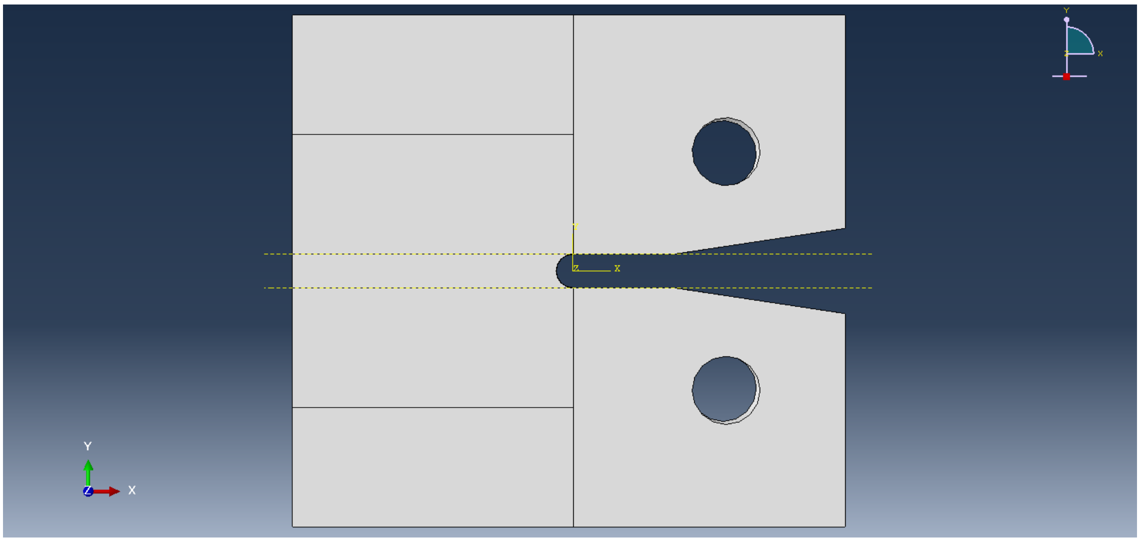

Figure 5.3: Cells partitions

In order to facilitate the meshing phase the partitions in the volume showed in Figure 5.3 are created. Because of the operating method of the UMAT, it is necessary to apply an additional partition to the dedicated model: in the thickness direction one cell per ply has to be created (Figure 5.4).

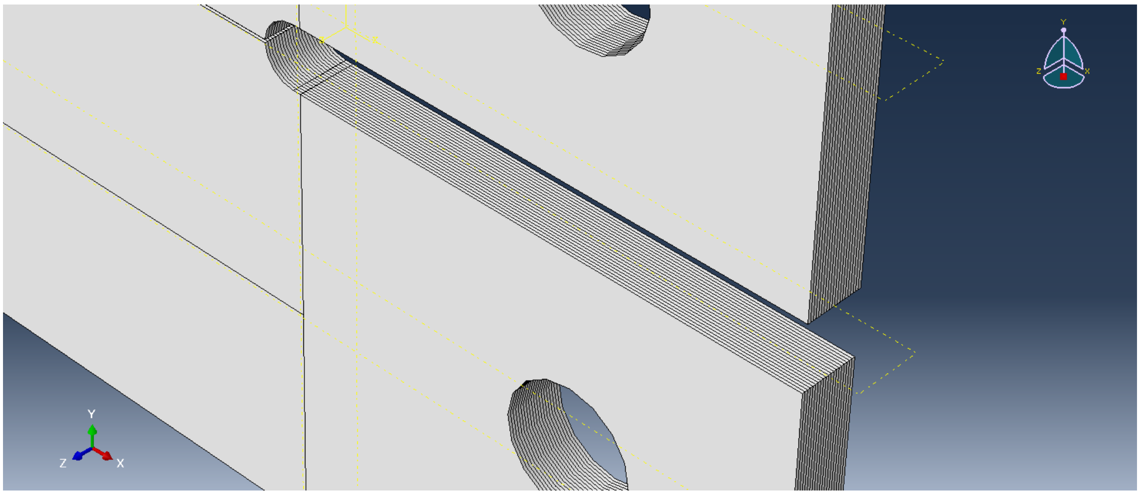

Figure 5.4: Thickness partition detail in the UMAT model

The cylinders representing the loading pins are modeled in the same way used for the CT coupon (Section 4.2.1). The final assembly is showed in Figure 5.5.

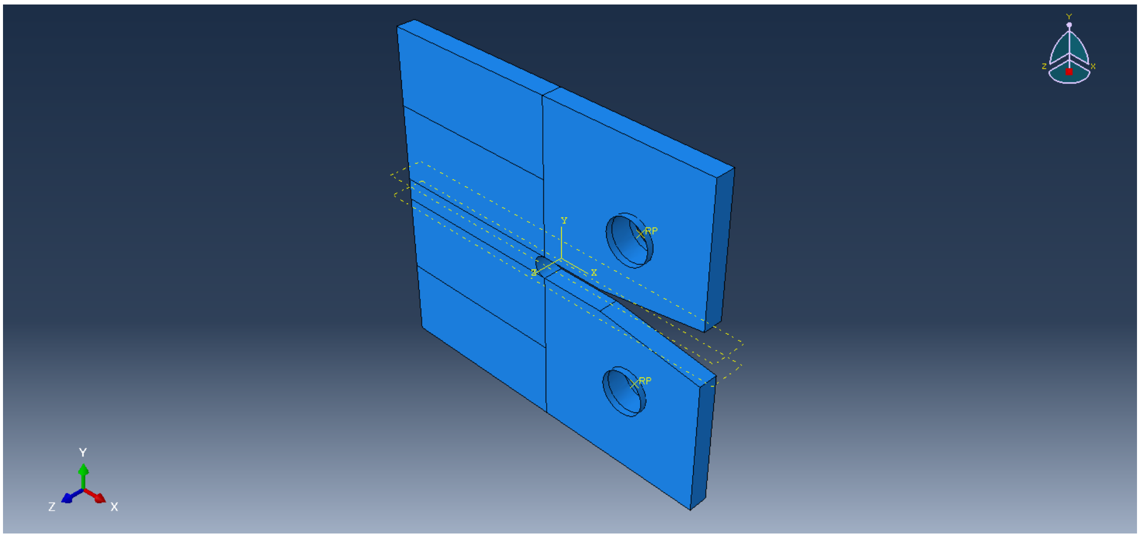

Figure 5.5: CC models final assembly

5.2.2 Mesh

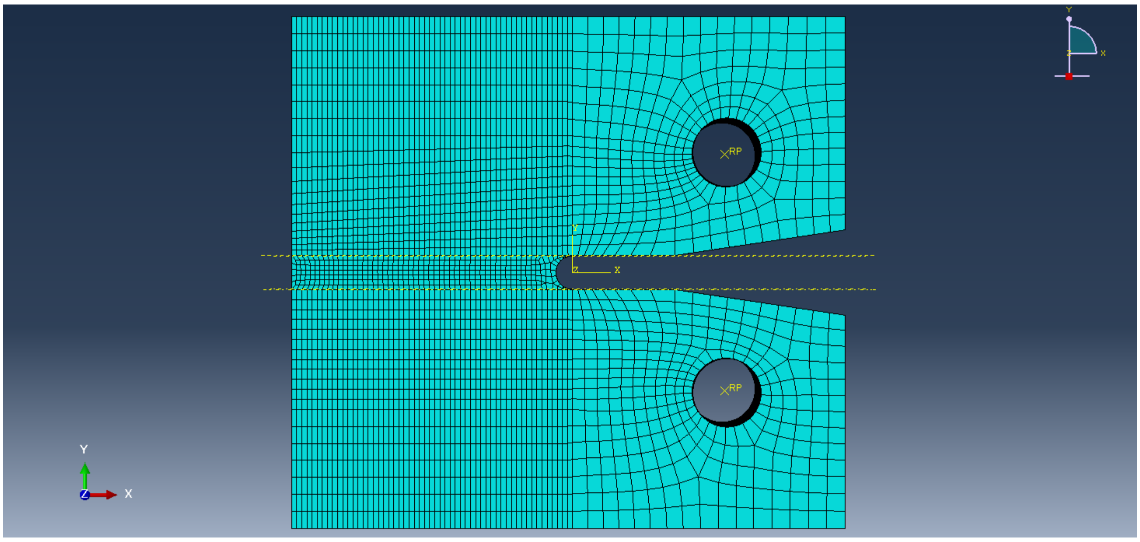

Figure 5.6: Mesh morphology of the CC coupon

As can be seen in Figure 5.6 different mesh dimensions are used in order to discretize the sample correctly without increasing excessively the computational cost. To achieve this result, the characteristic mesh size is set to 2 *mm* away from the expected failure area where the mesh dimension is refined to 0.4 *mm*. The element types used are the same type of the CT coupon model (Section 4.2.2). Cylinders representing the loading pins are treated the same way as the CT coupon ones.

5.2.3 Boundary conditions

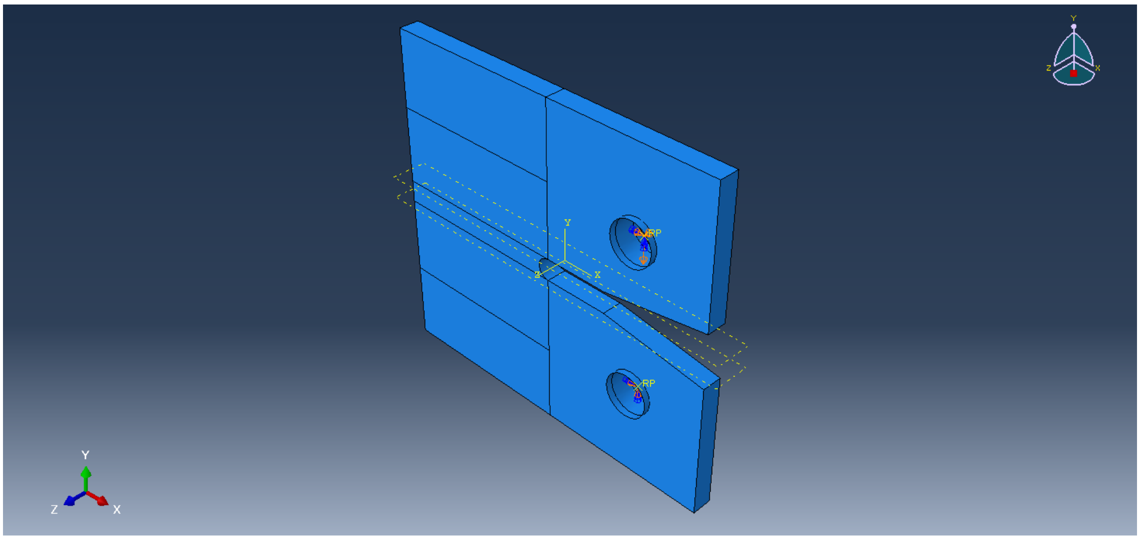

Figure 5.7: Boundary conditions

With the aim of simulating the real test loading process the following boundary conditions are applied to both the Hashin and UMAT model (Figure 5.7):

- clumping conditions at the reference point defined at the center of the lower cylinder ($U_x = U_y = U_z = 0$ $U_{Rx} = U_{Ry} = U_{Rz} = 0$)
- $U_x = U_z = U_{Rx} = U_{Ry} = 0$ at the reference point defined at the center of the upper cylinder
- $U_y = -5$ mm at the reference point defined at the center of the upper cylinder

As for the CT test model (Section 4.2.3), since in the Hashin model the volume of the sample is discretized using just one element in the thickness direction, it is necessary to apply an additional condition in that model to obtain a plane strain condition: for this reason $U_z = 0$ is applied to the whole CC coupon part.

Finally contacts between the loading pins and the coupon are defined as hard contact with a friction coefficient of 0.15.

5.2.4 Analysis

The analysis settings are the same used for the CT test showed in Section 4.2.4.

5.3 Test setup and procedure

The tests are performed using an Instron machine following the procedure of the ASTM5045 [29]. A compressive displacement rate of 0.5 mm is imposed to avoid dynamic effects during the experiment. Exactly how it gets done for the CT tests (Section 4.3.1) two CCD cameras are placed on one side of the machine in order to record not only the crack propagation but also deformations of the specimen's face. Also in this case, the recorded face is painted in order to allow the camera to better recognize different points of the specimen separately (Figure 5.8).

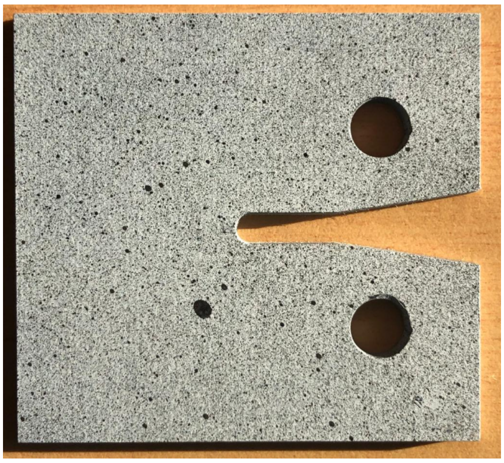

Figure 5.8: CC coupon face painted for augmented detectability

The procedure of the experiment can be summarized as follows:

1. The coupon is placed in the machine. The metal pin is inserted through the hole in the upper support making it coincide with the upper hole of the specimen. The machine is then adjusted so that the hole in the lower support

and the lower hole of the coupon are aligned, at this point the lower pin can be inserted

2. The top cross-bar of the Instron machine starts moving down with the chosen velocity. The compression movement continues until a crack is generated in the correct area.
3. The load is reversed and the coupon is pulled into traction until it goes back to its original position
4. A second compressive load cycle is applied until the compressive load reaches the first breakage level again

It is necessary to carry out an entire compression-traction-compression cycle in order to perform the data post-processing using the area method (Section 4.3.2)

During test the following parameters are measured:

- Displacement of the machine
- Load applied to the machine
- Crack length visually measured from the images taken by the CCD cameras
- Specimen deformation through the CCD cameras

5.4 Numerical and experimental results comparison

Figure 5.9: CC coupon after test

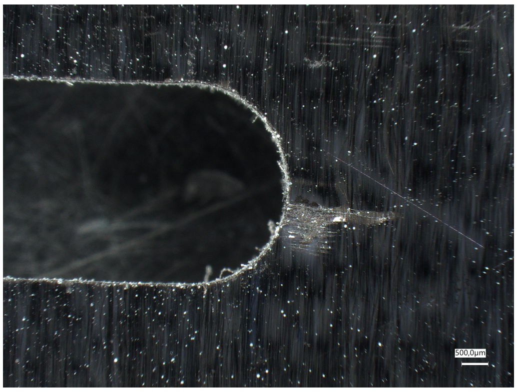

Figure 5.10: Detail of crack in the CC sample

As shown in Figure 5.9 and Figure 5.10 a crack of 2 *mm* is generated during test in the compressed area. It is interesting to highlight that just one step of propagation appears and that is because only one cycle of compressive-tractive-compressive forces is applied. Load displacement graph of the first coupon is shown if Figure 5.11.

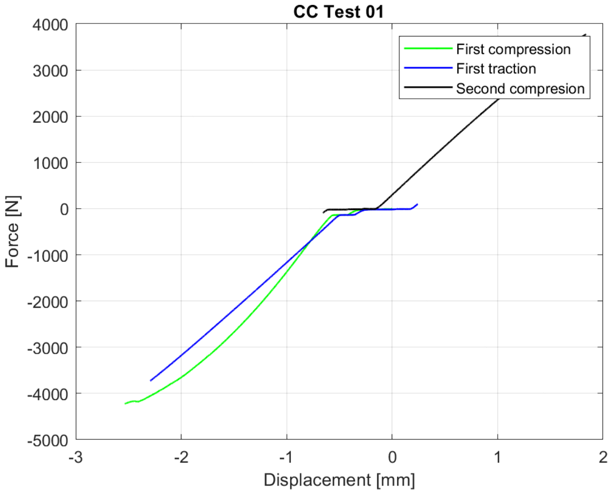

Figure 5.11: Load-displacement history during CC test

Observing the graph it is immediately noticeable the displacement with no associated force that appears between 0 mm and 0.5 mm. This part of the curve is due to some movements of the test setup which is not perfectly interlocked. This phenomena does not appear in the CT tests because a traction pre-load is applied in that case to avoid the problem, this solution, however, is not applicable with compressive loads.

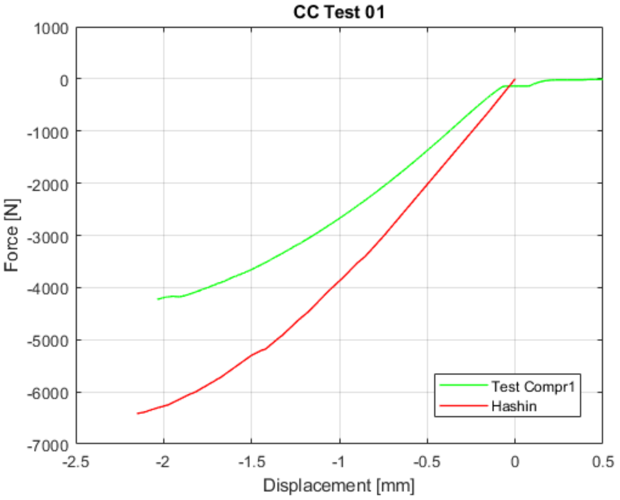

Figure 5.12: First compressive loading test results compared with Hashin model results

With the aim of comparing test results with the Hashin FEM model, test curves are translated horizontally. This process makes it possible to eliminate the firsts displacements caused by machine movements. Observing the graph in Figure 5.12 one notices some differences:

- The FEM model is way stiffer than the test coupon: this is mostly because displacement of the machine is measured and not the real displacement of the coupon. As done for the CT tests (Section 4.6), during post-processing, test's displacement are multiplied by a constant factor of 0.25 in order to take into account differences between sample and machine's displacement.

- It is also necessary to consider that because of fiber misalignment stiffness in fiber's direction with compressive load can be up to 25% lower than in tensile loading. In order to consider this phenomena E_{11} is decreased by 25% in the Hashin ABAQUS model. This modification its not necessary in the input properties of the UMAT model because the *COMPRESSION* subroutine does it automatically.
- The model doesn't find the correct breaking point. Using the area method the correct compressive critical strain energy release rate is calculated and results in: $G_{Ic} = 32\ kJ/m^2$. During this calculation e_p is considered as half of the real thickness of the specimen because only layers with fibers in load direction give contribution in resisting the compressive load, that is half of the coupon layers.

After updating the model with the new informations it follows better all the experimental results but the breaking force and displacements are still too high (Figure 5.13).

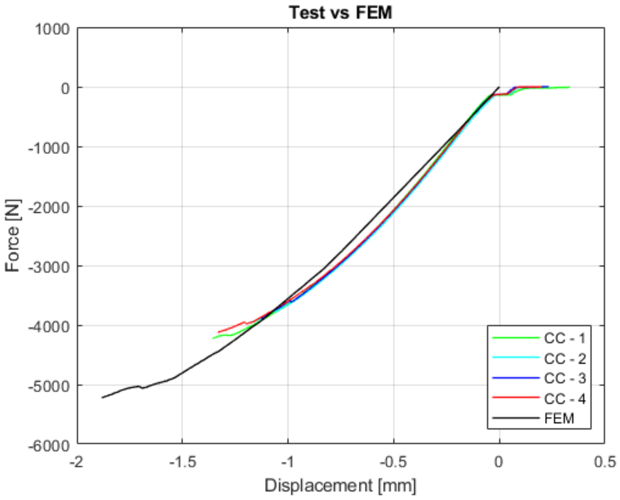

Figure 5.13: Comparison between CC test data results and updated Hashin FEM model

After all the model's informations are updated, they can be applied to the UMAT model that can be finally compared with test results.

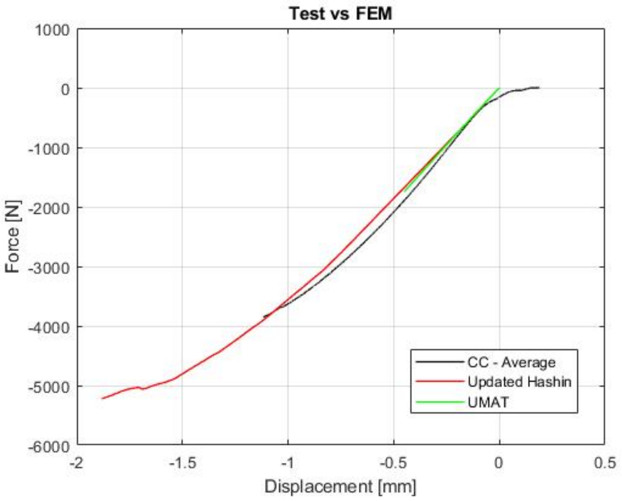

Figure 5.14: Numerical and experimental comparison with Hashin damage model and UMAT model

Figure 5.14 shows the comparison between the averaged experimental results and numerical results calculated with both the UMAT subroutine and the Hashin model. Exactly as the CT tests (Section 4.7) there is non convergence of the analysis after a few steps. It is still possible to observe that, as long as it converges, the UMAT graph follows the test behavior correctly.

In order to overcome the convergence issue an explicit analysis is run on the FEM model using, therefore, the VUMAT subroutine instead of the UMAT. This, as explained in Section 4.8, gives the possibility to check the accuracy of the material model even if convergence issues will still need to be solved with the implicit subroutine. To be able to run the CC test explicit simulation, the same modifications applied to the CT UMAT model, described in Section 4.8, need to be performed on the CC UMAT model. The obtained results are shown in Figure 5.15.

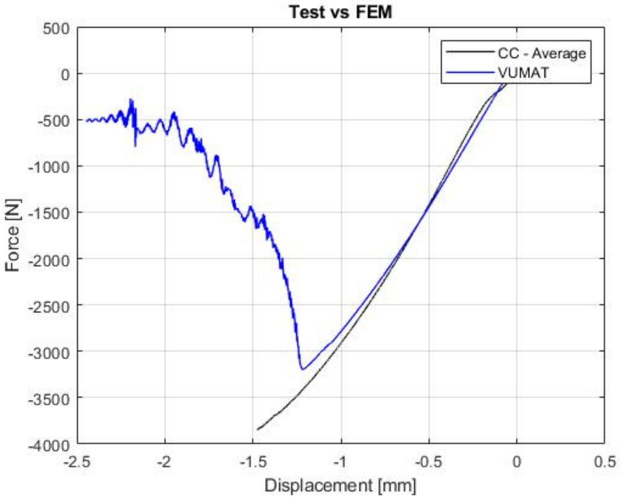

Figure 5.15: Numerical and experimental comparison with VUMAT model

The following observations can be done:

- The elastic behavior is correctly calculated by the model;
- The model is able to simulate the small pseudo-plastic behavior that the coupon shows because of its thermoplastic matrix;
- Because of the mass scaling and increased velocity of the model, after failure, some vibrations are visible in the results graph that do not represent any physical behavior. Figure 5.16 shows, however, that kinetic energy remains a small fraction compared to the internal energy for the whole analysis. Because of this, the results can still be considered acceptable;

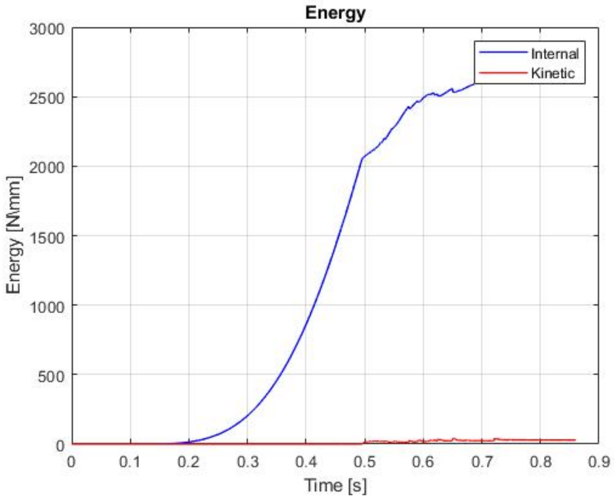

Figure 5.16: Internal and kinetic energy comparison

- The failure of the model appears with lower force and displacement compared to the real one.

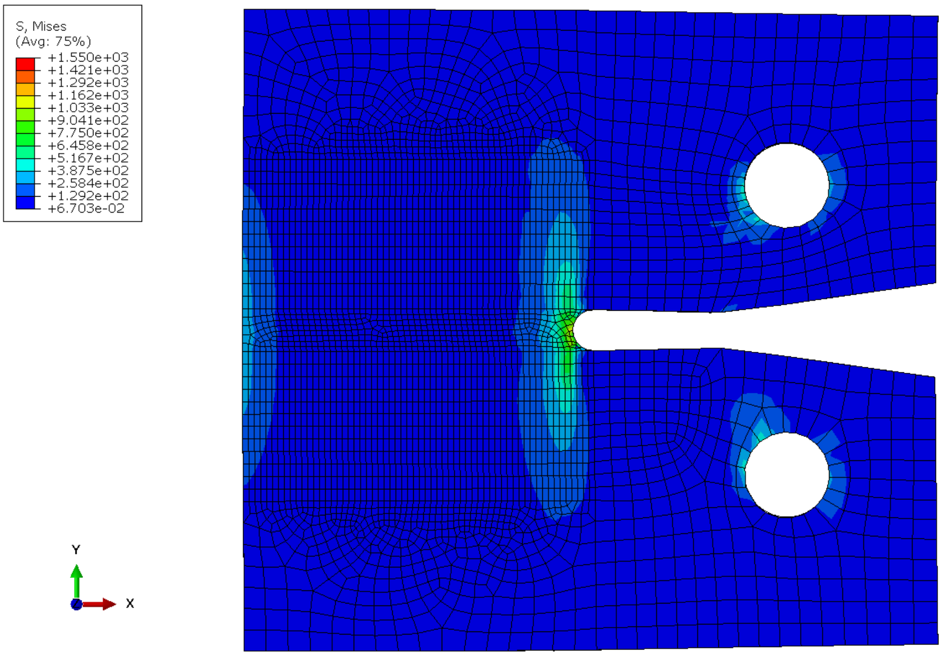

Figure 5.17: Mises stresses map on the CC coupon

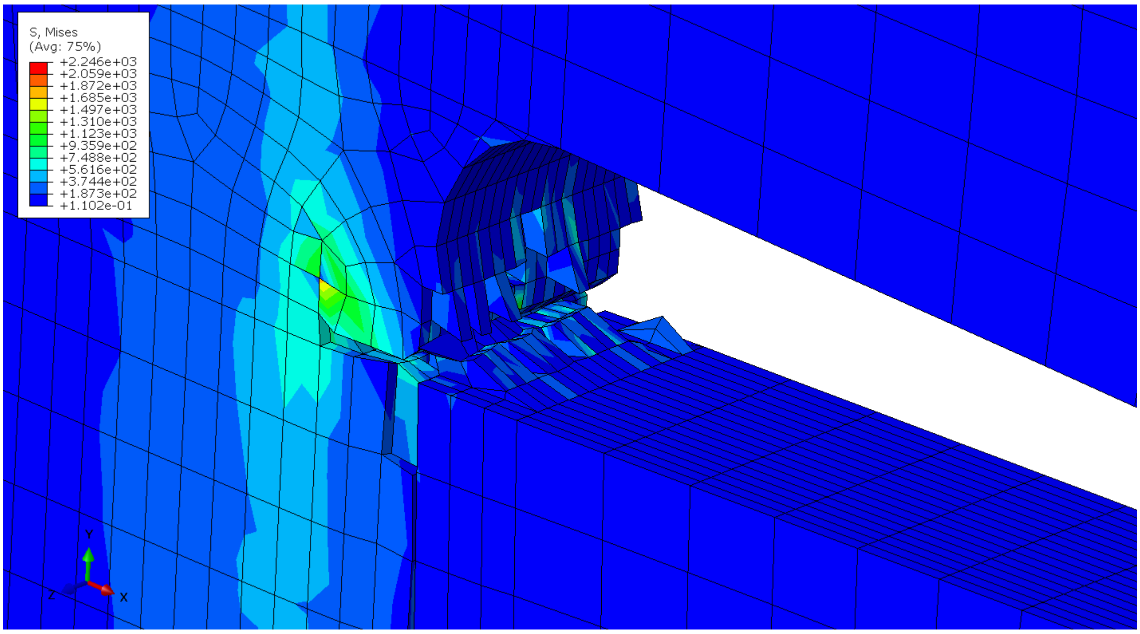

Figure 5.18: Numerical failure pattern

The stress distribution of the numerical model shown in Figure 5.17 is coherent with the expected one. Moreover the failure pattern (Figure 5.18) seems correct if compared to the test one (Figure 5.9).

Chapter 6

Dynamic application: Hopkinson bar test

It is widely demonstrated that the longitudinal tensile properties of UD carbon fiber are not strain rate sensitive [13]. For the longitudinal compressive properties, however, different results can be found in literature.

In recent years the split Hopkinson pressure bar (SHPB) has become a popular tool in the study of the dynamic behavior of materials. This testing device dates back to 1914 when Hopkinson designed it to measure transient impulsive stresses. The bar was then further updated by Kolsky and is now the most common experimental method used in the study of engineering materials under high strain rate loading ranging from $10^3\frac{1}{s}$ to $10^4\frac{1}{s}$ [34].

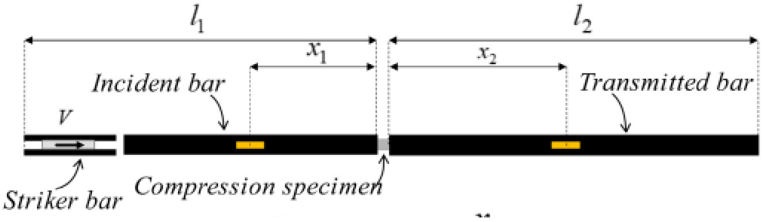

Figure 6.1: Schematic configuration of the SHPB

The Hopkinson bar consists of a set of two cylindrical steel bars that are both free to move along their common axis. Along this line, a shorter bar, referred to as the striker bar, can be accelerated to a certain velocity using for instance compressed gases or a mechanical mechanism. When the striker bar impacts the incident bar an incident elastic stress wave is generated. The wave thus generated partly reflects onto it when it impinges upon the specimen ultimately reaching the transmitted bar (see Figure 6.1). That is because of the change in impedance at the interface between the sample and the entry bar that results in the reflection of part of the entry pulse and the transmission of the remaining portion. The incident stress pulse and the transmitted stress pulse are measured in real life during the test using gauges on the incident and transmitted bars. If the two bars remain elastic and the wave dispersion is ignored, then the measured stress pulses can be assumed to be the same ones acting on the sample. Starting from wave propagation theory it is possible to deduce the equations to be used to extract the stress-strain curve in the sample using SHPB test output data.

In the following sections compressive SHPB tests are performed on the material defined in section 3.3 in order to initiate the comprehension of its behavior under loads with different strain rates. The experimental results are subsequently compared with the numerical results obtained through an ABAQUS model of the setup which utilizes the VUMAT subroutine. These tests aim to be the basis for an update of the VUMAT model that will take into account differences in the material behavior owed to a variation of strain rate in the loading.

6.1 Sample geometry

In designing the sample for a compressive SHPB test it is decisive to consider the following things:

- The length of the coupon has an impact in the maximum strain rate that can be reached during the test. Typically the longer the coupon the lower the strain rate.
- The specimen must be short enough to allow stress equilibrium to occur in a reasonable time scale [35].
- The thickness of the specimen, besides the implications on the strain rate, needs to be high enough to not make the coupon bend during test. At the same time it should not be too high to avoid too much resistance of the specimen that can cause breakage in the bars.
- The section of the specimen should be completely within the bars at which it is attached.

Different coupon geometries can be found in literature, specifically the ones initially chosen in the present case are shown in Figure 6.2 [13].

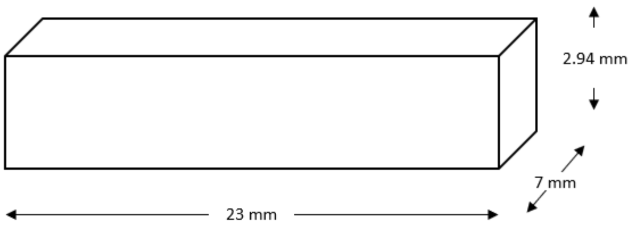

Figure 6.2: SHPB sample geometry and dimensions

6.2 FEM model: VUMAT

The test setup is simulated using ABAQUS/CAE and the VUMAT subroutine (Chapter 3). In order to reduce the computational cost, the symmetry of the problem is exploited so just a quarter of the setup is actually modelled.

6.2.1 Geometry

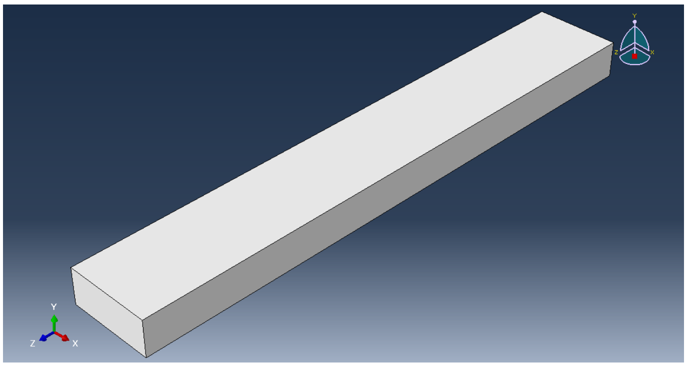

Figure 6.3: Coupon part

Three parts are created in order to simulate the test setup:

- The coupon: a three dimensional cuboid with the dimensions of a quarter of the specimen (Figure 6.3)

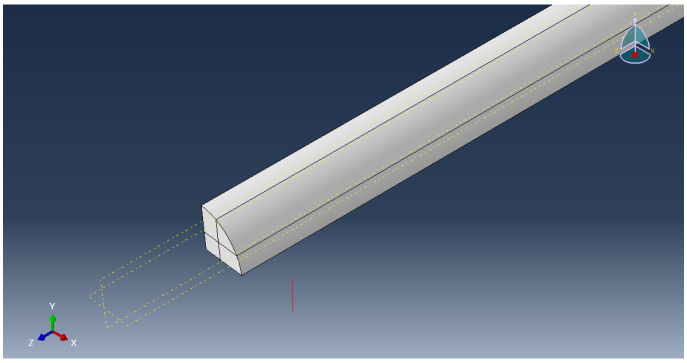

Figure 6.4: Striker part

- A quarter of a 20 mm diameter cylinder representing the striker bar with a length of 500 mm (Figure 6.4)
- A quarter of a 20 mm diameter cylinder representing the incident bar with a length of 2000 mm
- A quarter of a 20 mm diameter cylinder representing the transmitted bar with a length of 2000 mm

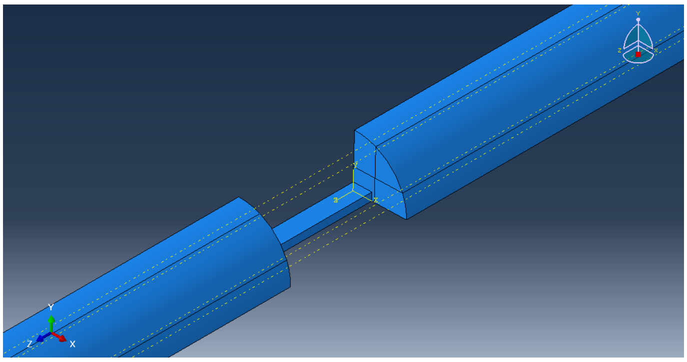

Figure 6.5: Test set-up assembly

A detail of the assembly is showed in Figure 6.5.

6.2.2 Mesh

Considering that the bars are not the target of the analysis and that they do not have particular geometrical characteristics or properties that require special attention, C3D8 elements with an average characteristic length of 5 mm are chosen for them.

Regarding the coupon it is necessary to do a convergence analysis to understand the best mesh dimensions. The element type is C3D8R for the coupons as well. The results are showed in Figure 6.6.

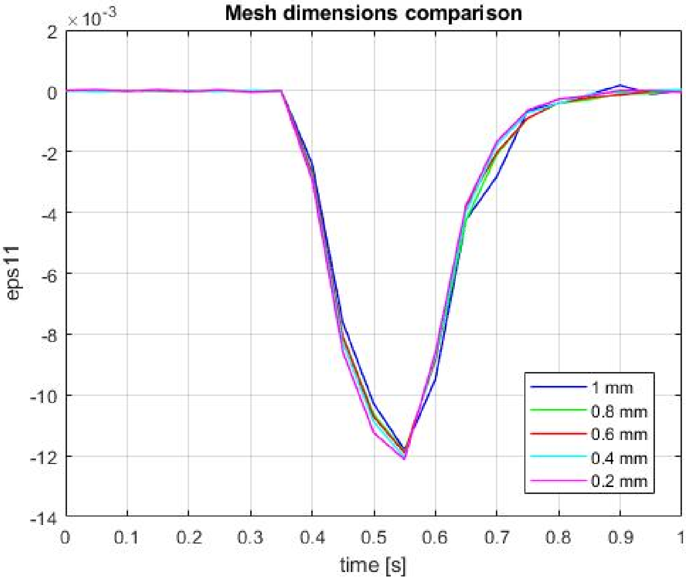

Figure 6.6: Mesh dimension convergence analysis

Except for the 1 mm mesh which is too rough for the coupon dimensions, all the other dimensions imply very similar results. In order to have a mesh that is fine enough and at the same time not too much time consuming, the 0.4 mm characteristic element length is chosen.

6.2.3 Boundary conditions

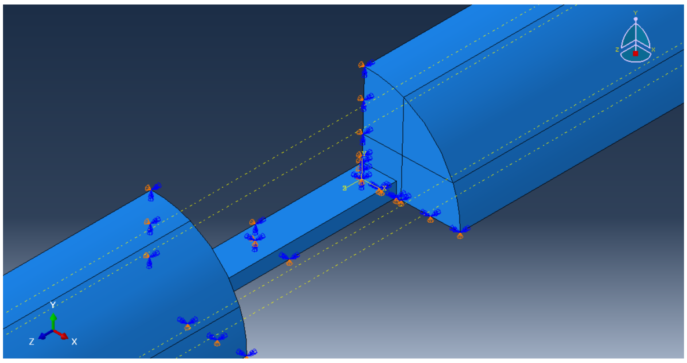

Figure 6.7: Symmetry boundary conditions

As shown in Figure 6.7, boundary conditions are applied on the symmetry planes to take into account the volumes that are not modeled. Specifically the following degrees of freedom are blocked:

- On the YZ plane: $U_x = U_{Ry} = U_{Rz} = 0$
- On the XZ plane: $U_y = U_{Rx} = U_{Ry} = 0$

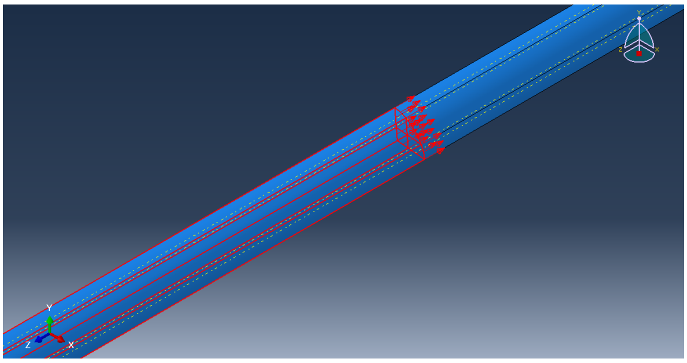

Figure 6.8: Applied velocity on the striker bar

The movement is given to the striker bar through the application of a velocity to it in the axial direction as showed in Figure 6.8. This velocity changes in different analysis based on the ones used during tests.

6.2.4 Analysis output requests

The output requested for the analysis are the strain in three elements of the model:

- Central element of the coupon
- Central element of the entry bar
- Central element of the exit bar

6.2.5 Post processing: strain rate calculus

After data are collected from the ABAQUS model analysis they can be used to obtain an idea of the strain rate ranges reached by the coupon. This calculus is very important in order to evaluate the velocity of the striker bar to impose during the testing phase.

The strain rate can easily be defined as follows:

$$\dot{\epsilon} = \frac{\delta\epsilon}{\delta t} \tag{6.1}$$

In order to calculate it with the data obtained from the analysis that are in a discrete number it is necessary to calculate the derivative through the finite differences method:

$$\dot{\epsilon} = \frac{\Delta\epsilon}{\Delta t} \tag{6.2}$$

This is calculated for every time step obtaining the strain rate time history (Figure 6.9).

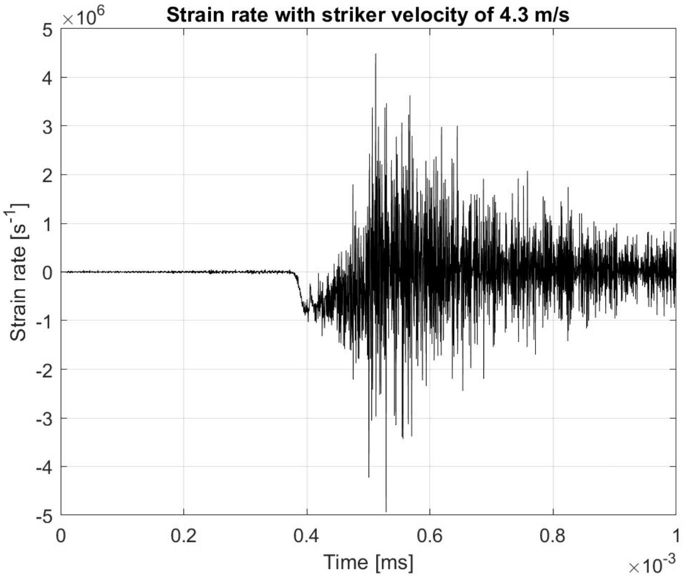

Figure 6.9: Example of strain rate output

Since the graph obtained with this method has a lot of noise it is necessary to use a filter to obtain a smoother signal. The filter used is the Savitzy-Golay filter 6.10.

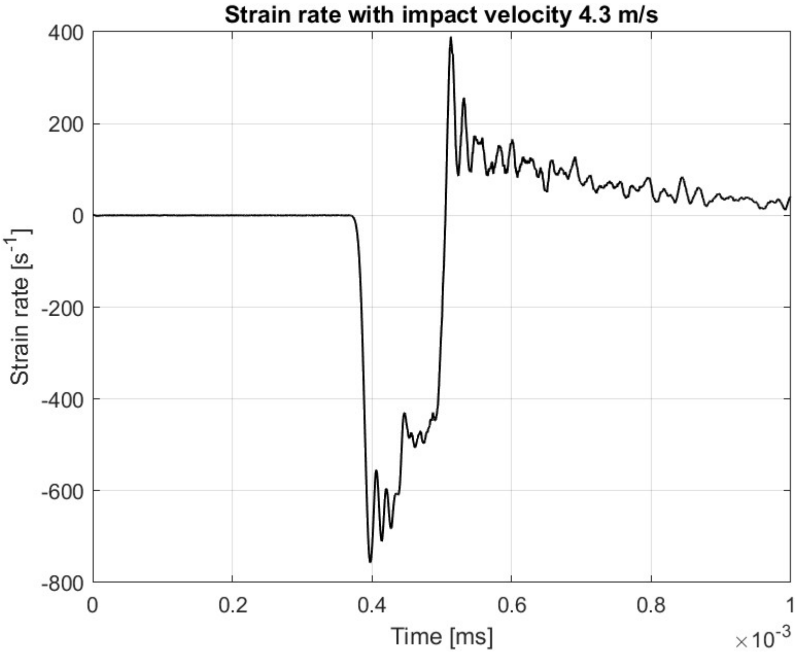

Figure 6.10: Example of strain rate output after smoothing

Various methods exist to smooth noisy signals but the Savitzy-Golay filter stands out with its ability to smooth data while preserving the features of the original signal, such as peaks and valleys, which might be lost with other smoothing techniques. This makes it particularly useful in applications like this one where is fundamental to preserve the shape of the curve. This filter smooths data by fitting a successive sub sets of adjacent data points with low degree polynomial using the method of the linear least squares

The core idea is to approximate the data points within a moving window by a polynomial of a certain degree. If there is a set of data points (x_i, y_i) where i ranges form 1 to N, the goal is to fit a polynomial of degree p to these points. The polynomial can be expressed as follows:

$$y = a_0 + a_1 x + a_2 x^2 + ... + a_p x^p \tag{6.3}$$

For a given window of data points centered in x_k, it is necessary to determine the coefficients a_i to obtain the polynomial data that fits best the data points. This is achieved by minimizing the sum of the squares of the differences between the actual data points y_i and the corresponding polynomial values y_{ih}:

$$min \sum_{i=-m}^{m} (y_{k+1} - \sum_{j=0}^{p} a_j x_{k+1}^{j})^2 \tag{6.4}$$

6.3 Test

6.3.1 Experimental setup and procedure

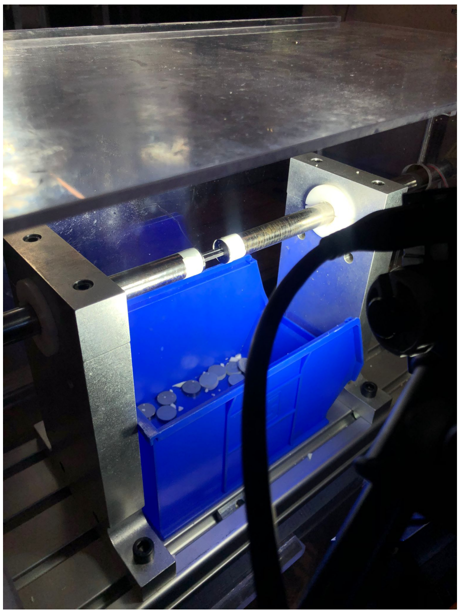

Figure 6.11: Test setup

The tests are performed using a split Hopkinson pressure bar custom built by Institut Clément Ader (ICA). The test setup consists of the following items:

- Three aluminium bars: the striker bar, the incident bar and the transmitted bar whose role during test is further described at the beginning of the current section;
- Two hard metal cylinders: they have the same diameter of the bars and protect them from the impact with the coupon that could damage them. They are positioned at the interfaces between the sample and the bars.

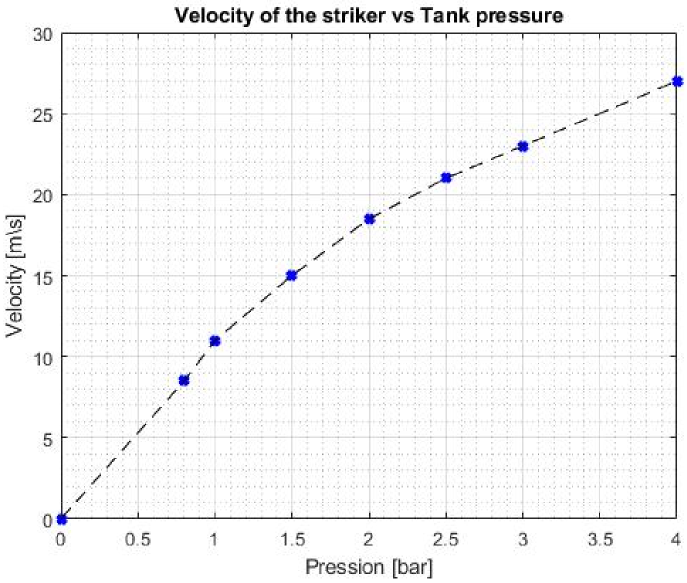

Figure 6.12: Striker bar velocity - tank pressure relation

- Gas tank: It contains the pressurized gas that, when released, gives the initial force to accelerate the striker bar. The pressure of the tank can be modified in order to obtain different velocities of the striker bar. The relationship between the pressure of the tank and the velocity of the striker bar is shown in the graph in Figure 6.12;

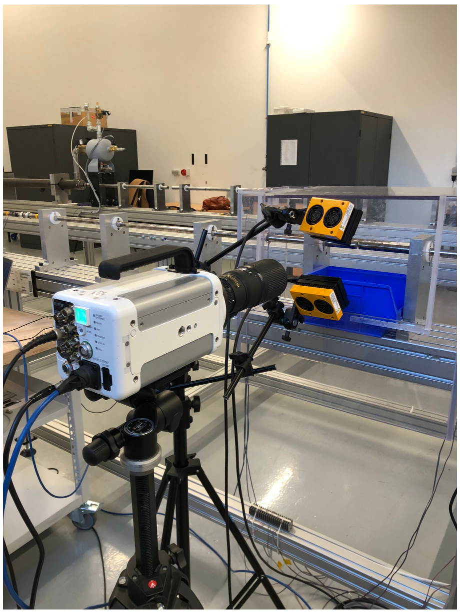

Figure 6.13: High speed camera setup

- High speed camera and lights 6.13: this allows to obtain detailed pictures of the phenomena. The pictures can also be used to directly extract from them the deformation of the coupon;
- Eight strain gauges : four are attached to the incident bar, and four to the transmitted bar. These strain gauges measure the deformation of the bars,

which, as previously explained, will be used to calculate the stress and strain distribution of the coupon during the post-processing phase. The strain gauges are placed in pairs at selected positions on each bar, with each pair mounted on diametrically opposite sides. This setup helps eliminate bending waves during post-processing, ensuring that only pure compression strains are measured. Two positions are chosen on each bar for redundancy.

The dimensions of the whole test setup and the position of the strain gauges is shown in Figure 6.14.

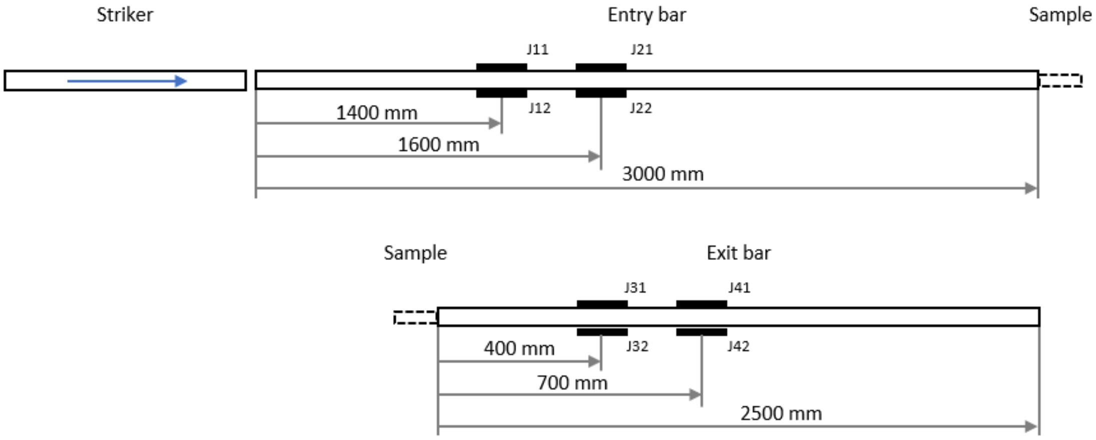

Figure 6.14: Dimensions of the ICA test setup

The following steps summarize the test procedure:

1. The cylindrical interphases between bars and sample is covered in grease. The thin layer of grease allows to smoothen the wave before it hits the coupon obtaining a more clear response;
2. The two cylinders are attached to the bars using adhesive tape;
3. The coupon is positioned between the two bars and blocked there with a little compression;
4. The tank is pressurized
5. Pressure is released from the tank and pushes the striker bar that starts the testing phase;
6. For security reason the tank needs to be depressurized before considering the test concluded;
7. Data from the strain gauges and video from the high speed camera can be visualized.

6.3.2 Experimental data post processing

Starting from the measurements of strains in the bars it is possible to calculate the stress, strain and strain rate of the sample [34]. Having records of the incident, reflected and transmitted pulses (respectively ϵ_I, ϵ_R and ϵ_T) it is possible to establish conditions at the specimen interphase. From the one dimensional theory of elastic wave propagation:

$$u - c_0 \int_0^t \epsilon dt' \tag{6.5}$$

where u is the displacement at time t, c_0 is the wave velocity and ϵ is the strain. The displacement u_1 of the face of the incident bar is the result of both the incident strain pulse traveling in the positive x direction and the reflected strain pulse ϵ_R traveling in the negative x direction, this results in:

$$u_1 = c_0 \int_0^t \epsilon_I dt' + (-c_0) \int_0^t \epsilon_R dt' = c_0 \int_0^t (\epsilon_I - \epsilon_R) dt' \tag{6.6}$$

Similarly, the displacement u_2 at the face of the transmitted bar is calculated using ϵ_T as follows:

$$u_2 = c_0 \int_0^t \epsilon_T dt' \tag{6.7}$$

The nominal strain in the specimen is therefore obtained:

$$\epsilon_s = \frac{u_1 - u_2}{l_0} = \frac{c_0}{l_0} \int_0^t (\epsilon_I - \epsilon_R - \epsilon_T) dt' \tag{6.8}$$

where l_0 is the initial length of the specimen. Expression 6.8 can be simplified if the stress across the specimen is considered constant, this assumption becomes more exact as l_0 approaches zero. If the deformation at the interfaces of the sample are considered equal, the following expression can be written:

$$\epsilon_R = \epsilon_T - \epsilon_I \tag{6.9}$$

By substituting expression 6.9 in 6.8:

$$\epsilon_S = -\frac{2c_0}{l_0} \int_0^t \epsilon_R dt' \tag{6.10}$$

The loads applied on the faces of the sample are shown below:

$$P_1 = EA(\epsilon_I + \epsilon_R) \quad P_2 = EA\epsilon_I \tag{6.11}$$

Hence, the average stress in the specimen σ_s can be expressed as follows:

$$\sigma_s = \frac{P_1 + P_2}{2A_s} = \frac{1}{2} E \left(\frac{A}{A_s} \right) (\epsilon_I + \epsilon_R + \epsilon_T) \tag{6.12}$$

where E is the modulus of elasticity of the pressure bars and $\frac{A}{A_s}$ is the area ratio between sections of pressure bars and specimen. Using 6.9, equation 6.12 can be simplified as shown below:

$$\sigma_s = E \left(\frac{A}{A_s} \right) \epsilon_T \tag{6.13}$$

In all previous expressions the recorded signals ϵ_I, ϵ_R and ϵ_S are shifted along the time axis to have coincident beginnings.
After experimental tests the post processing phase is handled by a Matlab program with the following steps:

1. The signal recorded by the strain gauges in the incident bar corresponds to both the incident and reflected deformation. At the beginning of the program Matlab reads the test output data through a text file.

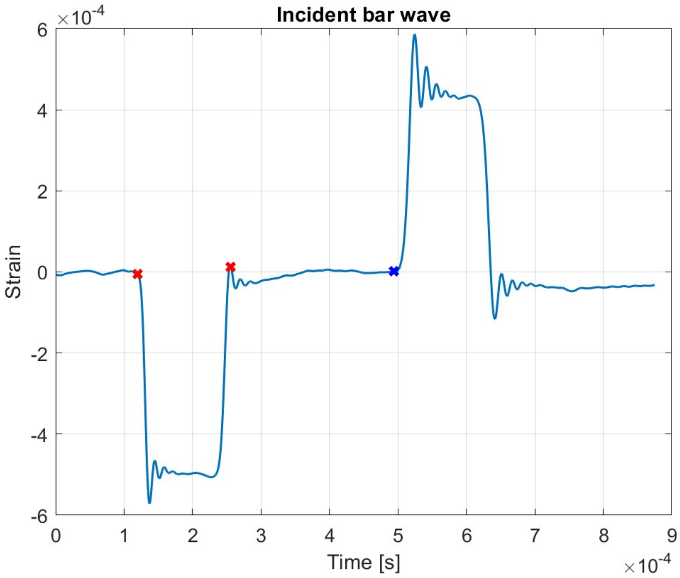

Figure 6.15: Selection of incident and reflected wave limits

2. The user selects the beginning and ending point of the incident wave through an interactive graph. The time-span corresponding to this wave will be considered from this moment on the base time of all the signals (Figure 6.15).

3. The user selects the beginning point of the reflected wave. The ending point is automatically found by the program considering that all signals need to have the same length.

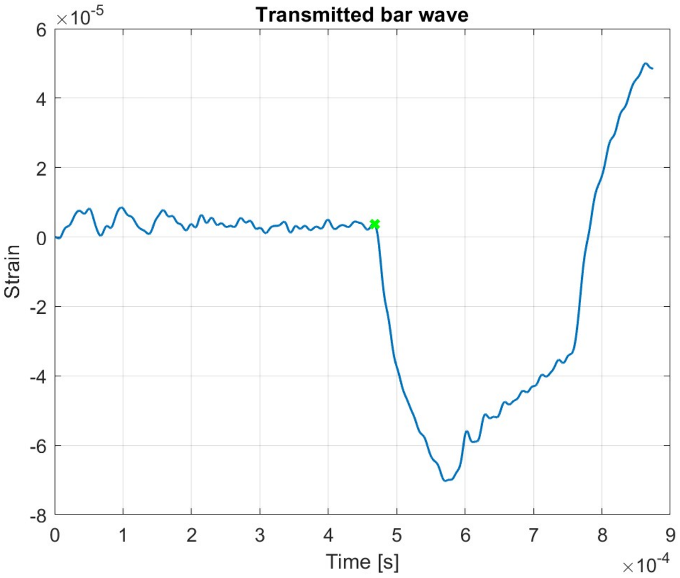

Figure 6.16: Selection of transmitted wave beginning

4. The user selects the beginning of the transmitted wave (Figure 6.16), the ending of it is automatically found using the same logic of the reflected wave.

5. Strain rate is calculated as follows:

$$\dot{\epsilon}_s = \frac{2c_0\epsilon_R}{l_0} \tag{6.14}$$

6. The deformation of the sample is calculated:

$$\epsilon_s = \int_0^t \epsilon_s dt' \tag{6.15}$$

   The integral value is determined using the trapezoidal method.

7. The coupon stress is calculated using equation 6.12;

8. Graphs with stress, strain and strain rate of the sample are shown as final output (Figure 6.17).

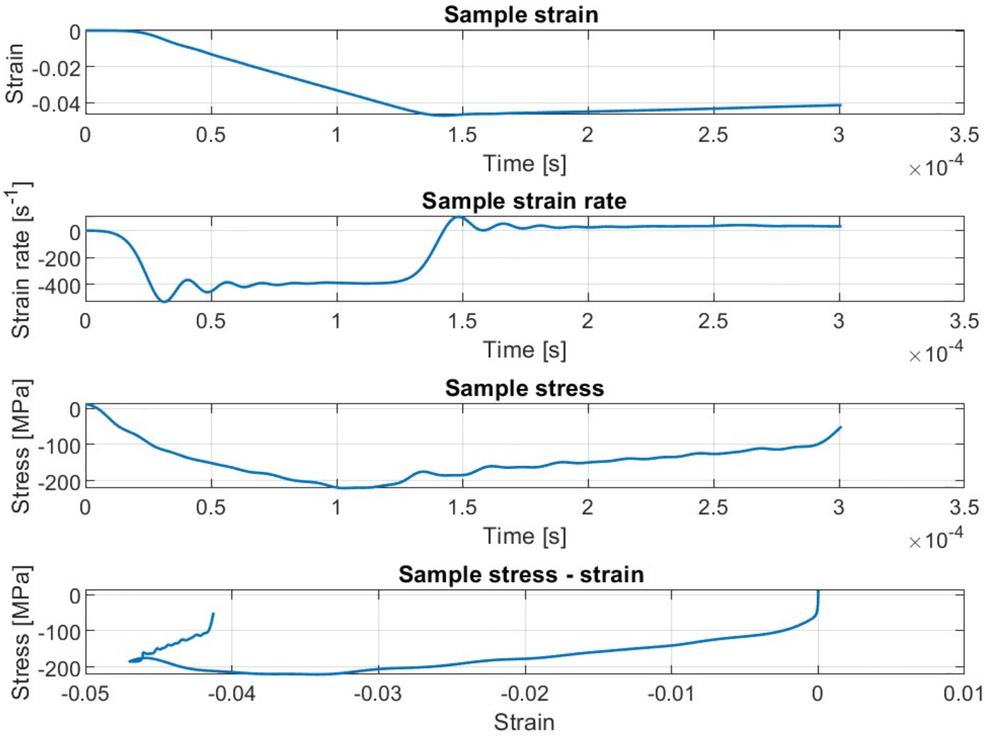

Figure 6.17: SHPB test sample behavior

6.3.3 Preliminary test

The minimum pressure of the machine has been used (0.8 Bar corresponding to a striker bar velocity of 8.5 m/s) but it still resulted in the failure of the coupon as it is shown in the following sections. New tests with lower pressures, and consequently lower striker velocities, need to be performed in order to obtain knowledge about linear behavior of the material.

$[0]_{16}$ **Coupon**

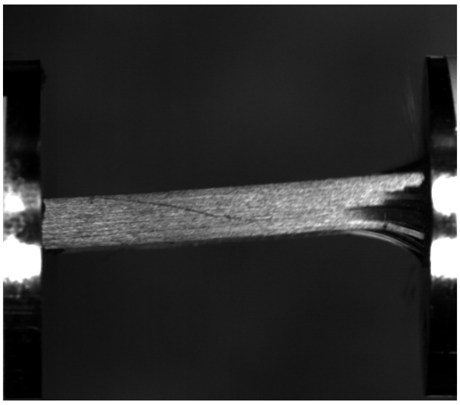

Figure 6.18: $[0]_{16}$ coupon test result

Results obtained with this test cannot be used to have a comparison with the numerical model. As shown in Figure 6.18 the failure of the coupon is due to delamination and not compression. This can be caused by a non perfect contact on the interface between the coupon and supports.

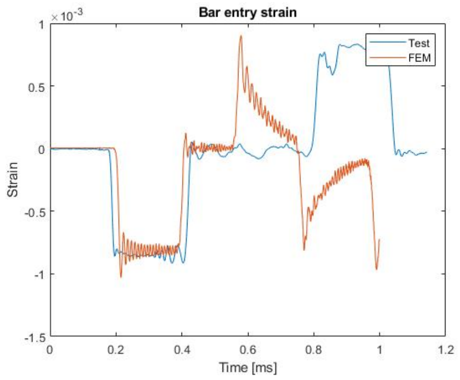

Figure 6.19: Entry bar strain

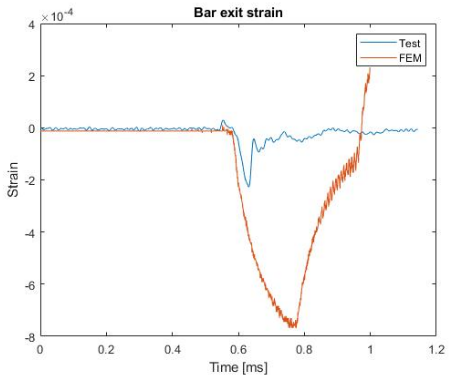

Figure 6.20: Exit bar strain

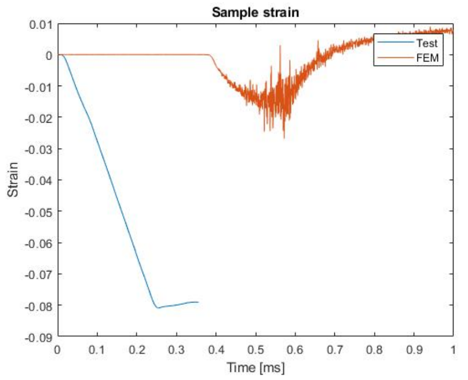

Figure 6.21: Sample strain

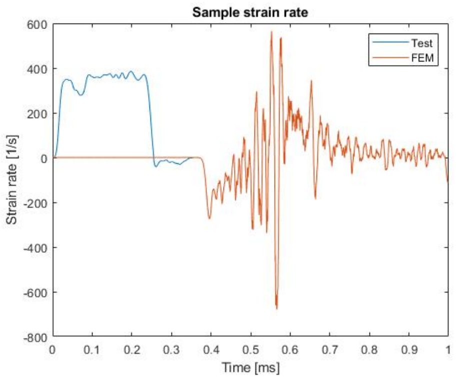

Figure 6.22: Sample strain rate

As noted above, many differences arises from the experimental and numerical comparison shown in Figures 6.19 6.20 6.21 6.22:

- The entry bar strain levels are correctly simulated by the numerical model. It is interesting to notice that the first wave, representing the incident pulse, perfectly overlaps the test curve while the reflected pulse has a different shape. This is due to the fact that the numerical model cannot simulate the breakage of the sample if not caused by compression.

- The numerical exit bar strain level is way higher than the test one. The breakage of the sample reduces the energy transferred to the exit bar that deforms less than expected.

- For the reasons listed above the strain level of the coupon is way higher during test than what the numerical results show

- The numerical model correctly calculates the strain rate level of the coupon.

$[90]_{16}$ Coupon

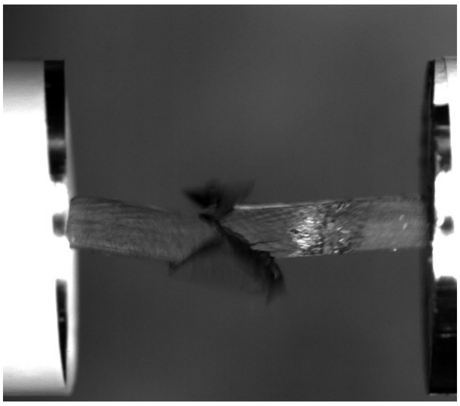

Figure 6.23: $[90]_{16}$ coupon test result

Figure 6.23 shows a classical compressive breakage with the angled failure through the thickness with a striker bar velocity of 8 m/s. Since in this case the coupon broke correctly the data shown are usable but new tests with lower pressures still need to be performed.

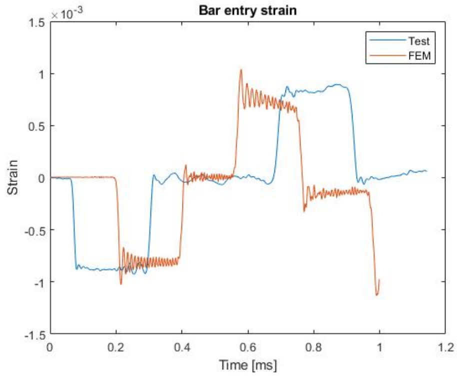

Figure 6.24: Entry bar strain

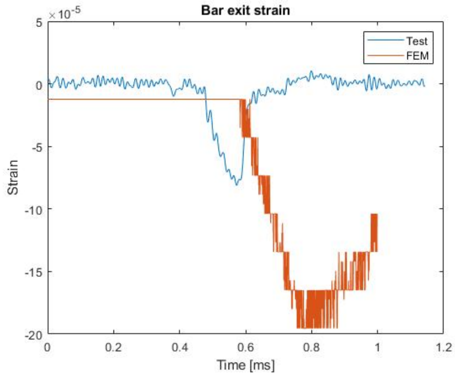

Figure 6.25: Exit bar strain

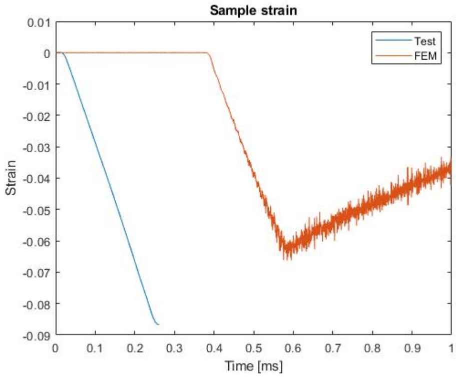

Figure 6.26: Sample strain

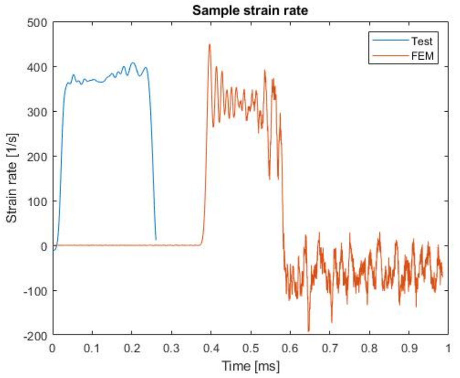

Figure 6.27: Sample strain rate

Figures 6.24 6.25 6.26 6.27 show the comparison between the VUMAT model results and the test data. The following observations can be done:

- The levels of strain and the wave shape of the entry bar is correctly foreseen by the numerical model
- The strain and strain rate graphs of the sample show good accordance between test and numerical results
- The numerical exit bar strain is way higher than the test one.

Figure 6.25 shows clearly how little the transmitted wave is if compared to the entry pulse in Figure 6.24. This is due to the very low impedance of the sample material that can cause the transmitted pulse to be so weak to be confused with noise. Some solutions can be applied to the setup to obtain a stronger signal in the transmitted bar [35]:

- More sensible strain gauges
- Bigger sample transversal area
- Changing the bar material for one with lower impedance to reduce the difference with the sample one

Unfortunately none of these solutions could be applied to the setup used with the available time frame but it is still possible to obtain fairly accurate result even with very weak transmitted wave.

$[+45 \quad -45]_{4s}$ **Coupon**

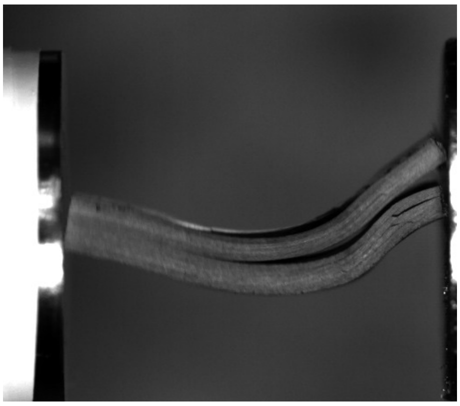

Figure 6.28: $[+45 - 45]_{4s}$ coupon test result

The $[+45 \quad -45]_{4s}$ coupon has undergone an extreme bending condition that resulted in its failure as shown in Figure 6.28. Further tests will be performed with shorter coupons in order to avoid this problem.

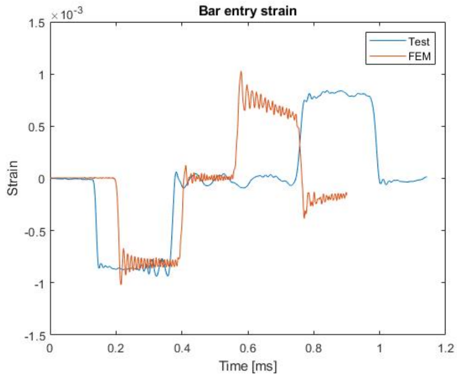

Figure 6.29: Entry bar strain

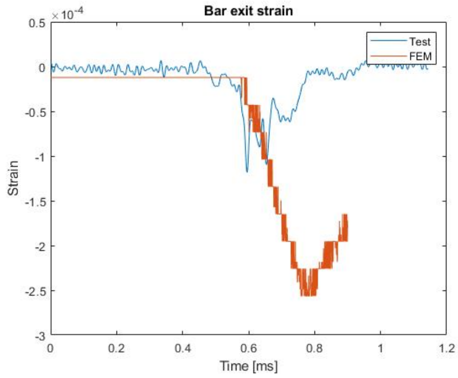

Figure 6.30: Exit bar strain

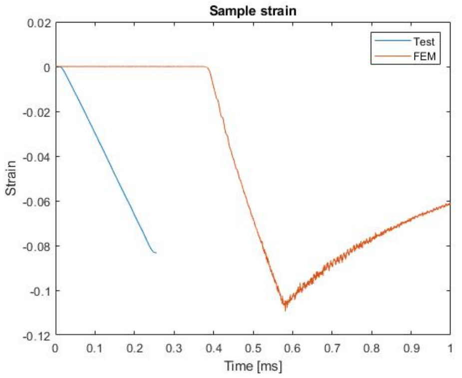

Figure 6.31: Sample strain

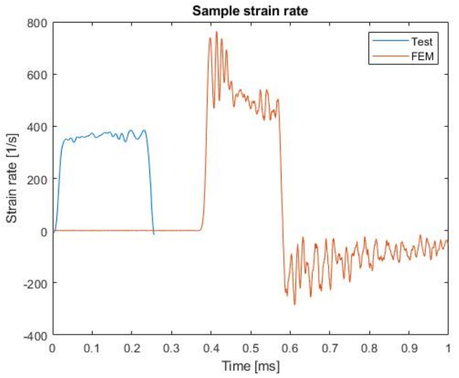

Figure 6.32: Sample strain rate

Figures 6.29 6.30 6.31 6.32 show the comparison between the VUMAT model results and the test data. In this case, like in the $[0]_{16}$ case, the numerical model is not able to simulate the failure of the coupon since that is due to sample imperfections. The following observations can still be done:

- The levels of strain and the wave shape of the entry bar is correctly foreseen by the numerical model
- The strain of the sample show higher results coming from the FE model than test data. That is because in the model the sample does not undergo a failure. For the same reason the numerical exit bar strain is way higher than the test one.
- The FEM model overestimates the sample strain rate levels.

6.3.4 Geometrical modifications

Figure 6.33: Split Hopkinson pressure bar setup at ISAE-Supaero

In order to avoid problems encountered during preliminary testing new dimensions are chosen for the sample geometry (Figure 6.34).

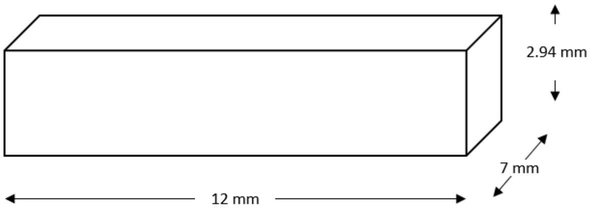

Figure 6.34: SHPB Test sample updated geometry

Moreover a new Split Hopkinson bar with mechanical activation custom made at ISAE Supaero (Figure 6.33) is used in place of ICA's setup. This choice is made because through mechanical activation it is possible to generate less intense waves that coupled with shorter specimens should result in a non-break of the sample. This should allow to observe elastic behavior of the material.

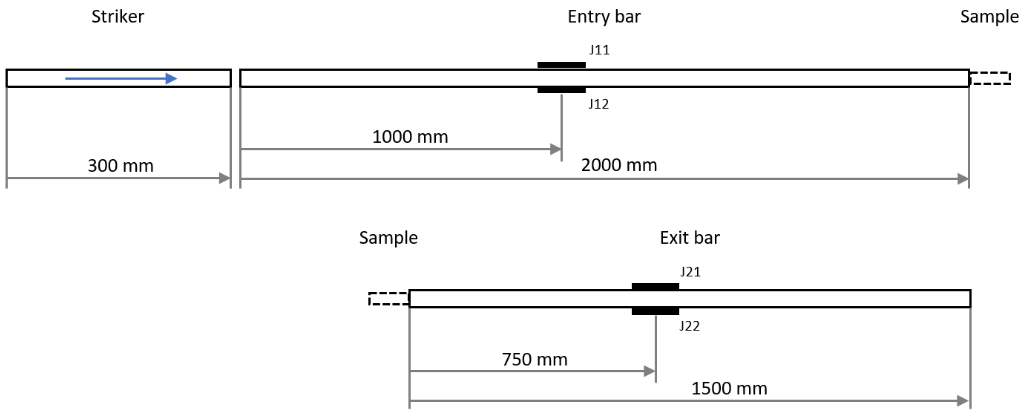

Figure 6.35: Dimensions of the ISAE test setup

New dimensions of the test setup with new positions of the strain gauges are shown in Figure 6.35.

6.4 Numerical and experimental results comparison

In the following sections comparison between numerical and experimental results of the split Hopkinson bar test with the new setup are showed. Samples with the following layups are tested:

- $[0]_{16}$
- $[90]_{16}$
- $[+45-45]_{4s}$

Each type of sample is tested with three different striker bar velocities:

- 4.3 m/s
- 5.1 m/s
- 6.2 m/s

For each velocity, three samples with the same layup are tested. The results presented are the average of the results of the same layup samples tested at the same striker bar velocity. For the sake of completeness, stress-strain curves of all the samples are shown in Appendix A.

Because of some problems with the setup results for $[0]_{16}$ samples with 4.3 m/s velocity were not saved correctly so they are not presented in the corresponding section.

It is important to underline that the accuracy of the results obtained with the method described in Section 6.3.2 is strongly dependent from the correctness of its assumptions. It is notably important, in this context, the uniformity of stress and strains of the sample. This can be verified through the comparison of ϵ_I and $\epsilon_R+\epsilon_T$: small differences in their modulus allow to corroborate the assumption [34].

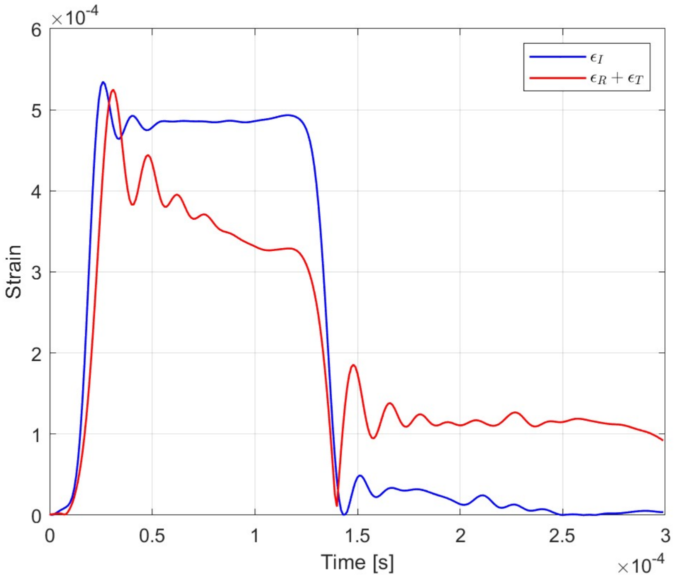

Figure 6.36: Wave comparison to check uniformity of stress and strains

Figure 6.36 shows the comparison between ϵ_I and $\epsilon_R+\epsilon_T$ for the $[90]_{16}$ coupon tested with striker bar velocity of 5.1 m/s. The graph shows differences acceptable for the test. Similar comparison are done for each coupon tested and they all resulted in the validation of the assumption of uniformity of stress and strains.

$[0]_{16}$ Coupon

In this section results for $[0]_{16}$ samples are shown. Prior to the observation of the result it is important to specify that, even with the new geometry, these samples have undergone failure as reported in Figure 6.37.

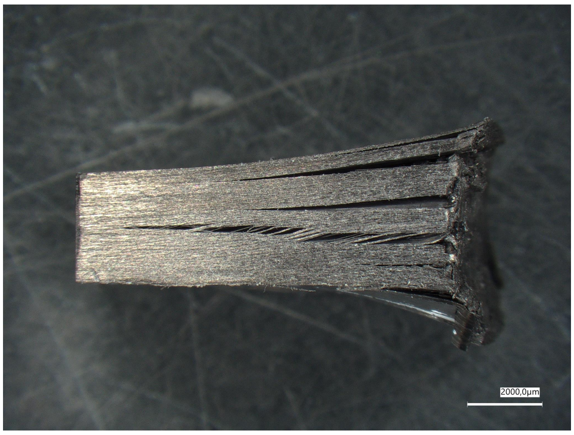

Figure 6.37: Failure on $[0]_{16}$ samples

The sample has undergone a bearing failure process because of the compressive forces involved in the test. Since this kind of failure is not considered in the material model here under study, some differences can be noticed between the numerical model and experimental results.

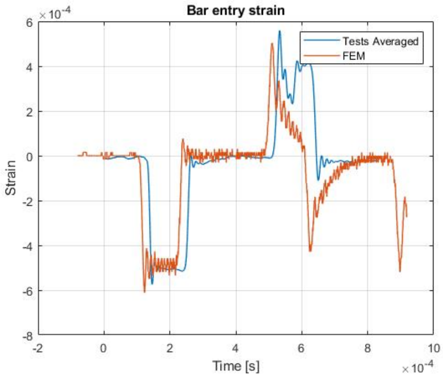

Figure 6.38: Entry bar strain

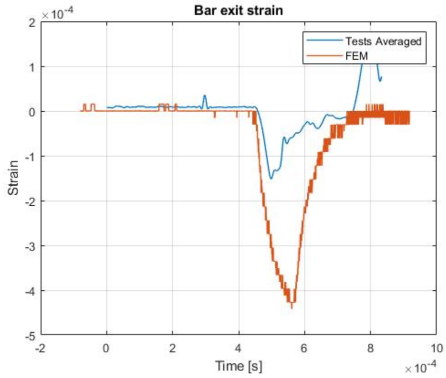

Figure 6.39: Exit bar strain

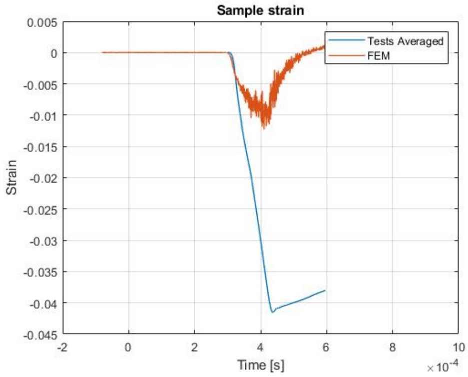

Figure 6.40: Sample strain

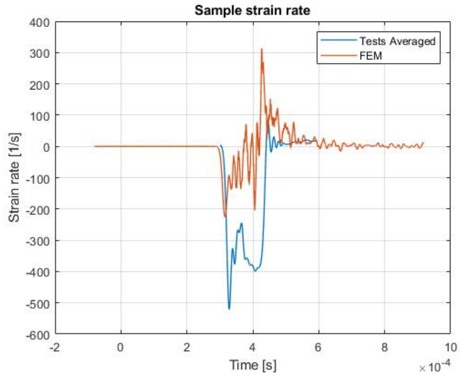

Figure 6.41: Sample strain rate

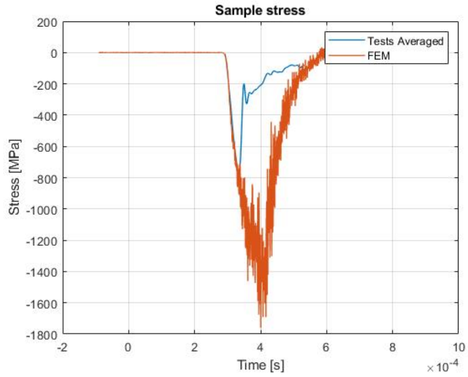

Figure 6.42: Sample stress

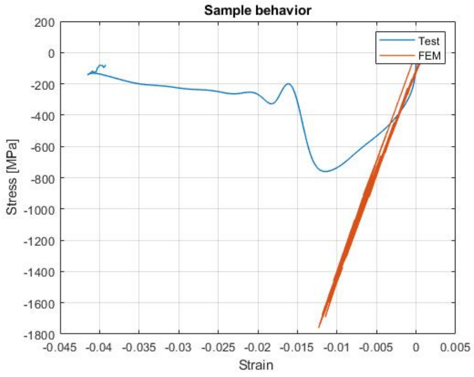

Figure 6.43: Coupon behavior

Figure 6.44: Test results with striker bar velocity of 5.1 m/s

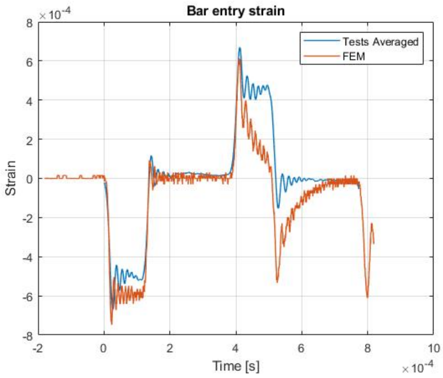

Figure 6.45: Entry bar strain

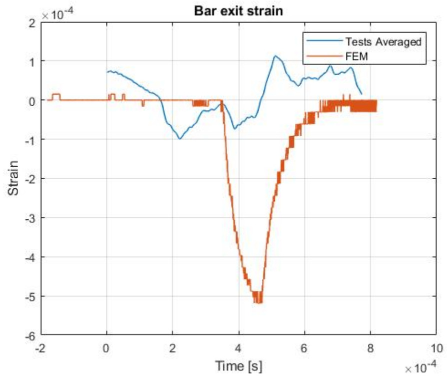

Figure 6.46: Exit bar strain

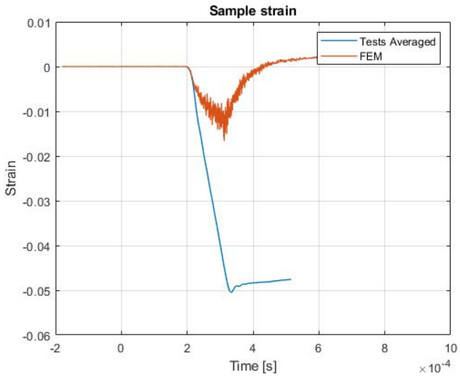

Figure 6.47: Sample strain

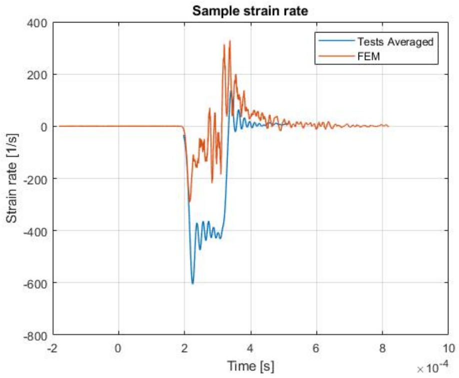

Figure 6.48: Sample strain rate

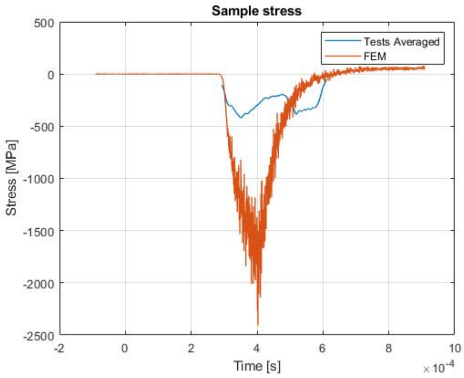

Figure 6.49: Sample stress

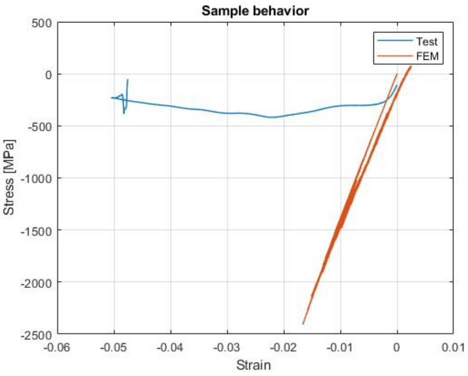

Figure 6.50: Coupon behavior

Figure 6.51: Test results with striker bar velocity of 6.2 m/s

The following observations can be made:

- Strain of the entry bar is perfectly simulated by the numerical model. The abrupt drop and following rise in the reflected wave of the test is due to the failure of the coupon, because of this the shape od the numerical reflected wave is different.
- Levels of the exit bar strains are different between FEM model and test results. The failure of the sample results in lower levels of the transmitted wave.

- During the test the coupon undergoes, because of the failure, higher strain and strain rate than expected from the simulations.
- Stress levels are correctly simulated by the numerical model.
- Until the failure point is reached, stress-strain behavior of the sample is coherent with the numerical results.

$[90]_{16}$ **Coupon**

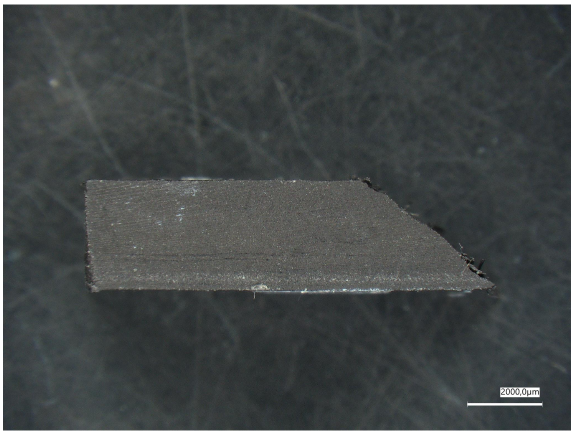

Figure 6.52: Failure on $[90]_{16}$ samples

In this section results for $[90]_{16}$ samples are shown. It is important to notice that the coupon failed in compression with the highest striker bar velocity (Figure 6.52), in this case greater discrepancies appear between numerical and experimental results.

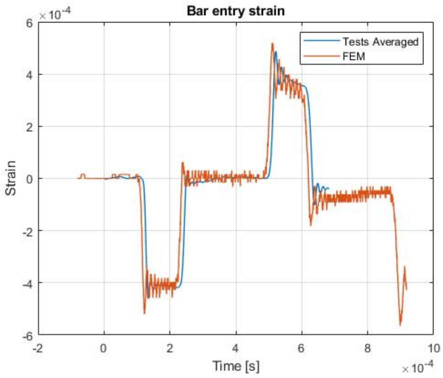

Figure 6.53: Entry bar strain

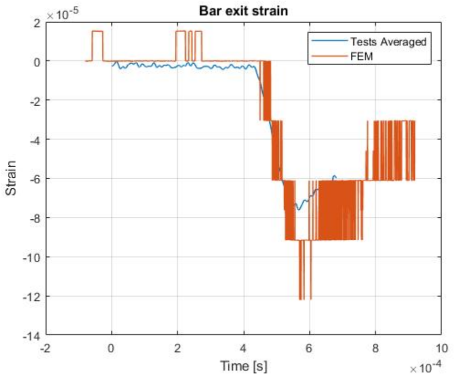

Figure 6.54: Exit bar strain

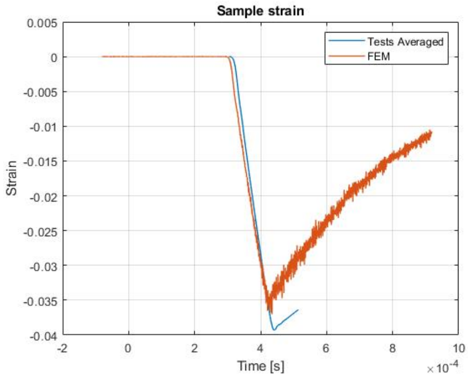

Figure 6.55: Sample strain

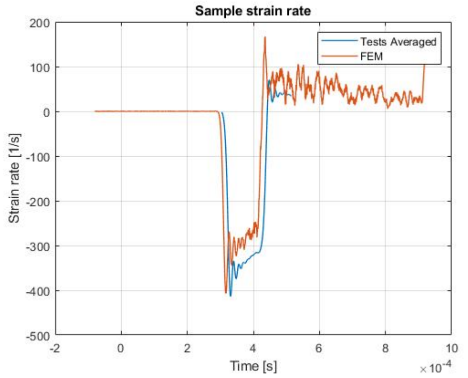

Figure 6.56: Sample strain rate

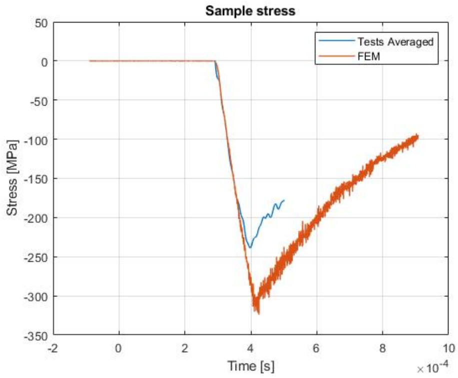

Figure 6.57: Sample stress

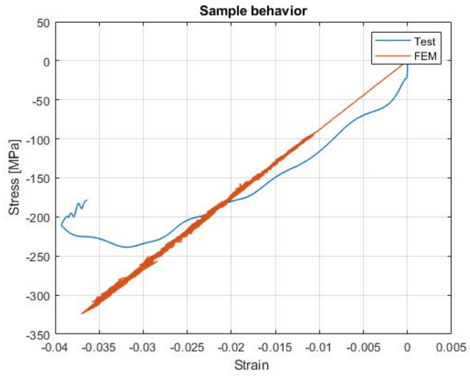

Figure 6.58: Coupon behavior

Figure 6.59: Test results with striker bar velocity of 4.3 m/s

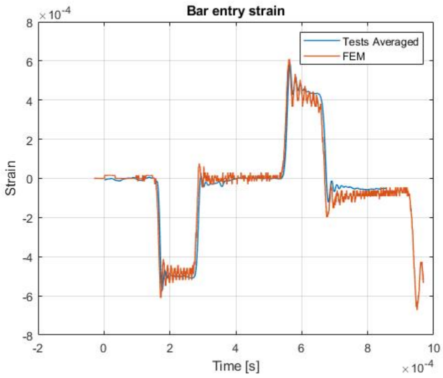

Figure 6.60: Entry bar strain

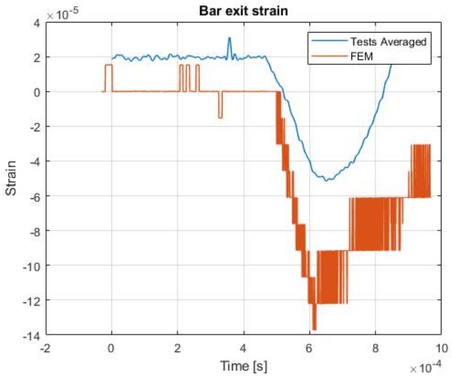

Figure 6.61: Exit bar strain

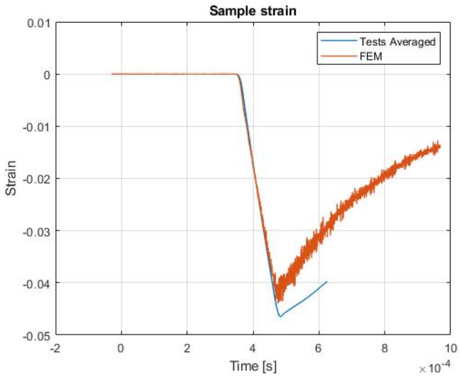

Figure 6.62: Sample strain

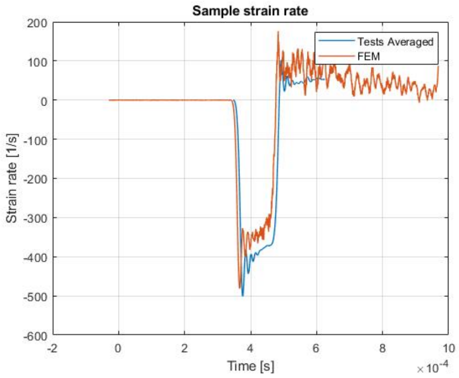

Figure 6.63: Sample strain rate

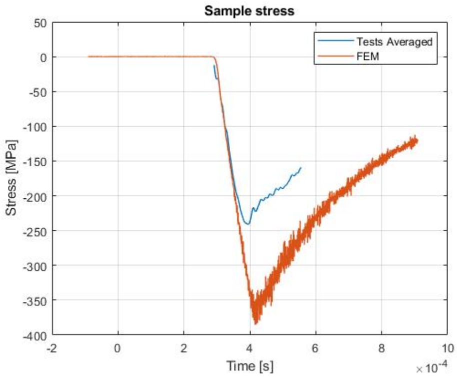

Figure 6.64: Sample stress

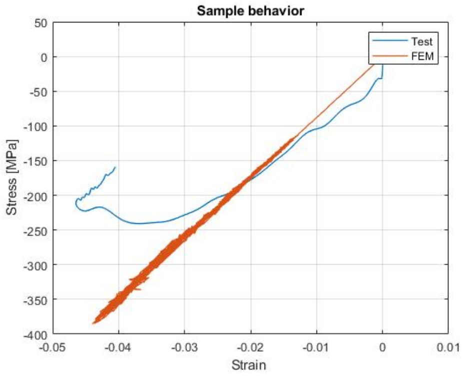

Figure 6.65: Coupon behavior

Figure 6.66: Test results with striker bar velocity of 5.1 m/s

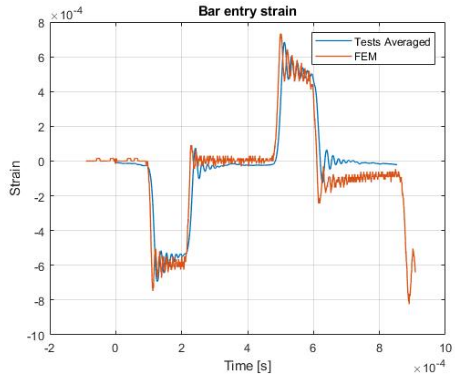

Figure 6.67: Entry bar strain

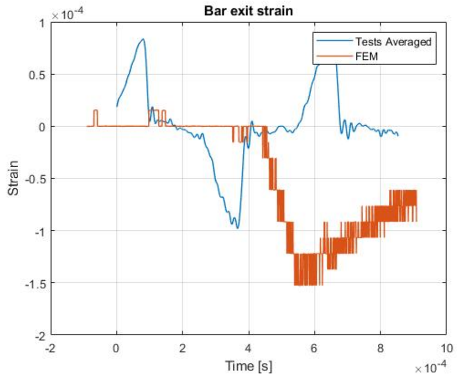

Figure 6.68: Exit bar strain

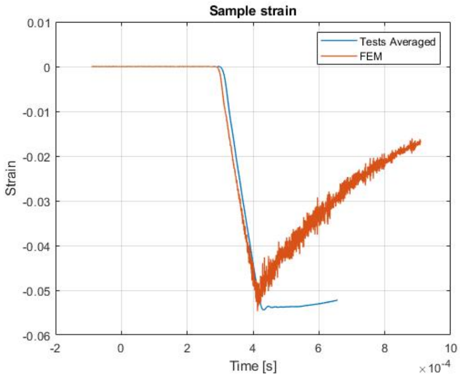

Figure 6.69: Sample strain

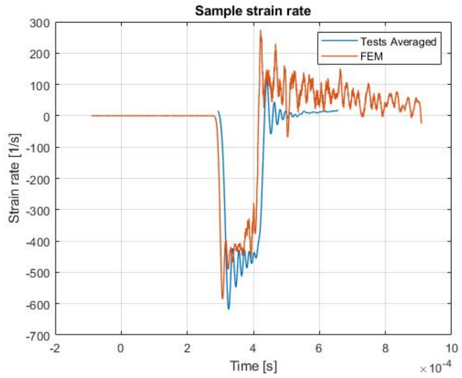

Figure 6.70: Sample strain rate

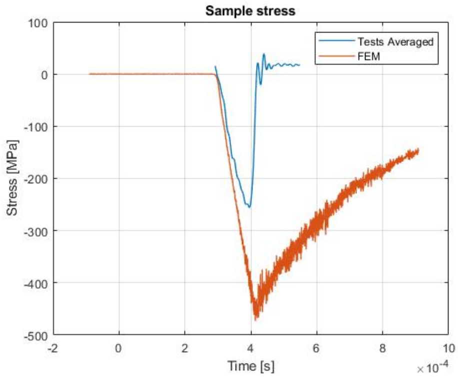

Figure 6.71: Sample stress

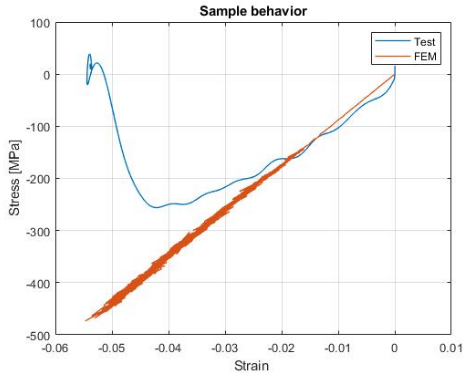

Figure 6.72: Coupon behavior

Figure 6.73: Test results with striker bar velocity of 6.2 m/s

In these cases, the FEM model correctly predicts the coupon's behavior, but the stress levels are typically overestimated when compared to experimental data. This can be attributed to the increased stiffness caused by high strain rate loading, a factor not considered in the material model under investigation

$[+45-45]_{4s}$ **Coupon**

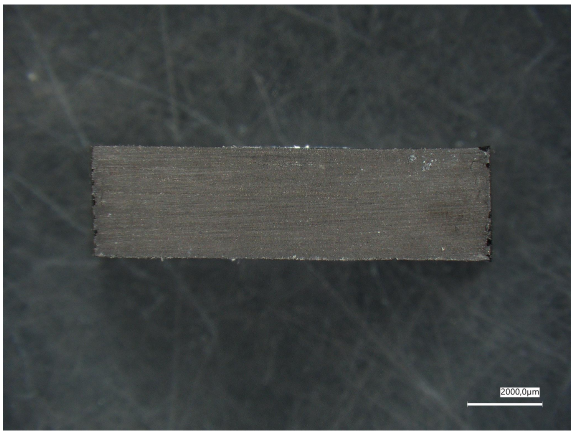

Figure 6.74: $[+45-45]_{4s}$ sample after test

This section shows the comparison between numerical and experimental results on $[+45-45]_{4s}$ samples with different striker bar velocities. No failure has happened during these tests as shown in Figure 6.74.

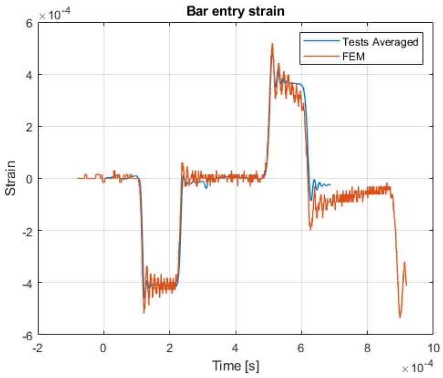

Figure 6.75: Entry bar strain

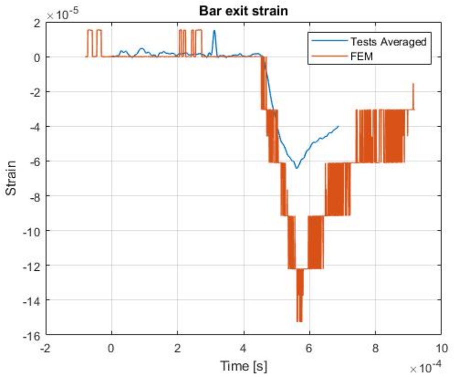

Figure 6.76: Exit bar strain

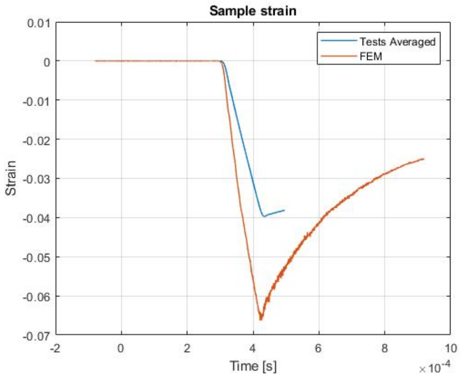

Figure 6.77: Sample strain

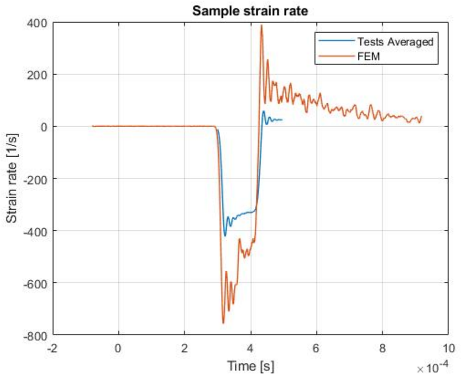

Figure 6.78: Sample strain rate

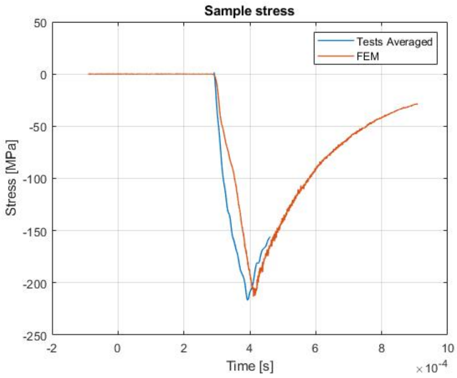

Figure 6.79: Sample stress

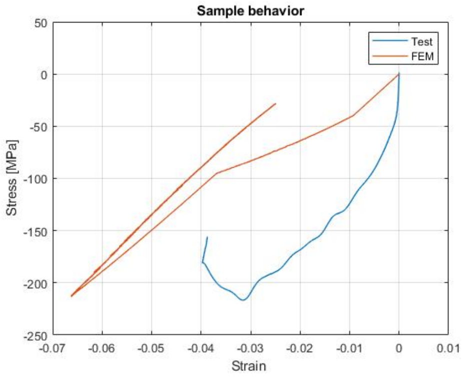

Figure 6.80: Coupon behavior

Figure 6.81: Test results with striker bar velocity of 4.3 m/s

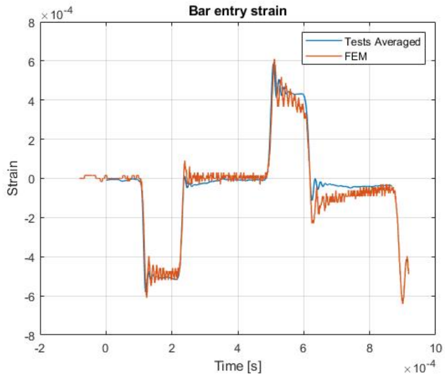

Figure 6.82: Entry bar strain

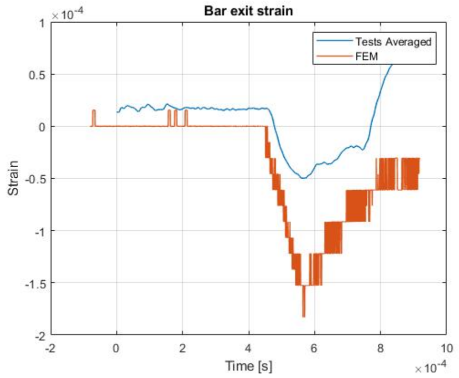

Figure 6.83: Exit bar strain

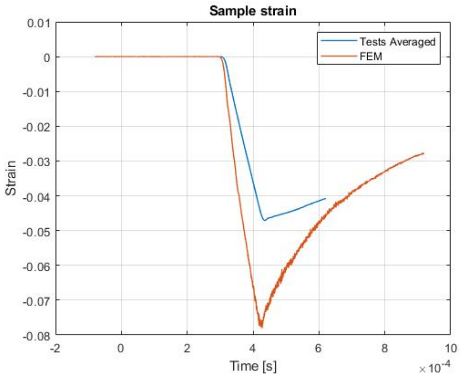

Figure 6.84: Sample strain

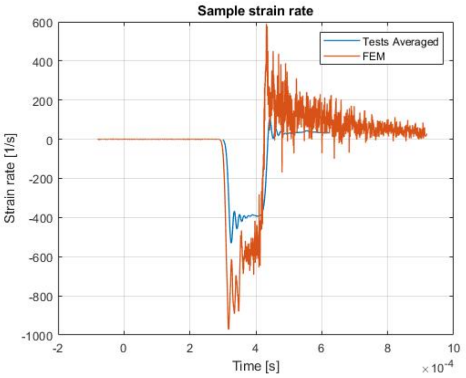

Figure 6.85: Sample strain rate

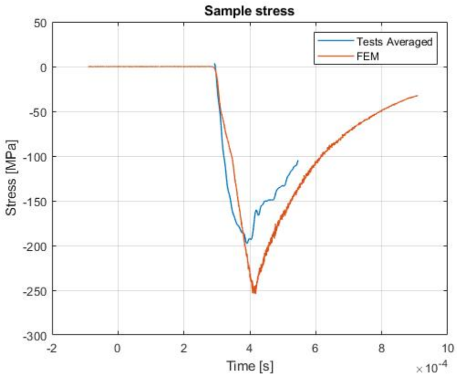

Figure 6.86: Sample stress

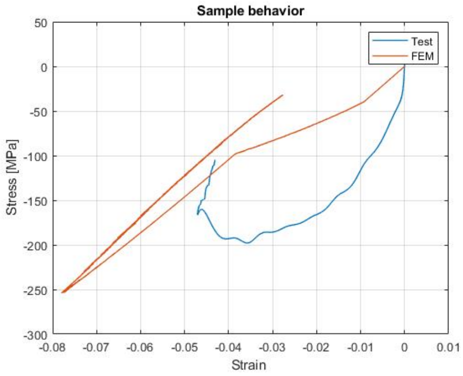

Figure 6.87: Coupon behavior

Figure 6.88: Test results with striker bar velocity of 5.1 m/s

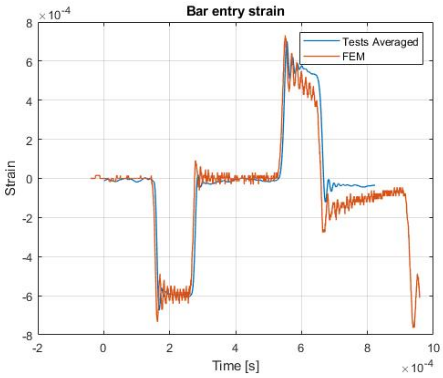

Figure 6.89: Entry bar strain

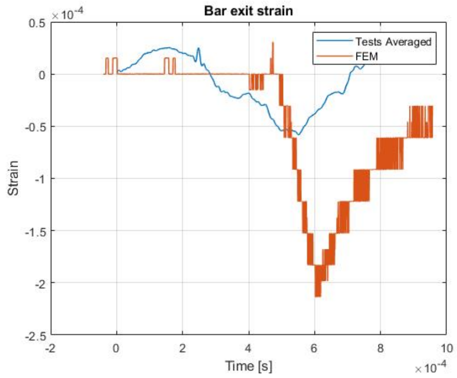

Figure 6.90: Exit bar strain

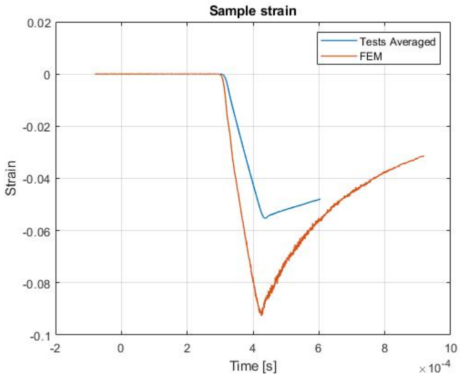

Figure 6.91: Sample strain

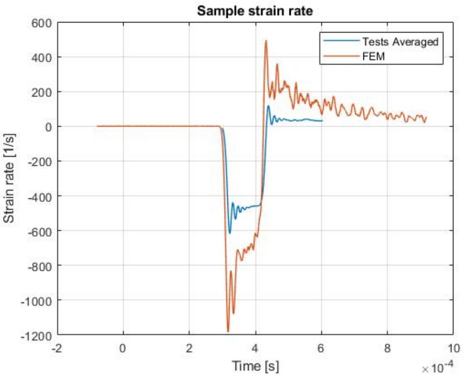

Figure 6.92: Sample strain rate

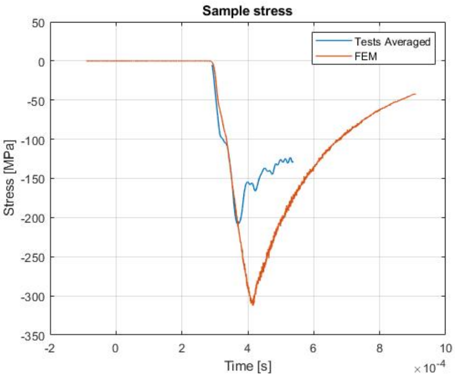

Figure 6.93: Sample stress

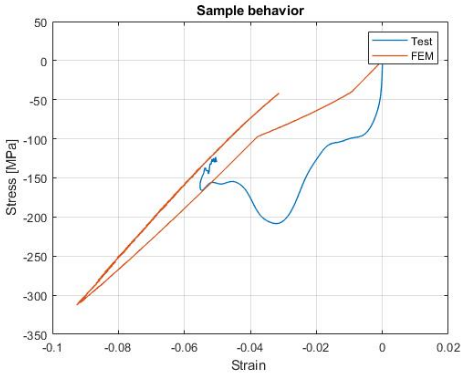

Figure 6.94: Coupon behavior

Figure 6.95: Test results with striker bar velocity of 6.2 m/s

In these cases, the FEM model accurately predicts the coupon's behavior, although the strain and stress levels are generally slightly overestimated compared to the experimental results. It's important to note that this type of layup creates a pure shearing loading condition, leading to very high friction levels that result in highly nonlinear behavior of the sample. This phenomenon is accounted for in the numerical model, which explains why the unloading curve, even when the sample does not fail, does not return to zero strain. The residual strain is due to the viscoelasticity of the PEAK matrix.

6.5 Strain rate effect

In the present section coupon behaviors at different strain rates are compared.

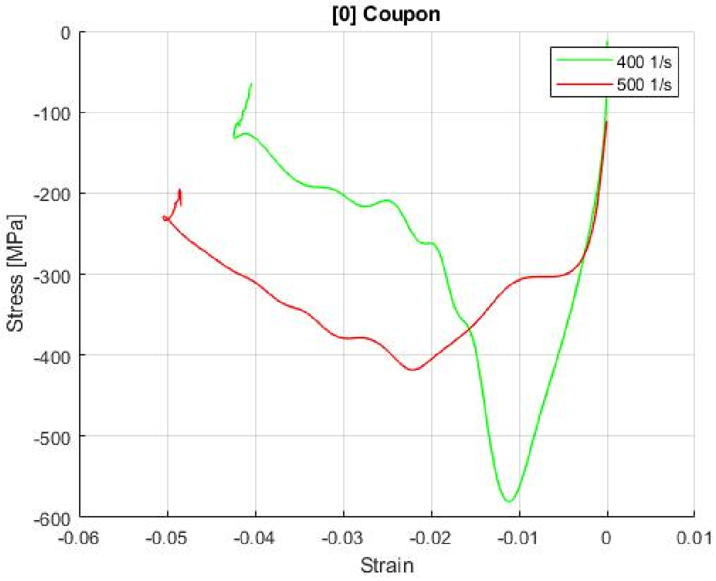

Figure 6.96: Strain rate effect on $[0]_{16}$ samples

The observations of Figure 6.43 and Figure 6.50, when compared to Figure 2.10, lead to the conclusions that numerical stress levels are the expected ones for these longitudinal compression tests. However, due to the delamination failure that occurs, the stress levels are significantly lower, with higher corresponding strains. As a result of these phenomena the data shown in Figure 6.96 are not particularly indicative of the strain rate dependency of the longitudinal behavior of the material under study. Nevertheless, It is still possible to observe that, until the delamination process begins, there is no noticeable effect of strain rate on sample stiffness.

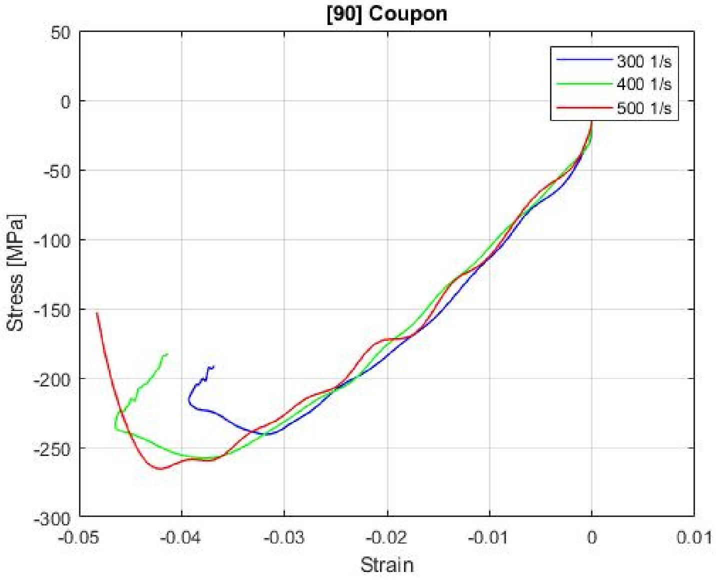

Figure 6.97: Strain rate effect on $[90]_{16}$ samples

Figure 6.97 shows different strain rate behaviors of $[90]_{16}$ samples. The following observations can be done:

- The elastic modulus of the linear part of the curve stays practically the same with the increase of the strain rate;
- In the non-linear part of the curve some stiffening can be observed with the increase of the strain rate

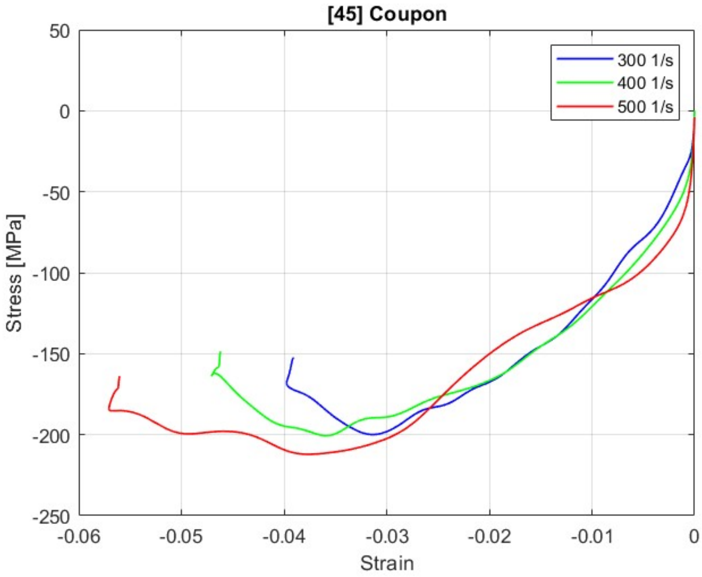

Figure 6.98: Strain rate effect on $[+45-45]_{4s}$ samples

Ultimately, Figure 6.98 shows different strain rate behaviors of $[+45-45]_{4s}$ samples. From the observations of the curves one can conclude that:

- A slight stiffening of the sample appears with the increase of the strain rate;
- High nonlinearity appears with a plateau region at a stress level that increase as the strain rate increases;

In conclusion, while some changes in the material behavior are observed due to variations in the strain rate, the relatively narrow range of strain rates tested in this study makes these changes appear less significant. To gain a clearer understanding of the relationship between strain rate and material behavior, it is necessary to test a broader range of loading strain rates.

Chapter 7

Conclusions and future developments

The primary objective of this thesis is to statically validate the composite material model, specifically designed for fiber-reinforced thermoplastics, which was previously developed at ISAE-Supaero, and to begin exploring the dynamic behavior of these materials, particularly in relation to strain rate effects.

The first goal is achieved by conducting compact compressive and tensile tests, then comparing the results with simulations based on the material model under investigation. The comparison produces very positive results, confirming that the equations and methods used in the model are correct. However, during these simulations, a new issue emerged: convergence problems with the implicit model when applied to complex geometries, such as those in the tests. Further studies are needed to identify the cause of these convergence issues and ultimately find a solution.

The study of the dynamic effects begins with Split Hopkinson Pressure Bar tests on the coupon, which allow for the observation of strain rate effects on the material behavior. However, since the range of strain rates tested is limited, it is not possible to derive a clear relationship between the material's behavior and the strain rate of the applied loading based solely on the results presented in this work. Additional tests should be conducted with a broader range of striker bar velocities to achieve this.

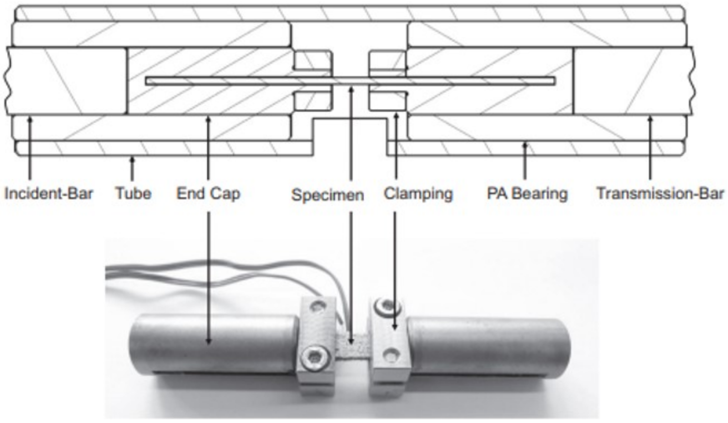

Figure 7.1: Proposal for new SHPB test setup [36]

However, conducting tests at higher velocities requires slight modifications to the setup to prevent the bearing issues discussed earlier in this thesis. Various methods for securing the sample in the correct position are available in the literature, with the most suitable one shown in Figure 7.1. Additionally, thicker coupons should be manufactured to achieve higher transmitted wave levels, resulting in more precise results.

In conclusion, this thesis builds upon the static work previously carried at ISAE-Supaero, providing a foundation for the further investigation of the mechanical behavior of fiber-reinforced thermoplastics. The insights gained not only continue this line of research but also establish the groundwork for studying the dynamic behavior of these materials.

Appendix A

SHPB Tests complete tests results

In the current appendix, stress-strain curves of all the coupons tested with ISAE-Supaero split Hopkinson pressure bar are shown.

$[0]_{16}$ Coupon

Figures A.1 and A.2 present the results for the $[0]_{16}$ samples. Unfortunately, some issues arose when saving the 6.2 m/s data, which means that only the results from the first sample are usable.

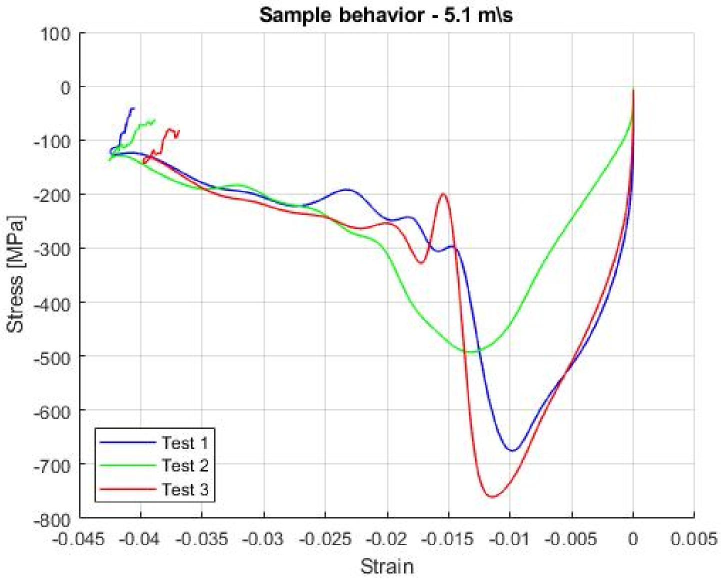

Figure A.1: Stress-strain behavior with striker bar velocity of 5.1 m/s

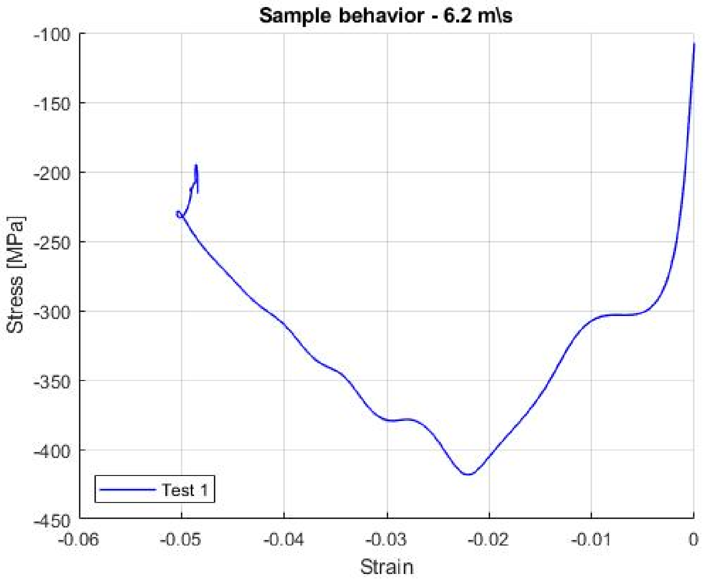

Figure A.2: Stress-strain behavior with striker bar velocity of 6.2 m/s

$[90]_{16}$ Coupon

Figures A.3, A.4 and A.5 present the results for the $[90]_{16}$ samples. Unfortunately, some issues arose when saving the 6.2 m/s data, which means that only the results from the first and second sample are usable. Note that the results are in good agreement with each other.

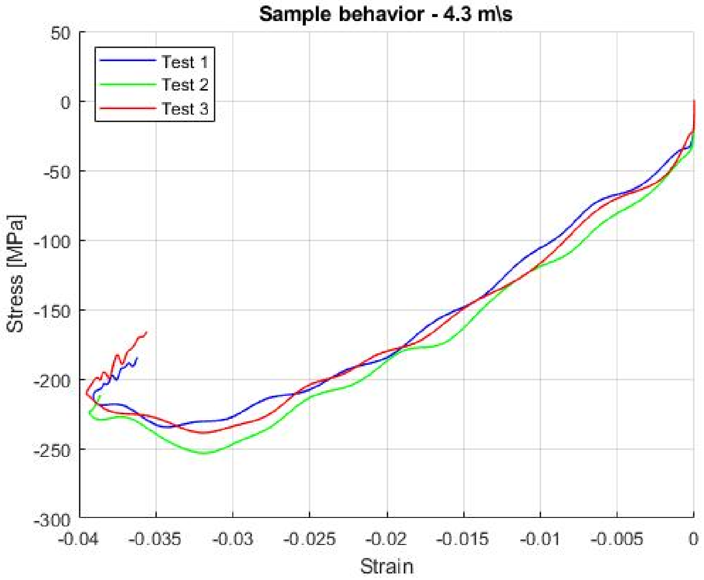

Figure A.3: Stress-strain behavior with striker bar velocity of 4.3 m/s

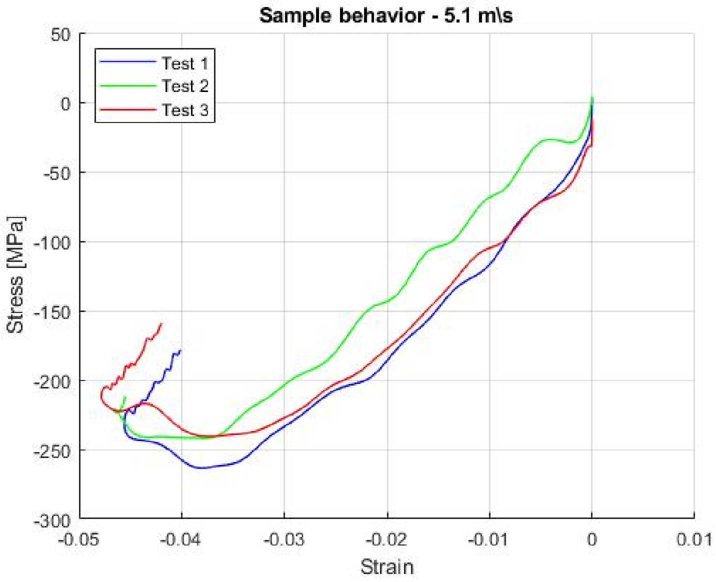

Figure A.4: Stress-strain behavior with striker bar velocity of 5.1 m/s

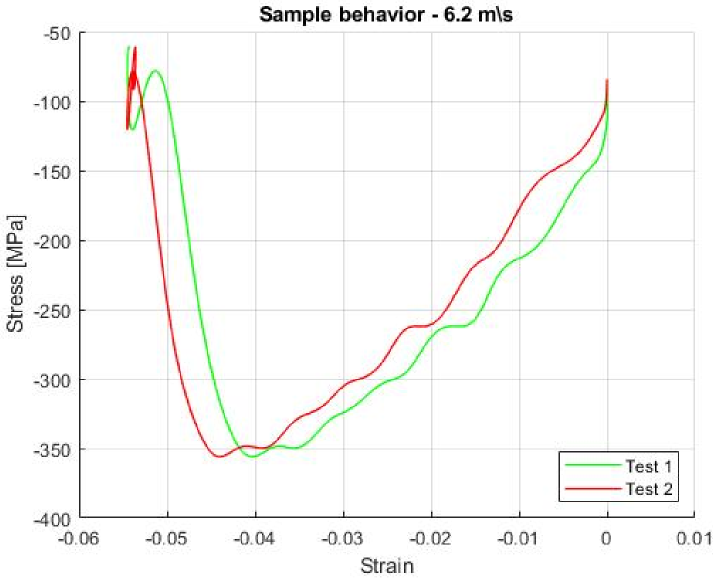

Figure A.5: Stress-strain behavior with striker bar velocity of 6.2 m/s

$[+45 \quad -45]_{4s}$ Coupon

Figures A.6, A.7 and A.8 present the results for the $[+45 \quad -45]_{4s}$ samples. Note that the results are in good agreement with each other.

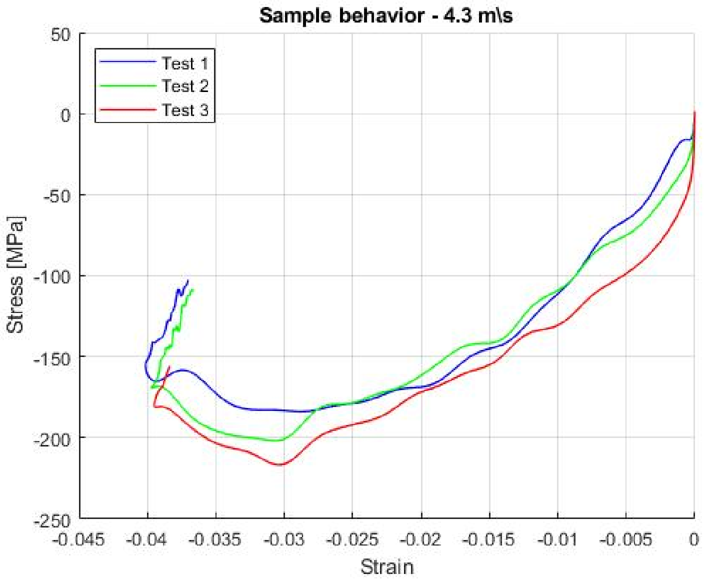

Figure A.6: Stress-strain behavior with striker bar velocity of 4.3 m/s

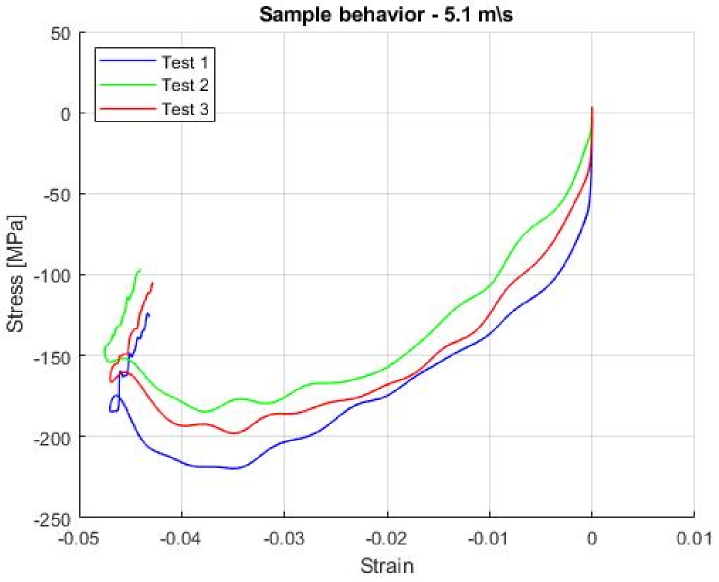

Figure A.7: Stress-strain behavior with striker bar velocity of 5.1 m/s

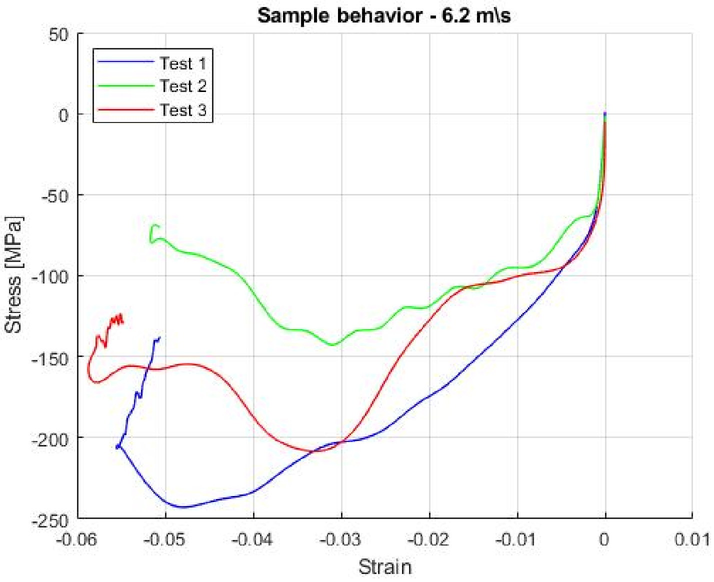

Figure A.8: Stress-strain behavior with striker bar velocity of 6.2 m/s

Bibliography

[1] Au Sudhin et al. “Comparison of Properties of Carbon Fiber Reinforced Thermoplastic and Thermosetting Composites for Aerospace Applications”. en. In: *Materials Today: Proceedings* 24 (2020), pp. 453–462. ISSN: 22147853. DOI: `10.1016/j.matpr.2020.04.297`. URL: `https://linkinghub.elsevier.com/retrieve/pii/S2214785320329199` (visited on 12/02/2024).

[2] Holm Altenbach, Johannes Altenbach, and Wolfgang Kissing. “Classification of Composite Materials”. en. In: *Mechanics of Composite Structural Elements*. Berlin, Heidelberg: Springer Berlin Heidelberg, 2004, pp. 1–14. ISBN: 978-3-642-07411-0. DOI: `10.1007/978-3-662-08589-9_1`. URL: `http://link.springer.com/10.1007/978-3-662-08589-9_1` (visited on 12/03/2024).

[3] Ramesh Talreja and Chandra Veer Singh. *Damage and Failure of Composite Materials*. 1st ed. Cambridge University Press, June 2012. ISBN: 978-0-521-81942-8. DOI: `10.1017/CBO9781139016063`. URL: `https://www.cambridge.org/core/product/identifier/9781139016063/type/book` (visited on 12/04/2024).

[4] P.W.R Beaumont, C. Soutis, and A. Hodzic. *Structural Integrity and Durability of Advanced Composites*. en. Elsevier, 2015. ISBN: 978-0-08-100137-0. DOI: `10.1016/C2014-0-01469-4`. URL: `https://linkinghub.elsevier.com/retrieve/pii/C20140014694` (visited on 12/04/2024).

[5] John A. Nairn. “Matrix Microcracking in Composites”. en. In: *Comprehensive Composite Materials*. Elsevier, 2000, pp. 403–432. ISBN: 978-0-08-042993-9. DOI: `10.1016/B0-08-042993-9/00069-3`. URL: `https://linkinghub.elsevier.com/retrieve/pii/B0080429939000693` (visited on 12/04/2024).

[6] Yuanxin Zhou et al. “Experimental Study on Tensile Behavior of Carbon Fiber and Carbon Fiber Reinforced Aluminum at Different Strain Rate”. en. In: *Applied Composite Materials* 14.1 (Jan. 2007), pp. 17–31. ISSN: 0929-189X, 1573-4897. DOI: `10.1007/s10443-006-9028-5`. URL: `http://link.springer.com/10.1007/s10443-006-9028-5` (visited on 12/02/2024).

[7] Cristobal Garcia and Irina Trendafilova. “Effect of nylon nanofibers on the delamination resistance of glass fiber epoxy composite laminates”. en. In: *Fiber-Reinforced Nanocomposites: Fundamentals and Applications*. Elsevier, 2020, pp. 131–146. ISBN: 978-0-12-819904-6. DOI: `10.1016/B978-0-12-819904-6.00006-2`. URL: `https://linkinghub.elsevier.com/retrieve/pii/B9780128199046000062` (visited on 12/05/2024).

[8] Omar Shabbir Ahmed et al. “Progresses and Challenges of Composite Laminates in Thin-Walled Structures: A Systematic Review”. en. In: *ACS Omega* 8.34 (Aug. 2023), pp. 30824–30837. ISSN: 2470-1343, 2470-1343. DOI: `10.1021/acsomega.3c03695`. URL: `https://pubs.acs.org/doi/10.1021/acsomega.3c03695` (visited on 12/05/2024).

[9] Néstor D. Barulich et al. “On Micro-Buckling of Unidirectional Fiber-Reinforced Composites by Means of Computational Micromechanics”. In: *Latin American Journal of Solids and Structures* 13.16 (Dec. 2016), pp. 3085–3106. ISSN: 1679-7825. DOI: `10.1590/1679-78252867`. URL: `http://www.scielo.br/scielo.php?script=sci_arttext&pid=S1679-78252016001603085&lng=en&tlng=en` (visited on 12/05/2024).

[10] H.M. Hsiao and I.M. Daniel. “Strain rate behavior of composite materials”. en. In: *Composites Part B: Engineering* 29.5 (Sept. 1998), pp. 521–533. ISSN: 13598368. DOI: `10.1016/S1359-8368(98)00008-0`. URL: `https://linkinghub.elsevier.com/retrieve/pii/S1359836898000080` (visited on 02/05/2025).

[11] Bernard Budiansky. “Micromechanics”. en. In: *Computers & Structures* 16.1-4 (Jan. 1983), pp. 3–12. ISSN: 00457949. DOI: `10.1016/0045-7949(83)90141-4`. URL: `https://linkinghub.elsevier.com/retrieve/pii/0045794983901414` (visited on 02/06/2025).

[12] J. Harding and L. M. Welsh. “A tensile testing technique for fibre-reinforced composites at impact rates of strain”. en. In: *Journal of Materials Science* 18.6 (June 1983), pp. 1810–1826. ISSN: 0022-2461, 1573-4803. DOI: `10.1007/BF00542078`. URL: `http://link.springer.com/10.1007/BF00542078` (visited on 02/06/2025).

[13] H. Koerber and P.P. Camanho. “High strain rate characterisation of unidirectional carbon–epoxy IM7-8552 in longitudinal compression”. en. In: *Composites Part A: Applied Science and Manufacturing* 42.5 (May 2011), pp. 462–470. ISSN: 1359835X. DOI: `10.1016/j.compositesa.2011.01.002`. URL: `https://linkinghub.elsevier.com/retrieve/pii/S1359835X11000054` (visited on 12/02/2024).

[14] Robert Millard Jones. *Mechanics of composite materials*. eng. Second edition. Boca Raton London New York: CRC Press, Taylor & Francis Group, 2021. ISBN: 978-1-56032-712-7.

[15] Luis Laborda Pérez. “Damage and failure identification of composite laminates with carbon fibers and thermoplastic matrix under static and dynamic loading”. Aug. 2024. ISAE Supaero.

[16] G. L. M. da Rocha Coelho. “Modelling of damage and failure of thermoplas tic matrix composite laminates”. Master’s thesis. Universidade do porto, Porto, Portugal, Oct. 2023.

[17] Pedro P. Camanho et al. “Prediction of in situ strengths and matrix cracking in composites under transverse tension and in-plane shear”. en. In: *Composites Part A: Applied Science and Manufacturing* 37.2 (Feb. 2006), pp. 165–176. ISSN: 1359835X. DOI: `10.1016/j.compositesa.2005.04.023`. URL: `https://linkinghub.elsevier.com/retrieve/pii/S1359835X05002526` (visited on 01/15/2025).

[18] G. Catalanotti, P.P. Camanho, and A.T. Marques. "Three-dimensional failure criteria for fiber-reinforced laminates". en. In: *Composite Structures* 95 (Jan. 2013), pp. 63–79. ISSN: 02638223. DOI: `10.1016/j.compstruct.2012.07.016`. URL: `https://linkinghub.elsevier.com/retrieve/pii/S0263822312003443` (visited on 01/15/2025).

[19] A Puck. "FAILURE ANALYSIS OF FRP LAMINATES BY MEANS OF PHYSICALLY BASED PHENOMENOLOGICAL MODELS". In: *Composites Science and Technology* 58.7 (July 1998), pp. 1045–1067. ISSN: 02663538. DOI: `10.1016/S0266-3538(96)00140-6`. URL: `https://linkinghub.elsevier.com/retrieve/pii/S0266353896001406` (visited on 01/15/2025).

[20] J.D. Fuller and M.R. Wisnom. "Pseudo-ductility and damage suppression in thin ply CFRP angle-ply laminates". en. In: *Composites Part A: Applied Science and Manufacturing* 69 (Feb. 2015), pp. 64–71. ISSN: 1359835X. DOI: `10.1016/j.compositesa.2014.11.004`. URL: `https://linkinghub.elsevier.com/retrieve/pii/S1359835X1400342X` (visited on 01/17/2025).

[21] G. Lubineau and P. Ladevèze. "Construction of a micromechanics-based intralaminar mesomodel, and illustrations in ABAQUS/Standard". en. In: *Computational Materials Science* 43.1 (July 2008), pp. 137–145. ISSN: 09270256. DOI: `10.1016/j.commatsci.2007.07.050`. URL: `https://linkinghub.elsevier.com/retrieve/pii/S0927025607002303` (visited on 01/24/2025).

[22] Jinsong Huang and D. V. Griffiths. "Return Mapping Algorithms and Stress Predictors for Failure Analysis in Geomechanics". en. In: *Journal of Engineering Mechanics* 135.4 (Apr. 2009), pp. 276–284. ISSN: 0733-9399, 1943-7889. DOI: `10.1061/(ASCE)0733-9399(2009)135:4(276)`. URL: `https://ascelibrary.org/doi/10.1061/%28ASCE%290733-9399%282009%29135%3A4%28276%29` (visited on 01/24/2025).

[23] P Ladeveze and E Ledantec. "Damage modelling of the elementary ply for laminated composites". en. In: *Composites Science and Technology* 43.3 (1992), pp. 257–267. ISSN: 02663538. DOI: `10.1016/0266-3538(92)90097-M`. URL: `https://linkinghub.elsevier.com/retrieve/pii/026635389290097M` (visited on 01/26/2025).

[24] Fuji Wang et al. "A comparison of cutting mechanisms of the carbon fibre reinforced thermoset and thermoplastic composites by the experimental and computational modelling methods". en. In: *Journal of Manufacturing Processes* 79 (July 2022), pp. 895–910. ISSN: 15266125. DOI: `10.1016/j.jmapro.2022.05.033`. URL: `https://linkinghub.elsevier.com/retrieve/pii/S1526612522003474` (visited on 01/26/2025).

[25] P. Linde, J. Pleitner, and H. Boer. "Modelling and Simulation of Fibre Metal Laminates". In: *ABAQUS Users' Conference* (2004).

[26] Matt Veidth. *What is Hashin Failure Criteria? | Hashin Damage in Abaqus*. URL: `https://caeassistant.com/blog/hashin-failure-criteria-hashin-damage-abaqus/`.

[27] S. Pinho et al. "Failure models and criteria for frp under in-plane or three-dimensional stress states including shear non-linearity". In: *tech. rep., National Aeronautics and Space Administration* (Feb. 2005).

[28] S.T. Pinho, P. Robinson, and L. Iannucci. “Fracture toughness of the tensile and compressive fibre failure modes in laminated composites”. en. In: *Composites Science and Technology* 66.13 (Oct. 2006), pp. 2069–2079. ISSN: 02663538. DOI: `10.1016/j.compscitech.2005.12.023`. URL: `https://linkinghub.elsevier.com/retrieve/pii/S026635380600011X` (visited on 12/10/2024).

[29] D20 Committee. *Test Methods for Plane-Strain Fracture Toughness and Strain Energy Release Rate of Plastic Materials.* en. DOI: `10.1520/D5045-14R22`. URL: `http://www.astm.org/cgi-bin/resolver.cgi?D5045-14R22` (visited on 12/02/2024).

[30] M.J. Laffan et al. “Measurement of the in situ ply fracture toughness associated with mode I fibre tensile failure in FRP. Part I: Data reduction”. en. In: *Composites Science and Technology* 70.4 (Apr. 2010), pp. 606–613. ISSN: 02663538. DOI: `10.1016/j.compscitech.2009.12.016`. URL: `https://linkinghub.elsevier.com/retrieve/pii/S0266353809004515` (visited on 12/11/2024).

[31] V. Médeau. “Rupture des composites tissés 3D: de la caractérisation expérimentale à la simulation robuste des effets d’échelle”. PhD thesis. Institut Supérieur de l’Aéronautique et de l’Espace, 2019.

[32] ASTM E399-90. *Standard test method for plane-strain fracture toughness of metallic materials.*

[33] N. Blanco et al. “Intralaminar fracture toughness characterisation of woven composite laminates. Part I: Design and analysis of a compact tension (CT) specimen”. en. In: *Engineering Fracture Mechanics* 131 (Nov. 2014), pp. 349–360. ISSN: 00137944. DOI: `10.1016/j.engfracmech.2014.08.012`. URL: `https://linkinghub.elsevier.com/retrieve/pii/S0013794414002744` (visited on 02/03/2025).

[34] U.S. Lindholm. “Some experiments with the split hopkinson pressure bar*”. en. In: *Journal of the Mechanics and Physics of Solids* 12.5 (Nov. 1964), pp. 317–335. ISSN: 00225096. DOI: `10.1016/0022-5096(64)90028-6`. URL: `https://linkinghub.elsevier.com/retrieve/pii/0022509664900286` (visited on 01/30/2025).

[35] Clive R. Siviour and Jennifer L. Jordan. “High Strain Rate Mechanics of Polymers: A Review”. en. In: *Journal of Dynamic Behavior of Materials* 2.1 (Mar. 2016), pp. 15–32. ISSN: 2199-7446, 2199-7454. DOI: `10.1007/s40870-016-0052-8`. URL: `http://link.springer.com/10.1007/s40870-016-0052-8` (visited on 03/06/2025).

[36] Marina Ploeckl et al. “A dynamic test methodology for analyzing the strain-rate effect on the longitudinal compressive behavior of fiber-reinforced composites”. en. In: *Composite Structures* 180 (Nov. 2017), pp. 429–438. ISSN: 02638223. DOI: `10.1016/j.compstruct.2017.08.048`. URL: `https://linkinghub.elsevier.com/retrieve/pii/S0263822317307250` (visited on 12/02/2024).